

Preparation of supported silver catalysts



Petra Keijzer

Preparation of supported silver catalysts

Petra Henrica Keijzer

PhD thesis, Utrecht University
ISBN: 978-90-393-7443-6

Cover illustration and design: Eva Huang (www.happynutcreations.com)
Printed by ProefschriftMaken (www.proefschriftmaken.nl)

Copyright © Petra Keijzer, 2022

Preparation of supported silver catalysts

Bereiding van gedragen zilverkatalysatoren
(met een samenvatting in het Nederlands)

Proefschrift

ter verkrijging van de graad van doctor aan de Universiteit Utrecht
op gezag van de rector magnificus, prof. dr. H.R.B.M. Kummeling,
ingevolge het besluit van het college voor promoties
in het openbaar te verdedigen op

woensdag 6 april 2022 des ochtends te 10.15 uur

door

Petra Henrica Keijzer

geboren op 20 februari 1992 te Noordoostpolder

Promotoren:

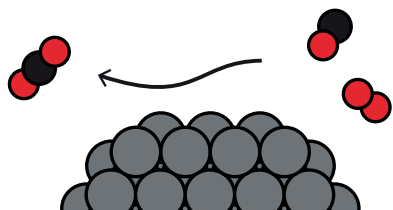
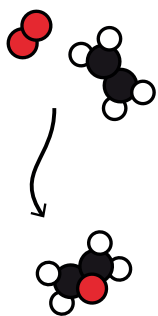
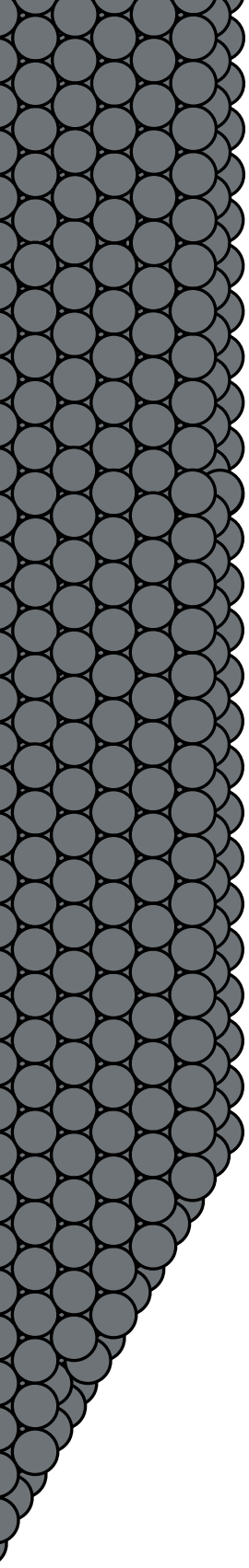
Prof. dr. ir. K.P. de Jong

Prof. dr. P.E. de Jongh

This research was supported by the Netherlands Center for Multiscale Catalytic Energy Conversion (MCEC), an NWO Gravitation program funded by the Ministry of Education, Culture and Science of the government of the Netherlands.

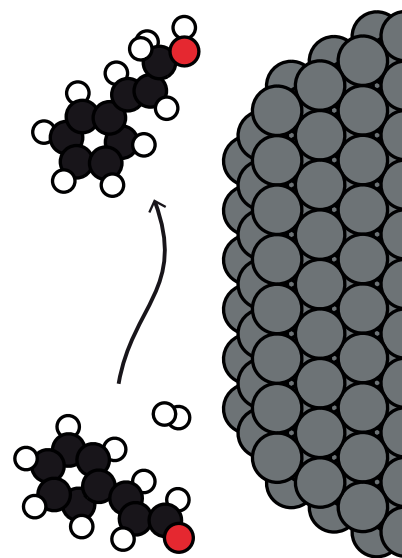
Contents

Chapter 1. Introduction to supported silver catalysts	1
Chapter 2. Preparation of single phase ordered macroporous α -alumina	13
Chapter 3. Stability of silver on α -alumina for ethylene epoxidation	27
Chapter 4. Supported silver catalysts prepared via melt infiltration	45
Chapter 5. Utilization of silver silicate for highly dispersed silver on silica catalysts	61
Chapter 6. Conclusions and perspectives	75
Appendices	83
References	119
Nederlandse samenvatting voor iedereen	137
Acknowledgements	147
List of publications and presentations	151
About the author	155



Chapter 1

Introduction to supported silver catalysts



Catalysts are essential. One or more catalysts are involved in the production of 85–90% of all chemicals and materials produced in industry [1]. Catalysts provide alternative reaction pathways for chemical reactions, enabling specific reactions to proceed at lower temperatures. This may enable the use of milder reaction conditions and, more importantly, it may improve the product selectivity, when the activation energy of a desired reaction pathway becomes lower than undesired pathways. This leads to a higher quantity of desired products, while the production of side products is minimized. Generally speaking, catalysts accelerate and steer chemical reactions, thus maximizing the quantity of desired products formed per unit of time and per amount of starting material.

In circa 80% of the chemical reactions, heterogeneous catalysts are used [2]. Often, these consist of metal particles supported on a porous metal oxide material. The chemical reaction takes place on the surface of the metal particles, where the metal of choice differs greatly per chemical reaction. This has foremost to do with the binding strength between the metal and the reactants, intermediates and products. On the one hand, the binding should be strong enough for the reactants to engage an interaction, but on the other hand, the binding should not be too strong, as the products need to be released after the reaction is complete. For most reactions, multiple metals can be used to catalyze the reaction. If so, the metal of choice depends on the desired products and its efficiency in the reaction, but also on the production cost and lifetime of the catalyst.

Silver catalysts are essential. For some reactions, the range of metals giving satisfactory results is very limited. One example of this is the epoxidation of ethylene (ethene) to form ethylene oxide, where industrially only silver is used [3–6]. More specifically, this chemical reaction is the main application of silver-containing catalysts. With an annual global production of 35 million tons in 2016 and a continues growth of 0.6–3% over the last years, ethylene oxide is, and will remain for the years to come, a fundamental building block in the chemical industry [7–10]. Among others, it ends up in anti-freeze coolants, plastics, detergents, surfactants, lubricants and paints. A simplified scheme of the ethylene epoxidation reaction is given in Figure 1.1. Next to the desired production

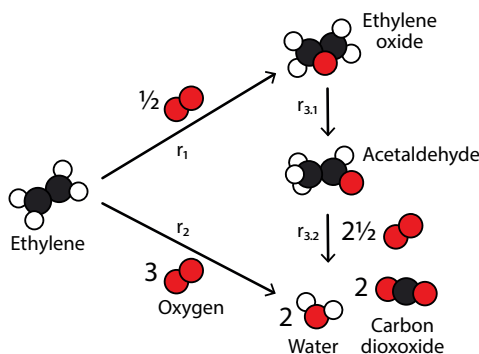


Figure 1.1 Schematic representation of the selective and total oxidation of ethylene to form ethylene oxide (r_1) or carbon monoxide and water (r_2). Once formed, ethylene oxide may isomerize into acetaldehyde ($r_{3,1}$) and be further oxidized into carbon dioxide and water ($r_{3,2}$).

of ethylene oxide (r_1), the undesired full combustion path is shown (r_2), yielding carbon dioxide and water. Both processes are exothermic. Without the use of a catalyst, only the full oxidation of ethylene ($\Delta H_r = -1323 \text{ kJ mol}_{\text{ethylene}}^{-1}$) would take place, as this is thermodynamically more favorable than the formation of ethylene oxide ($\Delta H_r = -106.7 \text{ kJ mol}_{\text{ethylene}}^{-1}$) [11,12]. Using silver, with its unique binding strength, strong enough for ethylene and oxygen adsorption and weak enough for ethylene oxide desorption, ethylene oxide can form and desorb [5,13]. As a result, high selectivities towards ethylene oxide can be obtained. Unfortunately, also after formation, ethylene oxide may be further oxidized to form carbon dioxide and water (r_3). This latter reaction is facilitated by hydroxyl groups present on the support material, via the rate determining isomerization of ethylene oxide to acetaldehyde ($r_{3,1}$) that is subsequently rapidly oxidized on silver to carbon dioxide and water ($r_{3,2}$) [13–16].

Another reaction where primarily silver is used on industrial scale is the conversion of methanol to formaldehyde where the conversion over (predominantly unsupported) silver catalysts takes place via oxidative dehydrogenation of methanol [17–19]. Formaldehyde is mainly used for the production of industrial resins which end up in binders, adhesives, coatings, and finishers to be used in, among others, the construction, automotive and aircraft industry, and in pharmaceuticals and cosmetics [19,20]. Next to these industrial applications, academic research shows the potential of silver as a catalyst in other (selective) oxidation and hydrogenation reactions, but also in the field of photo- and electrocatalysis [21,22]. Some examples include the selective or total oxidation of carbon monoxide, alcohols, nitrogen oxides and soot [23–29], the selective hydrogenation of nitroarenes and α,β -unsaturated aldehydes [30–35], the degradation of organic dyes, and the electroreduction of carbon dioxide to carbon monoxide [36–41].

The structure of the silver is essential. As stated above, chemical reactions take place on the surface of the silver. By decreasing the size of the individual silver particles, the specific surface area ($\text{m}^2 \text{g}^{-1}$) for silver is increased. Therefore, the number of surface sites, and the weight-based activity of the catalyst, increases. Another major benefit of working with supported silver nanoparticles instead of bulk silver is the structure of the silver particles. For most reactions, the activity and selectivity depend on the silver facets available. This surface is dependent on the size of the silver particles, as the atomic configuration of the surface changes with the particle size. Figure 1.2 shows supported silver particles of three different sizes, each having a different

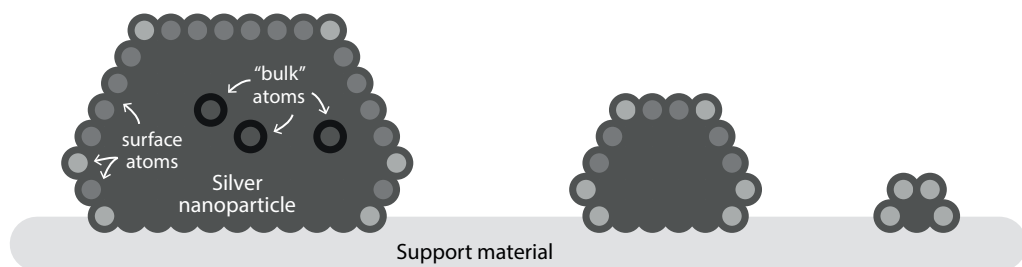


Figure 1.2 Schematic representation of the atomic configuration in supported silver particles varying in size. The lighter the color of the atoms, the lower their coordination number.

ratio of bulk (dark gray) to surface (lighter gray) atoms. Additionally, the surface of larger silver particles contains larger areas of surface atoms arranged in an atomically flat surface than smaller particles, which relatively contain more edge and corner atoms. Atoms on the edges of a particle, and especially those on the corners, have lower coordination numbers than atoms on a flat surface. The difference in coordination number alters the binding strength of these atoms with the reactants [42–44]. Therefore, some reactions show an enhanced activity or selectivity on smaller nanoparticles (<15 nm), for example, the oxidation of carbon monoxide and selective hydrogenation reactions [31,45–47]. For other reactions, larger particles (>50 nm) are favored, such as the epoxidation of ethylene and the oxidative dehydrogenation of methanol [19,48–51].

Control during catalyst synthesis is essential. To reach the highest efficiency, catalysts with the optimal silver particle size need to be prepared. To limit the growth of the silver nanoparticles, they are typically anchored on a support material. The type of support has a large influence on the catalytic reaction [52]. This can be positive, as a strong metal-support interaction may provide a higher stability of the metal particles [53]. However, the support can also play a negative role, for example in the ethylene epoxidation, where hydroxyl groups present on the surface of the support facilitate the isomerization of the ethylene oxide [13–16]. Alumina, silica, titania and carbon are popular support materials, as these materials are easy to shape, have a high mechanical and thermal stability and are relatively inexpensive [52].

Often, heterogeneous catalysts are prepared via the distribution of a metal precursor over the support, followed by precursor decomposition. Mostly impregnation or precipitation are used for the synthesis of industrial catalysts [48,54–56]. Schematic representations of these catalyst preparation methods are given in Figures 1.3 and 1.4, respectively. Both techniques ensure a homogeneous distribution of the precursor over the support surface. However, redistribution of the metal species both during drying and precursor decomposition may lead to large intra- and interparticle heterogeneities in the metal distribution, especially at relative high metal loadings [56–61]. Additionally, for impregnation, the maximum weight loading is constrained by the solubility of precursors in pore volume, whereas precipitation, on the other hand, allows high loadings but is accompanied by the production of large amounts of waste [54].

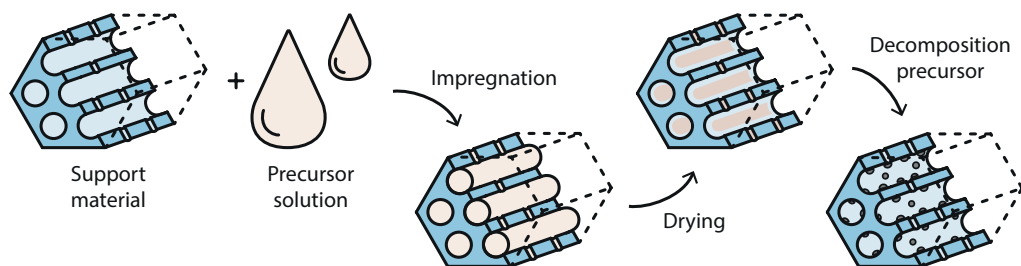


Figure 1.3 Schematic representation of catalyst preparation via impregnation. First, the pores of the support material are filled with a precursor solution. In the next step, the material is dried, and finally, the precursor is decomposed and/or reduced to end up with supported metal particles.

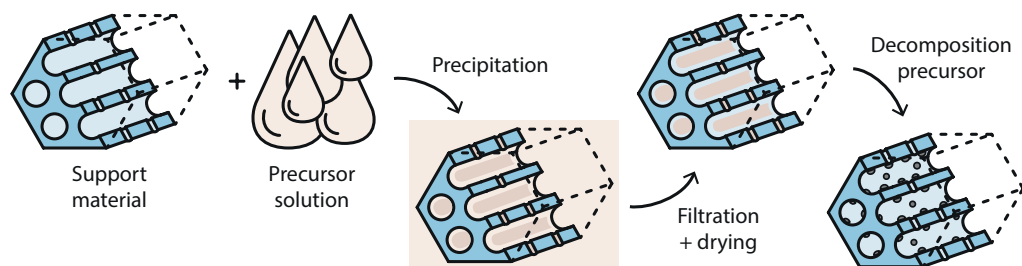


Figure 1.4 Schematic representation of catalyst preparation via precipitation. The support material is soaked in the precursor solution, while the precursor solution is changed (for example its pH) so that the precursor precipitates on the support material. Once precipitation is complete, the material is filtered, dried, and finally the precursor is decomposed and/or reduced to end up with supported metal particles.

There are several ways to prevent unwanted agglomeration of the metal species during the decomposition step. For example, the redistribution of metal species can be limited via providing a stronger interaction between the support and the precursor, and/or via changing decomposition parameters such as atmosphere and heating ramp to facilitate alternative deactivation pathways [55,62–64]. Another way is to form an immobile intermediate, such as via the formation of a metal silicate, for silica-supported catalysts [65]. The metal silicate can be further decomposed/reduced in a later step to form the desired metal nanoparticles. By utilizing copper or nickel silicates as intermediates, supported copper or nickel catalysts with a high dispersion and narrow particle size have been prepared, even at metal loadings up to 40 wt% [56,66–70]. In literature, preparation routes for several different silver silicates can be found [71–75]. These silver silicate compounds mostly find their application in the field of photocatalysis, where they show a higher activity compared to metallic silver [76–83]. Whereas the synthesis of pure and highly crystalline silver silicate generally takes place under high oxygen pressures, supported silver silicate can be synthesized by reacting a silica source with silver nitrate at atmospheric pressure [84,85]. By first distributing the silver nitrate over the support, and then applying an extra heat treatment to form silver silicate, the precursor can be affixed on the support material, as schematically shown in Figure 1.5.

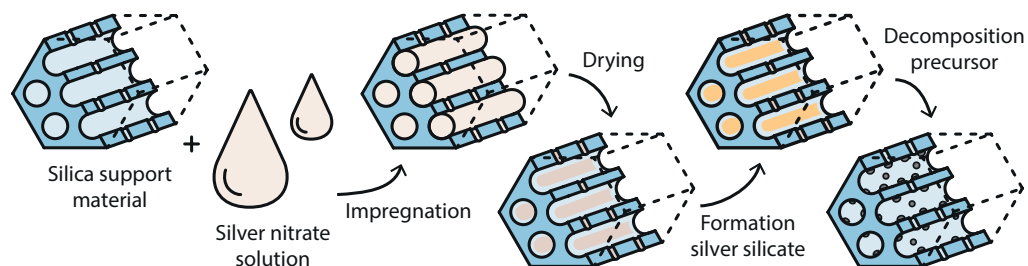


Figure 1.5 Schematic representation of catalyst preparation via silver silicate utilization. First, impregnation is used to fill the pores of the support material with precursor solution. After drying, a heat treatment is used to form silver silicate, at the expense of silver nitrate and some of the silica support. Finally, the silver silicate is decomposed to end up with supported particles.

An alternative and promising preparation method for heterogeneous catalysts is melt infiltration [86]. Currently, it is mainly applied for the synthesis of nanostructured materials in the field of batteries and ceramics [87–91]. A schematic representation of this preparation method is given in Figure 1.6. Melt infiltration makes use of capillary forces to fill a porous material with a liquid precursor spontaneously. Whether or not melt infiltration takes place depends on the degree of wetting and the related contact angle between the liquid and solid. Melt infiltration can be used for the synthesis of materials with a high weight loading. Moreover, since it is a solvent free technique, no drying step or wastewater treatment is needed. However, controlling the distribution of the precursor over the support is less straightforward than when using the synthesis methods mentioned before. Moreover, if lower metal loadings are desired, and thus not the complete pore volume can be filled with the pure metal precursor, some pores might be completely filled, while others are empty. To prevent the uneven distribution of the precursor, the pore volume of the support can (temporarily) be reduced by partially filling the pores with other materials, such as surfactants or polymers [92–94].

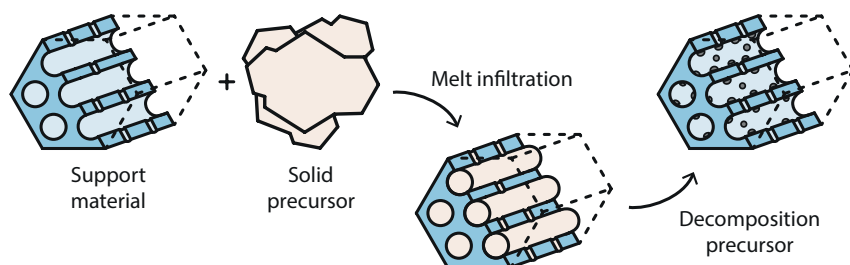


Figure 1.6 Schematic representation of catalyst preparation via melt infiltration. First, the support material and a solid metal precursor is physically mixed, whereupon the composite is heated above the melting temperature of the precursor. The molten precursor will infiltrate the pores of the support material due wetting and capillary forces. After cooling down and solidification, in the next step, the precursor is decomposed and/or reduced to end up with supported metal particles.

A long catalyst lifetime is essential. After preparation, catalysts will encounter harsh reaction conditions when used to catalyze the chemical reactions. Both for the activity and selectivity, it is of great importance that catalysts stay intact. Even though a catalyst is not rapidly consumed during the chemical reaction, it gradually deactivates under reaction conditions [95,96]. There are many different deactivation processes, including particle growth, poisoning, attrition and leaching [96–99]. By finding out which process is dominant for specific catalysts in specific chemical reactions and by understanding the underlying mechanisms, measures to suppress these processes can be implemented more efficiently and the lifetime of a catalyst can be extended. One of the most important deactivation processes is particle growth [96,100,101]. Even particles carefully distributed over a support material will grow in size over time. This growth results from the inherent thermodynamic instability of small metal particles at elevated temperatures and/or pressures [98]. Figure 1.7 gives a schematic representation of the two main mechanisms to describe the sintering process of supported nanoparticles, named particle diffusion and coalescence and Ostwald ripening.

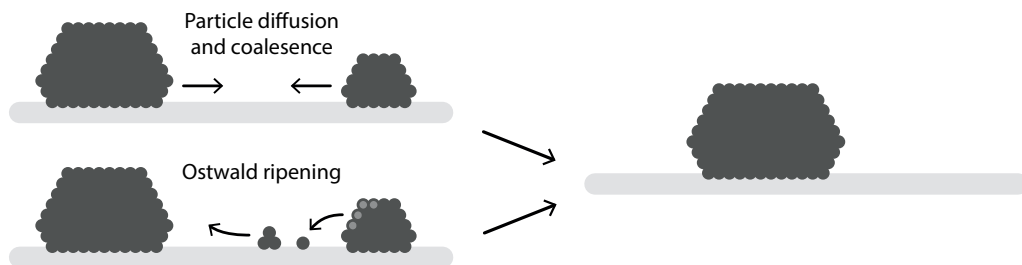


Figure 1.7 Schematic representation on particle growth via particle diffusion and coalescence or Ostwald ripening. In both mechanisms, the growth results in overall larger particles, but the mechanism behind the growth is different.

For particle diffusion and coalescence, particle growth is a result of the mobility of complete metal particles. The particles diffuse over the surface of the support material and when two particles are in close proximity, they merge to form one larger particle [102]. The driving force behind coalescence is the decrease in surface energy, as the overall surface-to-volume ratio decreases when two particles merge [103,104]. An efficient strategy against particle growth via this mechanism is decreasing the chance that two particles come close enough to merge. Therefore, one method to limit coalescence is by confining metal particles in a support pore network [96,105]. Another method is by increasing the interparticle distance, for instance by decreasing the metal weight loading or by using a support with a higher specific surface area [106,107].

In the Ostwald ripening mechanism, particle growth results from the interparticle transport of mobile metal-containing species [102,108]. The transport of these species can take place via the gas/liquid phase or via the support surface [96,104]. As a result of a difference in surface energy between smaller and larger particles, due to the larger specific surface area of the smaller particles, there is a higher concentration of mobile species around the smaller particles. This gives rise to concentration gradients and thus diffusion of these mobile species from smaller particles to larger ones. The size of larger particles increases at the expense of smaller particles, which decrease in size until they ultimately disappear [64,102,108]. In this mechanism, the interparticle distance does not influence particle growth if the formation of the mobile species, or their annihilation by attachment to another metal particle, is rate limiting [109–111]. Only when the diffusion of the mobile metal-containing species is rate limiting, the interparticle distance will have a significant influence. An effective way to limit particle growth via Ostwald ripening is by using catalysts with a narrow particle size distribution, as this decreases the driving force behind the transport of the mobile species [104,106,111–113]. Alternative methods include enhanced metal-support interaction and control over the reaction conditions and the initial particle size to restrict the formation of mobile species [110,114].

Model catalysts are essential. They are used to gain insight into how catalysts can best be prepared, how catalysts enhance the chemical reactions and how the lifetime of a catalyst can be optimized. For heterogeneous catalysts, support materials with an ordered pore structure and a narrow pore size distribution are useful model systems. These materials can be obtained via a (sacrificial) template, as schematically shown in Figure 1.8. After the precursor is distributed

around the template material, it is decomposed to form a stable structure. During this stage, the shape of the template should be kept intact. Next, the template is removed, leaving an inverse replica of the original template.

The pore size, shape and structure depend on the template of choice [115]. For microporous systems with pore sizes below 2 nm, soft templates containing small ions or molecules can be used, while larger molecules, ligands or micelles consisting of long hydrocarbon chain surfactants or block copolymers are ideal candidates for somewhat larger pores, up to circa 30 nm [116–121]. One of these ordered mesoporous supports is SBA-15, a silica material containing cylindrical pores, ordered in a two-dimensional hexagonal structure [121,122]. It has been used extensively as a model support material since its discovery [123–127]. When ordered pores larger than 30 nm are desired, hard templates, such as polymer or silica spheres self-assembled into a colloidal crystal, are practical [128–132]. The use of support materials with ordered pore structures allows advanced characterization and the possibility to deconvolute the metal induced effects from the support morphology effects, while these materials are still very similar to actual catalysts being used in industry [56,107,113,133–139].

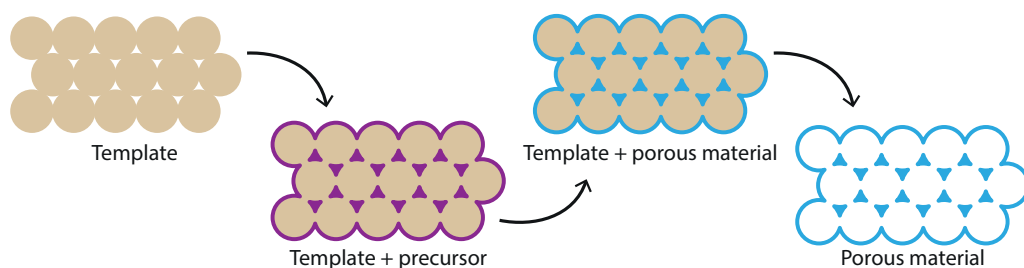
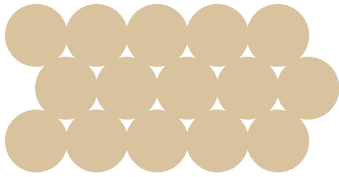


Figure 1.8 Schematic representation of the templated synthesis of a porous material.

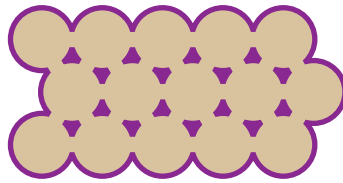
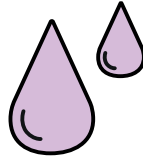
More research on supported silver catalysts is essential. Even though supported silver catalysts are already widely applied in industry, a better understanding and consequent improvement of these catalysts are still needed. For example, alongside the annual 35 million tons of ethylene oxide produced, the estimated annual production of carbon dioxide is circa 28 million tons [8]. Our understanding of this specific reaction is already quite high, but in recent years, more and more research is being performed on this specific epoxidation reaction to even further optimize the ethylene oxide production process [6]. Also for other chemical processes, literature shows the potential of using supported silver catalysts. While the activity of silver in most reactions is limited, the high selectivity towards the desired, but thermodynamically unfavored products, makes further research on supported silver catalysts for these reactions worthwhile [33,34].

In this thesis, the preparation of model support materials is described, alternative catalyst preparation methods for supported silver catalysts are explored and the performance of silver-containing catalysts is investigated in terms of activity, selectivity and stability. Chapter 2 focuses on the preparation of ordered macroporous α -alumina. The preparation of this material is complicated,

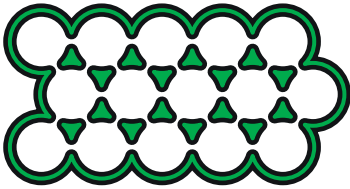
not only by the high temperature needed (1150 °C), but also by the many phase transformations taking place before the α -phase is obtained. Macroporous α -alumina is an interesting support material because of its relatively high surface area and its three-dimensional pore structure, interconnected by windows. This model support material is applied in Chapter 3, where the stability of supported silver particles is evaluated, both using thermal treatments and by investigating their catalytic performance for the epoxidation of ethylene. In Chapters 4 and 5, alternative preparation routes for silica-supported silver catalysts are explored, by making use of in-depth characterization both during the synthesis of the materials, and of the final catalysts. The explored methods are melt infiltration (Chapter 4) and the utilization of supported silver silicate (Chapter 5), and after catalyst preparation, their catalytic performance is investigated for the liquid phase selective hydrogenation of cinnamaldehyde and the gas phase oxidation of carbon monoxide, respectively.



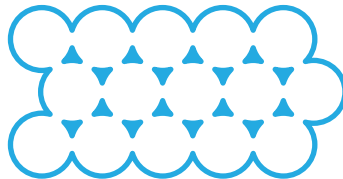
+



$\Delta T, N_2$



$\Delta T, \text{air}$



Chapter 2

Preparation of single phase ordered macroporous α -alumina

Ordered porous materials are highly relevant for applications in fields such as catalysis, adsorption and chromatography. Strategies such as soft and hard templating are now routinely applied to prepare for instance ordered mesoporous silica. In other cases, most notably when several polymorphic phase transformations are involved, achieving high quality ordered oxides is challenging. We present a strategy for the preparation of ordered macroporous α -alumina with a high degree of pore order. The preparation is based on impregnation of ordered polymer spheres with an alumina precursor. Most notably it involves a first heating step in an inert atmosphere, leading to conversion of the polymer template into carbon effectively delaying the phase transitions and stabilizing the pore structure up to high temperatures. A subsequent heat treatment in an oxidative atmosphere then removes the carbon and ordered macroporous α -alumina is obtained with circa 200 nm cages interconnected by windows of circa 100 nm, and a specific surface area of circa 25 m² g⁻¹. Our method led to a strong preservation of the long-range order of the pore structure, as not only evidenced by electron microscopy, but also quantified by spectroscopy. High surface area α -alumina is of particular interest as a catalyst support, but the preparation method might also be extended to other ordered macroporous oxides that are difficult to prepare due to phase transitions such as titania.

2.1 Introduction

Several important porous materials, such as zeolites and clays, occur naturally. However, a great step forward was the synthesis of new classes of porous materials in the laboratory. This started in the 1940s with synthetic zeolites, which are now used on a wide scale as catalysts, softeners and adsorbents [116]. Zeolites are prepared by using small ions or molecules as templates during hydrothermal growth, and hence the pore sizes are typically in the microporous (< 2 nm) regime [116]. Another breakthrough was the first synthesis of ordered mesoporous (2–50 nm) silica (MCM-41), as reported in 1992 [118]. In this case, the mesoporous silica was formed around a template of micelles, consisting of long hydrocarbon chain surfactants or block copolymers [117,118,121]. The mesoporous materials do not consist of crystalline silica, but do have a very well-defined pore ordering, and a very narrow pore size distribution.

Using these soft templating methods, the pore size is limited by the size of the organic templates or their micelles. This provides pore sizes up to roughly 10 nm, with a further extension to circa 30 nm by micelle swelling [117,119,120]. Porous materials with larger pore sizes, such as pores in the macroporous regime (> 50 nm), can be synthesized by using techniques such as foaming, emulsion templating or flame spray pyrolysis [138,140–142], but in these cases the pore size distribution is usually wide and pore ordering is absent or poorly controlled. When ordered macroporous materials are desired, hard templates need to be used [128,129]. Velev *et al.* were the first to report on the preparation of three-dimensionally ordered macroporous silica [132]. Polymer spheres self-assembled into a so-called “colloidal crystal” were used as a sacrificial template, whereupon silica was grown in the voids of these colloidal crystals, followed by template removal. This method proved to work also for other three-dimensional ordered macroporous materials, such as ZnO, Fe₂O₃ and Cr₂O₃ [130,143–146].

While ordered macroporous silica is relatively easily synthesized, the synthesis of ordered porous metal oxide phases that need a high temperature to be formed is challenging [147]. A notoriously difficult compound to synthesize is porous α -alumina, as illustrated for instance by Sadakane *et al.* who prepared a range of ordered materials, but failed to form ordered porous α -alumina [148]. α -alumina is the most stable alumina phase at high temperatures and can be formed from other alumina polymorphs above 1100 °C. The thermal stability and relatively low cost make α -alumina an attractive material for refractories, ceramics and abrasives [149–154]. In principle, due to its chemical and thermal inertness, α -alumina is also very attractive as catalyst support, and indeed the support of choice for catalysts used in large industrial processes such as ethylene epoxidation over a supported silver catalyst [13,155,156]. However, in catalysis, large specific support surface areas (preferably >10 m² g⁻¹) are often crucial, while this is extremely difficult to achieve with α -alumina. Commercial α -alumina exhibits typically a specific surface area of only about 1 m² g⁻¹, with 8 m² g⁻¹ being the highest specific surface area reported [157–159]. The material goes through several crystal phase transitions to form α -alumina from alumina precursors or other alumina polymorphs, which leads to a severe loss in specific surface area [160–162].

Alternative preparation methods for the preparation of high surface α -alumina have been explored. In patent literature, a method is reported involving the incorporation of a carbon template in

γ -alumina followed by two thermal treatments, first in an inert atmosphere to obtain α -alumina and the second treatment in an oxidizing atmosphere to remove the carbon [159]. Similar methods were used by Martin-Ruiz *et al.*, Pérez *et al.* and Furlan *et al.*, in which alumina was formed in the presence of a polymer [163–165]. Using these methods, α -alumina with a specific surface area up to $70 \text{ m}^2 \text{ g}^{-1}$ was produced, but without a well-defined pore size or structure [159]. As far as we are aware, the only successful synthesis of ordered macroporous α -alumina has been reported by Sokolov *et al.*, who used self-assembled poly(methyl methacrylate) (PMMA) spheres as a sacrificial template [166]. Such a polymer template cannot withstand high temperatures in air, but nevertheless ordered macroporous α -alumina was formed at higher temperatures ($1150 \text{ }^\circ\text{C}$), as apparently enough of the template remained during the heating to offer some stabilization of the structure during the phase transitions.

Inspired by these results, we designed a new strategy to prepare high surface area ordered macroporous α -alumina with a very high-quality pore structure. We used self-assembled PMMA sphere crystals to start with as templates, converted the crystals *in situ* into a protective carbon coating, followed by the formation of alumina in the presence of this protective carbon at higher temperatures but still in an inert atmosphere. Subsequently, in a separate oxidative treatment step, the carbon coating was removed and full conversion to α -alumina took place. This strategy allows the formation of high quality ordered macroporous α -alumina material with specific surface areas of $25 \text{ m}^2 \text{ g}^{-1}$, as we evidence in this chapter using detailed electron microscopy and reflectance spectroscopy.

2.2 Experimental methods

2.2.1 Polymer template

Poly (methyl methacrylate) (PMMA) spheres were synthesized by using the surfactant free emulsion polymerization of methyl methacrylate (MMA, 99%, $\leq 30 \text{ ppm}$ 4-methoxyphenol inhibitor, Sigma-Aldrich) in water. Following the procedure of Zhou *et al.* and Schrodin *et al.*, 100 mL MMA and 400 mL demineralized water in a 1 L round bottom flask were stirred by an overhead stirrer at 450 rpm [131,167]. The emulsion was heated to $70 \text{ }^\circ\text{C}$ and nitrogen was bubbled through the emulsion for at least 30 min to remove dissolved oxygen from the dispersion and to deactivate the inhibitor. Thereafter, 69 mg potassium persulfate (KPS, initiator, 99+%, Emsure) was added, resulting in a 0.5 mM concentration. The emulsion was left to react for 3 h at $70 \text{ }^\circ\text{C}$ after which a white dispersion had formed. The dispersion was allowed to cool down to room temperature and was filtered to remove larger chunks of polymer. The filtrate was centrifuged for 1 h at 3000 rpm during which a white solid precipitated. The clear supernatant was decanted, and the obtained white powder was left to dry for several days at room temperature in air after which it was crushed into a powder.

2.2.2 Ordered macroporous alumina

Three-dimensionally ordered macroporous α -alumina was obtained by impregnation of the polymer template with an alumina precursor [131,168]. In a typical synthesis, circa 1.5 g template powder was placed in a Büchner funnel and dropwise approximately 3 mL solution of 1 M aluminum nitrate

nonahydrate (99+%, Acros) in demineralized water/methanol (1:1 volume ratio) was added to completely wet the template. After 2 min of soaking, a dynamic vacuum was applied for 20 min to remove excess solvent. Subsequently, the dry powder was wetted with circa 3 mL ammonia (28–30%, Emsure)/methanol (99.9%, VWR) (1:1 volume ratio) to form aluminum hydroxide in the pores of the template. Again, the material was dried via vacuum suction for 20 min. In order to obtain sufficient filling of the pores, these steps were performed one, three or four times before drying the powder overnight at room temperature in air [131,168]. Note that to maximize the pore filling, each impregnation consisted of two different steps: firstly, an impregnation with an $\text{Al}(\text{NO}_3)_3 \cdot 9\text{H}_2\text{O}$ solution and secondly a washing with an ammonia solution to form $\text{Al}(\text{OH})_3$. After the impregnation rounds, the powder was left to dry overnight at room temperature in air.

The once and four times impregnated template materials were calcined in a flow of air of at least 0.5 L min^{-1} ($\text{GHVV} = 20 \text{ L g}_{\text{template}}^{-1} \text{ hr}^{-1}$), at $1150 \text{ }^\circ\text{C}$ ($5 \text{ }^\circ\text{C min}^{-1}$ heating ramp) and kept at this temperature for 6 h, in a similar fashion to established procedures [131,166,168]. The resulting samples were labeled 3DOM_1_air and 3DOM_4_air, indicating the number of impregnation steps and the gas atmosphere respectively (see Table 2.1). 1.5 g of dry, three times impregnated material was heated under a nitrogen flow to $1150 \text{ }^\circ\text{C}$ for 6 h ($5 \text{ }^\circ\text{C min}^{-1}$ heating ramp) The resulting material was black, or dark blue/green and a second heat treatment in a flow of air with the same flow and temperature program was applied after which a pristine white powder was obtained. The resulting sample was labeled 3DOM_3_N₂_air. For temperature studies, the impregnated material was heated separately in an air or nitrogen flow for 6 h at 200, 400, 600, 800, 1000 and $1150 \text{ }^\circ\text{C}$.

Table 2.1 Overview of the synthesis parameters for three-dimensionally ordered macroporous alumina (3DOM) samples, labeled in the form 3DOM_#_HT, with # being the number of impregnation steps and HT the applied heat treatment(s).

Sample	Number of impregnation steps	Heat treatment(s)
3DOM_1_air	1	Air
3DOM_4 _air	4	Air
3DOM_3_N ₂ _air	3	Nitrogen and air

2.2.3 Characterization

The polymer template and alumina powders were analyzed using scanning electron microscopy (SEM) with a FEI XL30 FEG operated at 15 kV, and FEI Helios G3 UC operated at 2 kV. SEM samples were prepared by attaching the sample powder to the sample holder by sticky carbon tape. Prior to the measurements, a 7.5 nm platinum layer was deposited over the sample via sputter coating. Diffuse-Reflectance Ultraviolet/Visible (DR UV/Vis) spectra of the materials were obtained using a Varian CARY 500 Scan UV/Vis-NIR spectrophotometer with an integrating sphere detector. In a typical analysis of the ordered macroporous materials, 30 mg of analyte was diluted with 600 mg pristine $\alpha\text{-Al}_2\text{O}_3$ ($1 \text{ m}^2 \text{ g}^{-1}$, 100 mesh, Sigma-Aldrich) and ground into a fine powder before taking a spectrum of the 1000–200 nm range. A background measurement

of pristine $\alpha\text{-Al}_2\text{O}_3$ was taken which was automatically subtracted from the obtained spectrum. Crystal phase analysis was performed with X-ray diffraction (XRD) on a Bruker D8 Phaser diffractometer equipped with a Co K_α source ($\lambda = 0.1789$ nm). The composite structures were analyzed by comparing diffractograms with crystal structures from the PDF-4+ 2016 database. Crystallite sizes were estimated using the Scherrer equation [169,170]. Nitrogen physisorption isotherms were measured at -196 °C on a Micromeritics TriStar 3000 apparatus. The specific surface area of the support was calculated using the BET equation ($0.05 < p/p_0 < 0.25$). Mercury porosimetry was performed using a Micromeritics AutoPore IV 9500 in the Chemical Reactor Engineering group at the Eindhoven University of Technology. Pore volume data were calculated over the range 0.0007–227.5270 MPa, assuming a contact angle between the support materials and the mercury of 130 ° and mercury surface tension and density of 485 dynes cm^{-1} and 13.5335 g cm^{-3} , respectively.

2.3 Results and discussion

2.3.1 Polymer template

In Figure 2.1, Frame A, a scanning electron microscopy (SEM) image of the polymer template after centrifugation and drying is shown. In the inset, a histogram of the sphere diameter is added. The number-averaged sphere size is 400 ± 24 nm. The monodispersity of the particle sizes can be seen from the histogram and from visual inspection of the image. The deposition of the spheres was relatively slow, allowing the formation of a hexagonally ordered structure (a “crystal”) as a close packing minimizes the energy of the system.

Diffuse-Reflectance Ultraviolet/Visible (DR UV/Vis) spectroscopy showed that the closed packed ordering of the polymer spheres is not only present at the surface, but also at the center of the colloidal crystal particles. In the DR UV/Vis spectrum (Figure 2.1, Frame B), three peaks are visible. Assuming a closed packed ordering of the polymer spheres, the two most intense peaks at 895 and 450 nm are assigned to second and first order diffraction of the nearest neighbor spheres in a close packed structure ((222) and (111) crystal planes), while the least intense peak

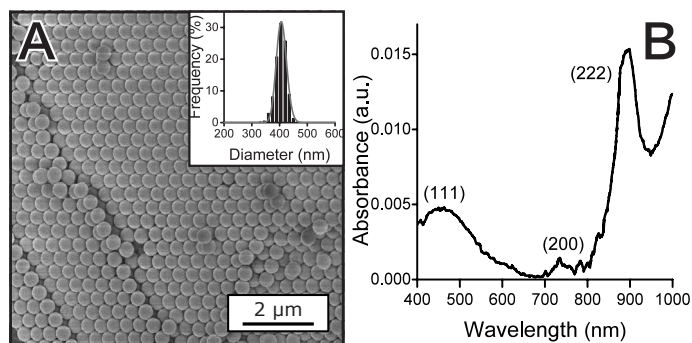


Figure 2.1 SEM image with a histogram of the particle size distribution in the inset (A) and DR UV/Vis spectrum of polymer template (B). The SEM image shows PMMA spheres with an average diameter of 400 ± 24 nm ordered in a colloidal crystal. The UV/Vis spectrum shows peak positions at 450, 780 and 895 nm, corresponding to the (111), (200) and (222) plane reflections of the PMMA spheres, respectively.

(780 nm) corresponds to the second order next nearest neighbor diffraction (200). By assuming a closed packed crystal structure, an average sphere diameter of 404 ± 20 nm was calculated (see Appendix A, Section I), which is in agreement with the number-averaged particle size obtained via SEM analysis.

2.3.2 The formation of macroporous α -alumina

The polymer template was used to synthesize macroporous α -alumina. Upon heat treatment of the impregnated template in air, the aluminum hydroxide in the voids of the template decomposes and the template is burned off. Upon decomposition of aluminum hydroxide at 400°C , first γ -alumina is expected to form, while α -alumina should be formed above 1100°C [160,171]. To understand the effect of the confinement of the hydroxide on the phase transitions, we first evaluated the crystalline phases of alumina in the voids of the template using X-ray diffraction (XRD). In Figure 2.2, Frame A, the diffractograms of the composite treated at different temperatures in air are shown. At the bottom of the frame, the diffractogram of the impregnated template before heating is shown, displaying two broad diffraction peaks attributed to the PMMA polymer [172]. With increasing temperature, both the aluminum hydroxide and the polymer peaks disappear and at 600°C , no diffraction peaks are visible. Broad peaks from γ -alumina appear at 800°C [133,163]. The broad diffraction peaks indicate that the material consists of relatively small crystallites with sizes of 5 ± 1 nm. These peaks disappear in favor of peaks that are attributed to crystalline α -alumina, which sharpen upon heating to 1150°C .

The disappearance of the broad diffraction peaks attributed to the polymer material at 200 – 400°C is in accordance with thermal gravimetric analysis of the material (see Appendix A, Figure A.1), showing that in this temperature range, the template is burned off. The presence of γ -alumina at 800°C and α -alumina above 1000°C is in accordance with the alumina phase diagram [173,174]. However, the conversion of confined aluminum hydroxide in the voids of the template into γ -alumina is delayed by 400°C . We believe that this delay is caused by residual template material present at least up to 600°C .

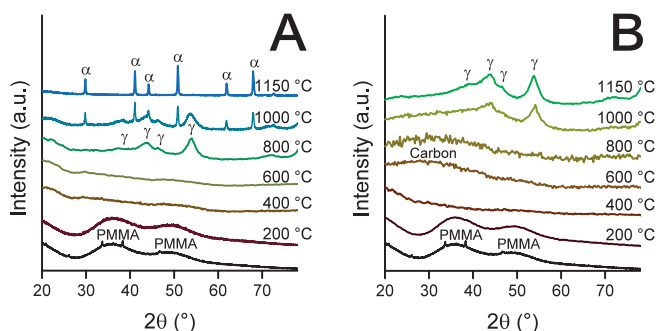


Figure 2.2 Diffractograms of the impregnated template treated at different temperatures in air (A) or under a nitrogen flow (B). After the material was treated at 800°C in air, γ -alumina was formed, converting into α -alumina at higher temperatures. Under inert atmosphere, the formation of γ -alumina was delayed to even much higher temperatures and no α -alumina was yet formed at 1150°C . The diffractograms are offset for clarity.

In Figure 2.2, Frame B, the diffractograms of the impregnated template heat treated under a nitrogen flow are shown. The diffractogram of the composite heated to 200 °C is very similar to the diffractogram taken before heat treatment. By heating the composite in a nitrogen flow, the decomposition of the polymer template is delayed compared to when the composite is heat treated in air. When the composite is treated to 400 °C, these broad peaks have disappeared and after heating to 600 °C, another broad peak is visible at 30 °. This peak was not observed in the material treated in air and is attributed to a carbon material, formed due to pyrolysis of the polymer template. The broad peak is still present in the composite heated at 800 °C, and next to this peak, no other peaks are visible.

The appearance of γ -alumina is delayed to 1000 °C and this phase is still present after heat treatment at 1150 °C. Even after prolonged heating (6 h) at 1150 °C, no crystalline α -alumina was observed. We postulate that the delay in phase transitions is caused by the presence of the formed carbon. Causing a delay in a phase transition is only possible when the carbon and alumina are in close contact. This ensures that carbon can act as a protective layer to stabilize the pore structure even at 1150 °C. The pyrolysis of the template material into a protective carbon coating is supported by the black color after the heat treatment in a nitrogen flow at 1150 °C (see Appendix A, Figure A.2). Since at this temperature no α -alumina was formed, carbon free ordered macroporous γ -alumina with a high-quality pore structure can be obtained by simply burning off the carbon at 900 °C in an oxidizing atmosphere (route 2 in Figure 2.3 and see Appendix A, Figures A.3 and A.4). Alternatively, the carbon-coated γ -alumina can be used as a ceramic with altered dielectric properties [175]. Next to the ordered macropores, also some pores in the range of 30–90 μm were present in the obtained γ -alumina. The surface area of this material was $85 \pm 10 \text{ m}^2 \text{ g}^{-1}$. By increasing the temperature of the second heat treatment in an oxidizing atmosphere to 1150 °C, ordered macroporous α -alumina was formed (route 3 in Figure 2.3 and

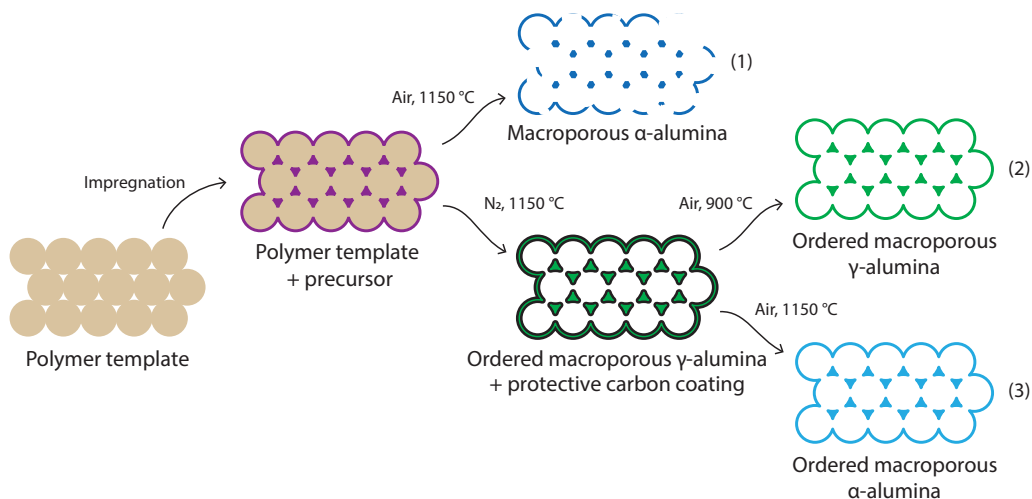


Figure 2.3 Schematic representation of the synthesis procedures of three-dimensionally ordered macroporous α -alumina by reference procedure (1) and the procedures described in this chapter for γ -alumina (2) and α -alumina (3).

see Appendix A, Figure A.5). Although the carbon was burned off before the transformation of γ -alumina to α -alumina, the pore structure was well preserved in the α -alumina, better than in the case of treating impregnated template material in an oxidizing atmosphere directly (route 1 in Figure 2.3), as will be discussed in more detail below.

By increasing the number of impregnation steps, the yield of the ordered macroporous material was increased. The synthesis of the reference material (3DOM_1_air) yielded $20 \pm 1 \text{ mg g}_{\text{template}}^{-1}$, which corresponds to circa 2% of the total pore volume of the template material being filled. The yields for 3DOM_4_air and 3DOM_3_N₂_air were 40 and 30 $\text{mg g}_{\text{template}}^{-1}$, respectively, and are hence significantly higher. Increasing the number of impregnation steps clearly increases the yield of this procedure, but cannot lead to full pore filling with alumina, as the volume of the precursor ($\text{Al}(\text{NO}_3)_3 \cdot 9\text{H}_2\text{O}$) is much higher than the volume of its decomposition product, $\text{Al}(\text{OH})_3$, and the final alumina phase. When taking this decrease in volume into account, the maximum achievable yield (assuming 100% pore filling using a single impregnation with $\text{Al}(\text{NO}_3)_3 \cdot 9\text{H}_2\text{O}$) is $63 \text{ mg g}_{\text{template}}^{-1}$. After 4 impregnation steps, we reached 60% of this theoretical value.

2.3.3 Quality of the pore structure

A crucial part of our strategy for improving the quality of the ordering and pore structure is by stabilizing the morphology by pyrolysis of the template material into a protective carbon coating. Next to that, we investigated the effect of increasing the number of impregnation steps on the quality of the pore structure. Several techniques were applied to investigate the effect of our strategy on the quality of the prepared macroporous α -alumina. Nitrogen physisorption and mercury intrusion measurements on 3DOM_3_N₂_air (see Appendix A, Figures A.6 and A.7) showed a specific surface area of $25 \pm 10 \text{ m}^2 \text{ g}^{-1}$, originating from macropores, while micro- and mesopores are absent. This is a very high specific surface area for α -alumina materials and in good agreement with the theoretically expected value of $14 \text{ m}^2 \text{ g}^{-1}$ for the hexagonal ordered macroporous structure (see Appendix A, Section V).

In Figure 2.4, SEM images of 3DOM_1_air, 3DOM_4_air and 3DOM_3_N₂_air are shown. Frames A, D and G give an overview of the material, while the other frames show images taken at higher magnifications. We tried to show both the best (Frames B, E and H) and the worst parts (Frames C, F and I) of the samples. In Frame A, long-range ordering in the 3DOM_1_air sample is visible in the overview image. However, the material consists of sheets of alumina instead of the expected cage-structure, as can be better observed at higher magnifications (Frame C). In Frame B, a higher magnification of another section of the material does show the expected morphology, but this morphology co-exists with the sheets visible in the overview and at higher magnification in Frame C. These observations suggest that the sheets originate from the cage structure, which deformed during phase transitions at high temperature as also observed in the original paper by Sokolov *et al.* [166].

3DOM_4_air is displayed in Frames D–F. Frame D shows the desired hexagonal cage-structure, although in Frame E, the cage structure appears to be slightly split, forming an intermediate morphology between the sheets observed in the 3DOM_1_air sample and the desired cage

morphology. In Frame F, no sheets are visible, but also no fully formed cages are observed. The material resembles a stick-and-node structure, with some absent sticks on the surface of the material, similar to observations from Rudisill *et al.* [147]. In Frames G–I, showing the sample prepared by the two-step approach, the cage structure of 3DOM_3_N₂_air is visible throughout the sample (Frame G) and a clear hexagonal ordering is visible at higher magnifications (Frame H). Even for those parts of the material in which the morphology is least preserved (Frame I), the cages of the material are enclosed by a well-defined stick-and-node structure, and the cage structure is overall preserved.

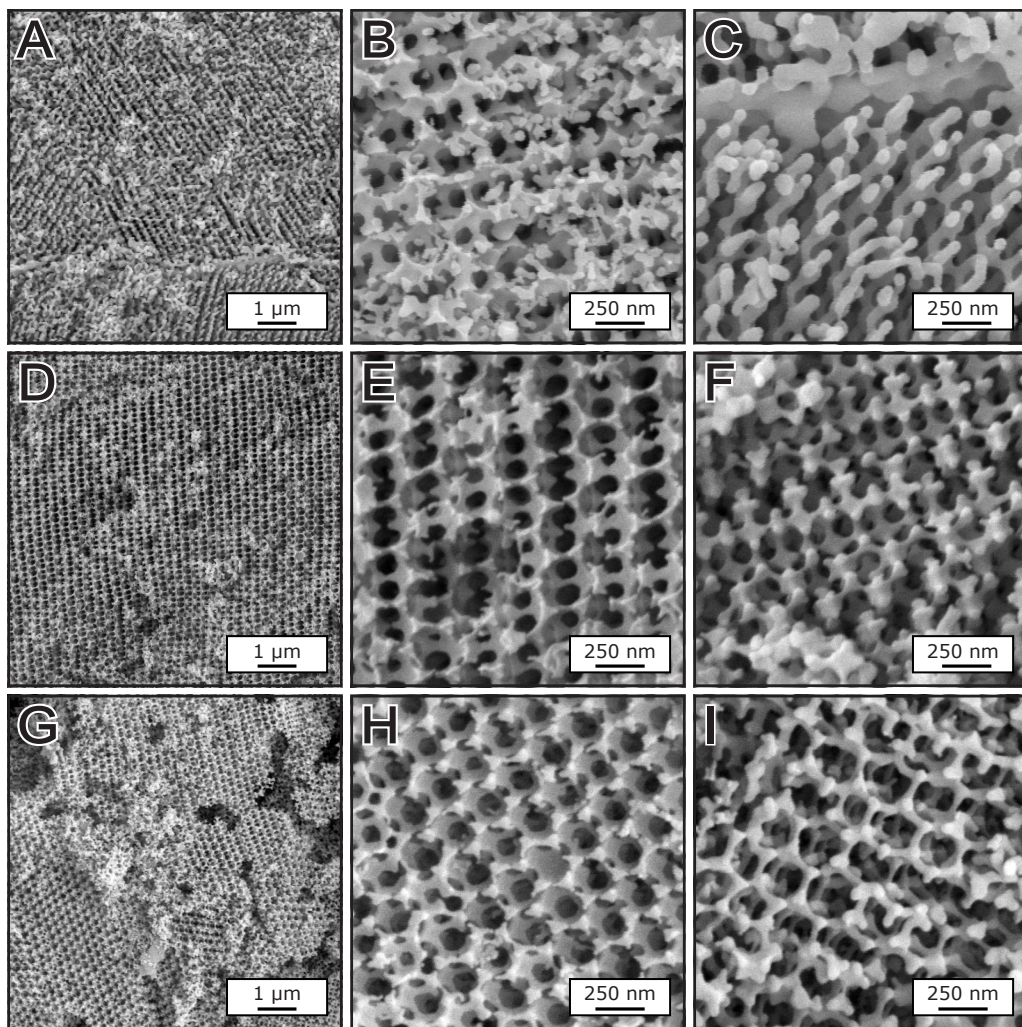


Figure 2.4 SEM images of macroporous α -alumina 3DOM_1_air (A–C), 3DOM_4_air (D–F) and 3DOM_3_N₂_air (G–I). In 3DOM_3_N₂_air, pores of 220 ± 15 nm are connected by windows of circa 105 ± 5 nm, resulting in a cage structured material. For 3DOM_4_air and 3DOM_1_air, the cage structure is not as well preserved, as alumina migrated from the walls of the cages to form pillars.

From SEM it appears that increasing the number of impregnation steps increases the quality pore structure of the final macroporous α -alumina in comparison to the 3DOM_1_air sample. In the images in Figure 2.4, the loss of the desired cage structure in these samples seems to result from the transport of the alumina from the thin to the thicker sections of the cage morphology, resulting in a loss of the cage morphology [147,166,176–178]. This transport towards the thicker parts of the structure is driven by the minimization of the surface area. A comparable loss of pore structure was observed for other microporous materials [147,176]. In the worst case, this transport results in some cages no longer having a wall separating them, or in the formation of α -alumina sheets.

When following our new strategy, the ordered macroporous structure is supported by the protective carbon coating, such as in 3DOM_3_N₂_air, and the resulting material retains the cage structure. As a result, the pore structure is far better than if this carbon coating had not been formed. While the morphology is maintained to a higher degree, the different preparation routes do not have a significant influence on the pore sizes. An average pore size of circa 220 ± 15 nm was measured. The windows and walls are respectively 105 ± 5 nm and 35 ± 5 nm. The pore sizes are significantly smaller in the resulting macroporous material than the size of the polymer template (400 nm spheres). For all three samples, the reduction of the pore size is similar as they are derived from the same template material. Additional SEM, focused ion beam SEM and transmission electron microscopy images in which the pore structure at a larger scale and the pore structure on the inside of the particle are visualized are given in Appendix A, Figures A.8 and A.9.

While electron microscopy can illustrate the degree of ordering and how well the desired morphology is maintained, a reliable and statistically relevant method is required to validate these results. Ordering in the macroporous material results in peaks in DR UV/Vis spectra [131,142,175,179,180]. The position of these reflectance peaks reflects the size of the unit cell, the morphology of the ordered structure and the average refractive index of the sample. The latter is determined by the relative amounts of the material (volume fraction), in this case α -alumina, and the liquid or gas in the pores of the structure. The dependencies can be expressed in the Bragg equation, given in Equation 2.1. Here, the interplanar distance is represented by d_{hkl} , the peak position as λ , the diffraction order as m and the average refractive index as $n_{\text{material,avg}}$. The width and intensity of peak is determined by the quality of the ordered structure.

$$D = \frac{m \cdot \lambda}{2 \cdot d_{hkl} \cdot n_{\text{material,avg}}} \quad (2.1)$$

In Figure 2.5, the DR UV/Vis spectra of the three ordered macroporous α -alumina materials (3DOM_1_air, 3DOM_4_air and 3DOM_3_N₂_air) are shown. Results from the samples measured in air are shown in Frame A. The positions of the reflectance peaks in this frame are similar for all three samples. The reflectance peaks of 3DOM_1_air and 3DOM_4_air spectra do not differ visibly, both exhibiting a shallow peak at 500 nm. The spectrum of 3DOM_3_N₂_air exhibits a sharp peak at the same position.

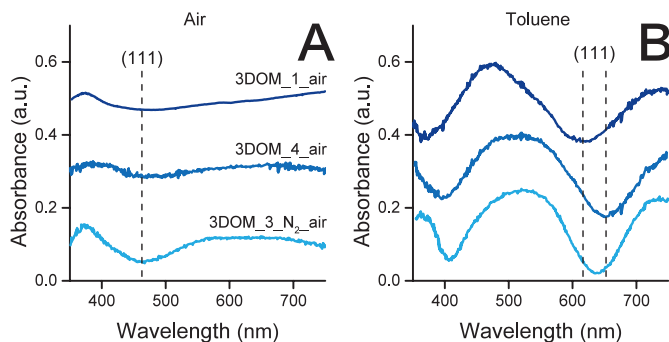


Figure 2.5 DR UV/Vis spectra of macroporous α -alumina 3DOM_1_air (top), 3DOM_4_air (middle) and 3DOM_3_N₂_air (bottom) in air (A) and toluene (B). A redshift of the reflection minima is observed in toluene due to a change in refractive index. The spectra are offset for clarity.

To allow for a better distinction between the spectra of the three samples, especially between the 3DOM_1_air and 3DOM_4_air samples, the DR UV/Vis spectra of these samples were also measured after filling the pores with toluene (Figure 2.5, Frame B). When the spectrum is measured in toluene, the reflectance peaks are more intense and redshifted, due to the higher density of toluene compared to air and the larger refractive index, respectively. The (111) reflection peaks that were visible when the measurements were performed in air (Frame A) are shifted to 600–650 nm while additional peaks for (220) reflections appear at 350–400 nm, due to this redshift. The redshift in 3DOM_1_air is less than the shift in the two other materials and similarly, the reflectance peaks of 3DOM_1_air are clearly less sharp and less intense than the peaks from both 3DOM_4_air (red) and 3DOM_3_N₂_air (green).

As shown by Blanford *et al.*, from the red shift of the refractive peak, a number of material characteristics can be derived, which together with the full width at half maximum (FWHM) describe the quality of the morphology of the material [180]. These characteristics are summarized for the three ordered macroporous α -alumina materials in Table 2.2. Using the position of the d_{111} reflectance peak in air ($n = 1$), butanol ($n = 1.3991$) and toluene ($n = 1.4941$), the interplanar distance (d_{111}) and the volume fraction of alumina (φ) can be calculated using the linearized Bragg equation (Equation 2.2), while the cage size (D) can in turn be derived from the interplanar distance [180]. In this equation, the d_{hkl} peak position (λ), diffraction order (m), volume fraction solid material (φ) and refractive index of the solid wall (n) are represented. The refractive index of the wall is assumed to be 1.7682, equal to the refractive index of bulk α -alumina [181].

$$\lambda = \frac{2 \cdot d_{hkl}}{m} \cdot \varphi \cdot n_{\text{wall}} + \frac{2 \cdot d_{hkl}}{m} \cdot (1 - \varphi) \cdot n_{\text{solvent}} \quad (2.2)$$

No significant increase in the volume fraction and the cage sizes was observed with increasing impregnation steps (Table 2.2). Taking into account that with SEM the pore size was measured, but with using DR UV/Vis the calculated size includes the wall thickness (of 35 ± 5 nm), the sizes measured with the different techniques are in good agreement.

Table 2.2 Material characteristics for the ordered macroporous support materials, derived from DR UV/Vis in solvents (air, butanol and toluene) and Equation 2.2.

Sample	3DOM_1_air	3DOM_4 _air	3DOM_3_N ₂ _air ^a
Volume fraction of alumina, φ	0.18 \pm 0.02	0.14 \pm 0.01	0.16 \pm 0.02
Interplanar spacing, d_{111} (nm)	206	208	211
Calculated cage (+ wall) size, D (nm) ^b	252	255	259
FWHM in toluene (cm ⁻¹)	3433	2700	2286

^a 3DOM_3_N₂_air measured in air, butanol, methanol and toluene.

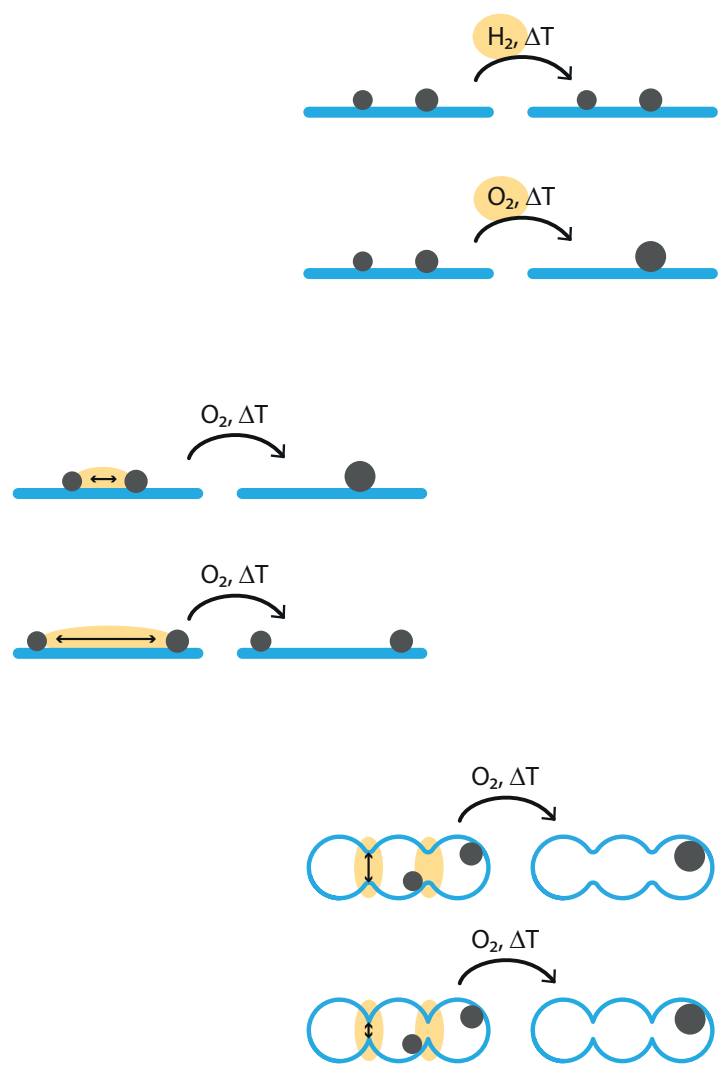
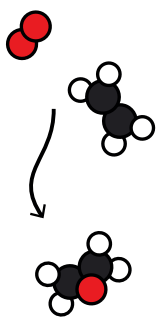
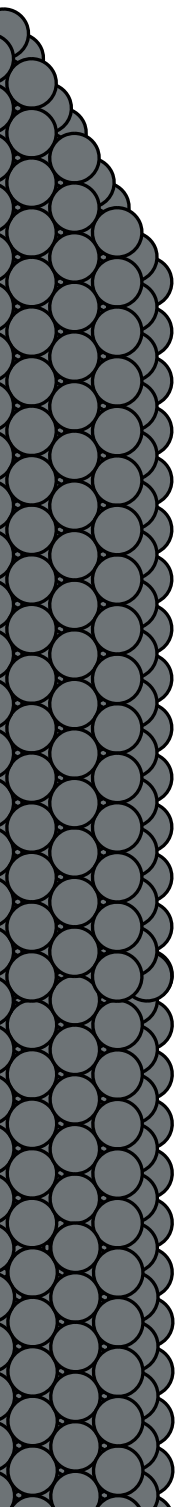
^b Assuming closed packed arrangement of the pores.

Most importantly, the full width at half maximum (FWHM) of the refractive peak is a measure for the degree of ordering of the porosity in the material. A sharp peak is indicative of a better ordered material. The decrease in FWHM with both the number of impregnation steps and the additional protective carbon coating is striking. This decrease shows that both adjustments result in better ordering compared to the 3DOM_1_air reference material. The FWHM for 3DOM_3_N₂_air is even similar to the FWHM of ordered macroporous γ -alumina in methanol described in literature [180]. Hence this suggests that with our new two-step approach α -alumina can be made with a similarly high quality as the γ -alumina of Blanford *et al.*, despite the extra phase transformation step.

Having a very high surface area α -alumina support is of particular interest in catalysis, as it is notoriously difficult to obtain such high surface areas by known methods. High surface areas serve to better stabilize the active supported metal particles, even more so if the pore structure is cage-like [133,182]. The preparation strategy proposed in this chapter could be relevant also for other ordered macroporous materials that are difficult to prepare due to phase transitions, such as titania [99,183].

2.4 Conclusions

We demonstrate a method for the synthesis of high quality, high surface area ordered macroporous α -alumina, based on impregnation with aluminum hydroxide of an ordered polymer template. Multiple impregnating steps contribute to a high degree of pore filling with aluminum hydroxide, increasing the yield of the synthesis and minimizing the loss of ordering. We employed a specific heat treatment in an inert atmosphere to convert the polymer template into a protective carbon coating. Close contact of the protective carbon coating with the alumina surface caused a delay of the alumina phase transitions to higher temperatures and helped to preserve the pore structure. By a final heat treatment in air, the carbon was removed, and high quality ordered macroporous α -alumina with a specific surface area of circa 25 m² g⁻¹ was obtained. The high quality of the pore structure was evidenced by electron microscopy and quantified by spectroscopic analysis.



Chapter 3

Stability of silver on α -alumina for ethylene epoxidation

The stability of supported metal particles is an important parameter in heterogeneous catalysis. For silver catalysts supported on α -alumina, industrially used in ethylene epoxidation, the loss of silver surface area as a result of particle growth is one of the most important deactivation mechanisms. In this work, the growth of silver particles was investigated by exposing catalysts to thermal treatments. The presence of oxygen during heating strongly enhanced particle growth, and the interparticle distance was a crucial parameter. However, restricting the movement of complete silver particles using cage-like α -alumina did not limit particle growth. These findings indicate that Ostwald ripening was the dominant mechanism behind particle growth, with the diffusion of oxidized silver species being a rate limiting factor. Finally, higher surface area α -alumina provided better silver stability during ethylene epoxidation, with only a limited decrease in selectivity. This makes silver supported on high surface area α -alumina promising candidates for ethylene epoxidation catalysis.

3.1 Introduction

The activity of catalysts gradually decreases over time. By gaining information on how deactivation occurs, the stability of the catalyst, and thus the lifetime can be improved [95,96]. Most deactivation of supported catalysts results from the loss of active surface area, which can be chemically, mechanically or thermally induced [96–99]. One example of the thermally induced loss of active surface area is the growth of the active metal particles. For α -alumina-supported silver catalysts, used for the epoxidation of ethylene, this is one of the most important deactivation mechanisms [100,101,184].

Silver is the sole metal commercially used as catalyst for the epoxidation of ethylene [3,7,156]. The mild oxidation properties of silver allow selective oxidation of the ethylene into ethylene oxide, instead of fully oxidizing ethylene to carbon dioxide and water [5,13,185,186]. The activity of the silver is particle size dependent, as the turnover frequency increases with the particle size up to circa 60 nm [48–51]. Above this size, the turnover frequency is constant, which makes 60 nm the optimum size for the silver particles. The silver particles are generally supported on α -alumina with a low specific surface area (circa $1 \text{ m}^2 \text{ g}^{-1}$) [155,156,187–189]. The low density of hydroxyl groups present on the surface of α -alumina is beneficial in terms of selectivity, as the undesirable further conversion of ethylene oxide to carbon dioxide and water is relatively easy, and is facilitated by these hydroxyl groups [13–16]. The combination of the low density of hydroxyl groups on the surface and the low specific surface area of α -alumina minimizes the number of these hydroxyl groups [157]. However, the low surface area of the support, especially in combination with the harsh ethylene epoxidation reaction conditions and the relatively low Tamman temperature of silver (circa $340 \text{ }^\circ\text{C}$), makes the silver particles vulnerable to growth [50]. Therefore, instead of having silver particles with the optimal size of circa 60 nm, particle sizes in the range of 100–1000 nm are more common in industrial catalysts [155,187].

Particle growth results from the inherent thermodynamic instability of small metal particles distributed over the support at elevated temperatures and/or pressures [98]. For most chemical reactions, the growth of metal particles can be ascribed to either Ostwald ripening or particle diffusion and coalescence. In Ostwald ripening, particle growth is driven by the interparticle transport of mobile metal-containing species [102,108]. The transport of these species can both take place via the gas/liquid phase or via the support surface. For particle diffusion and coalescence, particle growth is a result of the mobility of complete metal particles. The particles diffuse over the surface of the support material and when two particles are in close proximity, they merge to form one larger particle [102].

To gain insight into to which particle growth mechanism is dominant, model systems are essential. Thanks to the use of model catalysts, the mechanism behind particle growth is now fairly well understood for many systems containing supported metal particles [56,107,113,136]. One example is the growth of copper particles supported on silica, where after carefully tuning both the ordered pores of the support material, and the particle size distribution of the copper, the dominant growth mechanism under specific conditions was identified [113]. However, the dominant mechanism behind the particle growth of supported silver particles in the epoxidation

of ethylene is still under debate [190–193]. Recently, in an advanced electron microscopy study on the silver dispersion during ethylene epoxidation, particle growth via Ostwald ripening was put forward [194].

In this chapter, we systematically investigate which parameters influence the mobility of silver on α -alumina for the epoxidation of ethylene, by analysis of particle growth after subjecting the catalysts to thermal treatments under various conditions. Besides commercially available α -alumina support materials, we also made use of porous, ordered α -alumina materials with a high specific surface area that was described in Chapter 2. This material is an excellent model support for investigating the stability of supported silver particles, especially since the cage and window sizes of the pores present in the α -alumina are adjustable. Finally, next to the thermal treatments, also the catalytic performance of these materials in the epoxidation of ethylene is investigated.

3.2 Experimental methods

3.2.1 Macroporous α -alumina

Three different types of α -alumina materials were used as support. Next to the commercially available α -alumina materials from Sigma-Aldrich ($1 \text{ m}^2 \text{ g}^{-1}$, 100 mesh) and BASF ($8 \text{ m}^2 \text{ g}^{-1}$, Al-4196E), ordered macroporous α -alumina materials were synthesized, following the procedure for 3DOM_3_N₂_air, as described in Chapter 2, Section 2.2. Macroporous α -alumina with different pore sizes were prepared by making use of polymer spheres with number-averaged diameters of 400, 315 or 280 nm to prepare the sacrificial polymer templates. These polymer spheres were prepared by using respectively 2.3, 1.4 and 0.9 mol L^{-1} methyl methacrylate, $8.4 \mu\text{mol L}^{-1}$ potassium persulfate and a reaction temperature of $80 \text{ }^\circ\text{C}$ during the surfactant free emulsion polymerization:

3.2.2 Silver deposition

Silver was deposited on the α -alumina materials via incipient wetness impregnation, following a literature procedure [48,195]. The silver precursor, silver oxalate, was freshly prepared each time. Silver oxalate was synthesized by mixing an aqueous solution of oxalic acid dihydrate (99.5%, Merck) with an aqueous solution of silver nitrate (99+%, Sigma-Aldrich) (1:2 mol ratio). Next, the silver oxalate was obtained via centrifugation and washed three times with milliQ water (1:20 volume ratio) to remove any unreacted silver nitrate. Finally, the silver oxide was dried overnight in static air at $60 \text{ }^\circ\text{C}$. The support powders ($38\text{--}400 \mu\text{m}$) were dried under vacuum at $120 \text{ }^\circ\text{C}$ for 2 h before they were impregnated with a solution (90% of the pore volume) of silver oxalate in demineralized water/ethylene diamine (99%, Sigma-Aldrich) (1:0.73 vol ratio) to obtain materials with a theoretical loading of 0.6, 4.5 or 15 wt% silver. The materials were dried overnight in air at $60 \text{ }^\circ\text{C}$ and after 5, 10 and 30 min of drying, the materials were thoroughly mixed. The precursor was decomposed via a heat treatment at $215 \text{ }^\circ\text{C}$ for 2 h ($5 \text{ }^\circ\text{C min}^{-1}$ heating ramp) in an oxygen, hydrogen or nitrogen flow (see Section 3.3.2, Table 3.2).

3.2.3 Characterization

The pore volume and surface area of the α -alumina materials were analyzed using nitrogen physisorption. Isotherms were measured at $-196\text{ }^{\circ}\text{C}$ on a Micromeritics TriStar 3000 apparatus. The specific surface area of the support was calculated using the BET equation ($0.05 < p/p_0 < 0.25$). The surface density of acid sites on the α -alumina materials was determined by temperature programmed desorption (TPD) of ammonia, using an Autochem II 2920 V4.03 apparatus from Micromeritics. Prior to the TPD measurement, circa 100 mg α -alumina was treated at $400\text{ }^{\circ}\text{C}$ in air for 15 min (50 mL min^{-1}), then treated to 10% ammonia in helium for 20 min at $100\text{ }^{\circ}\text{C}$ (25 mL min^{-1} STP). For the TPD measurement, the sample was heated from 100 to $550\text{ }^{\circ}\text{C}$ ($10\text{ }^{\circ}\text{C min}^{-1}$ heating ramp) in a helium flow (25 mL min^{-1}). The amount of desorbed ammonia was monitored using a thermal conductivity detector (TCD) and used to calculate the total number of acid sites. For this, the complex peak shape was deconvoluted and fitted with three Gaussian peaks, of which the total area was used to calculate the surface density of acid sites. The support materials and silver-containing materials were analyzed by scanning electron microscopy (SEM) using a FEI XL30 FEG and Helios microscope operated at 5–10 kV. SEM samples were prepared by attaching the sample powder to the sample holder by sticky carbon tape. Prior to the measurements, a 7.5 nm platinum layer was deposited over the sample via sputter coating. In the SEM images, the silver particles were identified and their diameter was determined manually. For this we counted for each sample at least 200 different particles in at least three different places. The surface-averaged particle sizes ($d_{p,s}$) and the standard deviations in the width of the particle size distribution ($\sigma_{p,s}$) were calculated using the following Equation 3.1, with n the number of silver particles counted, and d_i the size of particle i .

$$d_{p,s} \pm \sigma_{p,s} = \frac{\sum_{i=1}^n d_i^3}{\sum_{i=1}^n d_i^2} \pm \sqrt{\frac{1}{n} \cdot \sum_{i=1}^n (d_{p,s} - d_i)^2} \quad (3.1)$$

The interparticle distance (i_{pd}), the distance between the edges of two silver particles, was estimated using the average density of silver distributed over the surface area of the support materials. It was calculated using Equation 3.2, where A is the specific surface area of the support material obtained via nitrogen physisorption and N is the estimated number of silver particles present, calculated using the silver loading and the surface-averaged silver particle size. A flat support surface and a hexagonal arrangement of spherical silver particles over the support surface were assumed.

$$i_{pd} \text{ (edge to edge)} = \sqrt{\frac{A}{N}} - d_{p,s} \quad (3.2)$$

Due to the morphology of the macroporous materials, the use of electron microscopy is challenging. Therefore, to validate the SEM measurements, Diffuse-Reflectance Ultraviolet/Visible (DR UV/Vis) spectroscopy was used to determine the surface-averaged silver particle size. DR UV/Vis spectra of the materials were obtained by measuring circa 20–100 mg material in the range of 800–200 nm with a 4 nm interval and a 4 nm slit size using a Varian CARY 500 scan UV/Vis-NIR or a Perkin Elmer Lambda 950S UV/Vis-NIR spectrophotometer with an integrating sphere detector. Some of the macroporous materials were diluted, by mixing 30 mg of analyte with 600 mg pristine α -alumina ($1\text{ m}^2\text{ g}^{-1}$, 100 mesh, Sigma-Aldrich). The peak position of the

surface plasmon resonance absorption (λ_{\max}) was used as a measure for the surface-averaged particle size using Equation 3.3. For this calibration curve, simulations were made using Lumerical software, for silver particles in an environment of 60% air and 40% α -alumina [48]. Macroporous α -alumina materials exhibit a relatively weak scattering peak; this contribution was neglected in the estimation of the silver particle size via DR UV/Vis.

$$\lambda_{\max} = 0.0073 \cdot d_{p,s}^2 + 0.2965 \cdot d_{p,s} + 385.34 \quad (3.3)$$

Crystal phase analysis was performed using X-ray diffraction (XRD) on a Bruker D2 Phaser diffractometer, equipped with a Co K_{α} source ($\lambda = 0.1789$ nm). The composite structures were analyzed by comparing the diffractograms with crystal structures from the PDF-4+ 2016 database.

3.2.4 Thermal stability

Thermal stability measurements were performed in a tubular oven by heating 10 to 100 mg of silver-containing material (38–150 μm) in a hydrogen or oxygen flow with a GHSV of 16000–60000 hr^{-1} . The samples were heated from room temperature to 100, 200, 300 and/or 400 $^{\circ}\text{C}$ (5 $^{\circ}\text{C min}^{-1}$ heating ramp).

3.2.5 Catalytic testing

The catalytic performance of the silver supported on α -alumina materials was investigated for the epoxidation of ethylene. In a typical catalysis experiment, 25 mg catalyst grains (38–150 μm) diluted with 125 mg SiC (Alfa Aesar, >98%, 212–245 μm) was loaded in a plug flow reactor with an internal diameter of 4 mm between two layers of quartz wool. The SiC diluent was washed with $\text{HNO}_{3,(\text{aq})}$ (65%, AnalaR NORMAPUR[®] analytical reagent; 10 mL $\text{g}_{\text{SiC}}^{-1}$) and calcined at 800 $^{\circ}\text{C}$, to remove any metal or organic contaminants. The catalysts were conditioned by heating them to 270 $^{\circ}\text{C}$ for 90 min in a flow of 20 mL min^{-1} containing 7.5% ethylene and 2.13% oxygen in helium at atmospheric pressure. Afterward, the reaction temperature was lowered to 180–200 $^{\circ}\text{C}$ and the gas flow rate per gram of silver was varied between 350 and 1600 L $\text{g}_{\text{Ag}}^{-1} \text{h}^{-1}$. The reaction products were analyzed every 15 min using online gas chromatography (Interscience) equipped with two separate channels containing a Porabond Q column and a Molsieve 5 \AA column and thermal conductivity detectors. Conversion and selectivity data were calculated from data retrieved at 180 and 200 $^{\circ}\text{C}$ when steady state was reached after 50 h on stream. For calculations on transport limitations, see Appendix B, Section I. The conversion of ethylene and selectivity towards ethylene oxide during the ethylene epoxidation reaction were calculated using Equations 3.4 and 3.5. X and S stand for the conversion (in %) and selectivity (in %) respectively, while p_A is the partial pressure of component A (in Pa). The carbon balance (Equation 3.6) was above 99% for all datapoints used.

$$X_{\text{Ethylene}} = \frac{0.5 \cdot p_{\text{CO}_2} + p_{\text{Ethylene oxide}} + p_{\text{Acetaldehyde}}}{p_{\text{Ethylene, out}} + 0.5 \cdot p_{\text{CO}_2} + p_{\text{Ethylene oxide}} + p_{\text{Acetaldehyde}}} \cdot 100\% \quad (3.4)$$

$$S_{\text{Ethylene oxide}} = \frac{p_{\text{Ethylene oxide}}}{0.5 \cdot p_{\text{CO}_2} + p_{\text{Ethylene oxide}} + p_{\text{Acetaldehyde}}} \cdot 100\% \quad (3.5)$$

$$\text{Carbon balance} = \frac{p_{\text{Ethylene, out}} + 0.5 \cdot p_{\text{CO}_2} + p_{\text{Ethylene oxide}} + p_{\text{Acetaldehyde}}}{p_{\text{Ethylene, in}}} \cdot 100\% \quad (3.6)$$

The apparent turnover frequency (TOF), in mole of ethylene converted per mole surface silver per second, was determined using Equation 3.7, where P is the pressure (101325 Pa), u is the flow velocity of ethylene (in $\text{m}^3 \text{s}^{-1}$), X is the ethylene conversion (in %), R is the gas constant ($8.314 \text{ J mol}^{-1} \text{ K}^{-1}$), T is the ambient temperature (298 K), m is the mass of silver used (in mol), $V_{\text{Ag atom}}$ the volume of a silver atom (in m^3), $A_{\text{Ag atom}}$ the surface area of a silver atom (in m^2) and $d_{p,s}$ is the surface-averaged diameter of the silver particles (in m), used to calculate the dispersity (using an Ag atom radius of $1.44 \cdot 10^{-10}$ m). The silver particles were assumed to be spherical and the silver surface atoms were assumed to be the active sites [48,157,196]. The first part of Equation 3.7 was used for determining the amount of ethylene converted (in mol s^{-1}), and the bottom of the last part was used to estimate the silver surface (in mol).

$$TOF = \frac{P \cdot u_{\text{Ethylene}} \cdot X_{\text{Ethylene}}}{R \cdot T} \cdot \frac{1}{m_{\text{Ag}} \frac{6V_{\text{Ag atom}}}{A_{\text{Ag atom}} \cdot d_{p,s}}} \quad (3.7)$$

3.3 Results and discussion

3.3.1 α -alumina materials

Different α -alumina materials, varying in porosity and specific surface area, were used as support materials. Figure 3.1 shows the nitrogen physisorption isotherms (Frame A) and scanning electron microscopy (SEM) images (Frame B–F) of the selected α -alumina materials. Frames B and C are images of two commercially available α -alumina materials without intraparticle porosity, distinguished by their specific surface area of $1 \text{ m}^2 \text{ g}^{-1}$ and $8 \text{ m}^2 \text{ g}^{-1}$, respectively. Large, nonporous particles are visible in the image of $1 \text{ m}^2 \text{ g}^{-1}$ α -alumina (Frame B). Some smaller crystallites decorate the surface, but most of the material consists of large particles exceeding several micrometers. The large particles have flat surfaces and relatively sharp edges, indicative of a high crystallinity. The $8 \text{ m}^2 \text{ g}^{-1}$ α -alumina (Frame C) is a specialty chemical. The crystallites in this α -alumina consist of interconnected grains of approximately 100 to 500 nm in size, which exhibit more rounded features.

In addition to the commercially available materials, we synthesized a series of macroporous materials with much larger specific surface areas (Figure 3.1, Frames D–F). X-ray diffraction (XRD) measurements showed that all materials had the α -alumina crystal structure (see Appendix B, Figure B.1). According to nitrogen physisorption measurements, all materials had specific surface areas of circa $30 \text{ m}^2 \text{ g}^{-1}$, which is significantly higher than the commercial α -alumina materials. These high surface areas are ascribed to the intraparticle porosity. For all macroporous materials, regular features that are arranged in a hexagonal lattice are observed. The morphology is a highly ordered pore structure, consisting of cages with interconnecting windows to the nearby cages. Using SEM, the cage and window sizes were measured. The cage and the window sizes vary per material, the cage size ranges from 160 nm to 205 and the window size ranges from 55 to 115 nm.

Hydroxyl groups on the surface of the alumina (acid sites) facilitate the unwanted combustion of ethylene oxide to carbon dioxide and water and therefore influence the selectivity of the catalysts [13–16]. The acidity of the α -alumina materials was determined using temperature programmed

desorption (TPD) of ammonia. The desorption curves and the data fitting used to calculate the surface density of acid sites are given in Appendix B, Figure B.2, and an overview of the specific surface areas and the surface density of acid sites of the materials are given in Table 3.1. The number of acid sites per surface area was very similar for all alumina supports discussed and in line with values reported in literature [161,197], except for the $1 \text{ m}^2 \text{ g}^{-1}$ α -alumina. However, it should be noted that in this case the error in the determination of the acid density might be much larger than for the other alumina materials, as the main error is in the determination of the specific surface area.

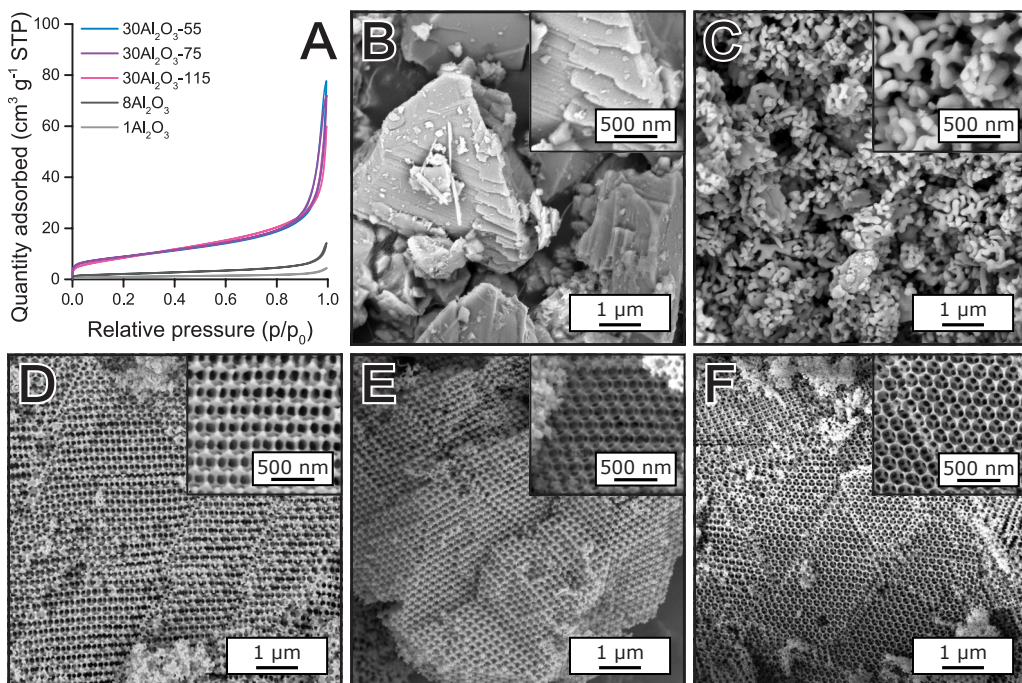


Figure 3.1 Nitrogen physisorption isotherms (A) and the corresponding scanning electron microscopy images (B–F) of the various α -alumina materials. $1 \text{ m}^2 \text{ g}^{-1}$ α -alumina (B), $8 \text{ m}^2 \text{ g}^{-1}$ α -alumina (C) and ordered macroporous α -alumina with specific surface areas of circa $30 \text{ m}^2 \text{ g}^{-1}$ (D–F) with number-averaged cage and window sizes of respectively 205 and 115 nm (D), 165 and 75 nm (E) and 160 and 55 nm (F).

Table 3.1 Overview of the surface density of acid sites on α -alumina materials, labeled in the form $\text{SSAAl}_2\text{O}_3\text{-WS}$, with SSA the specific surface area of the α -alumina used as support material, and WS the number-averaged window size of the α -alumina, if applicable.

Material	Specific surface area ($\text{m}^2 \text{ g}^{-1}$)	Acid sites ($\mu\text{mol g}^{-1}$)	Acid sites ^a (nm^{-2})
$1\text{Al}_2\text{O}_3$	1	25.6	15
$8\text{Al}_2\text{O}_3$	8	55.7	4.2
$30\text{Al}_2\text{O}_3\text{-115}$	33	194	3.6
$30\text{Al}_2\text{O}_3\text{-55}$	31	165	3.2

^a Density of acid sites calculated using the specific surface area of the materials.

3.3.2 Silver deposition

The size of the silver particles deposited on the α -alumina materials was tuned by varying the gas atmosphere in the heat treatment step [48]. In this way, despite the use of different support materials and metal weight loadings, sets of supported silver particles with the same initial silver particle sizes were prepared, and all materials were exposed to the same maximum temperature of 215 °C during preparation. XRD measurements showed that irrespective of the atmosphere used during the heat treatments, for all materials the diffraction pattern of metallic silver was observed (see Appendix B, Figure B.3). The presence of metallic silver instead of silver oxides can be explained by the low decomposition temperatures of circa 200 °C for silver (I) oxide and below 200 °C for silver (I,III) oxide [198]. It is known that under these conditions some small particles of silver oxide or surface oxides still may be formed, and that these can be stable up to higher temperatures, however, the bulk of the particles is metallic [51,199–201].

Silver particle size analysis was performed both by using SEM and Diffuse-Reflectance Ultraviolet/Visible (DR UV/Vis) spectroscopy. Figure 3.2 shows an SEM image and the DR UV/Vis spectrum of two materials, used for the particle size analysis. An overview of all materials discussed in this chapter is given in Table 3.2. In the SEM images in Figure 3.2, the silver is visible as bright white, round particles. They are deposited on 30 m² g⁻¹ α -alumina with cage and window size of respectively 205 and 115 nm (Frame A) and on non-porous 1 m² g⁻¹ α -alumina (Frame B). The surface-averaged size of these silver particles are 45 nm \pm 22 nm, and 44 nm \pm 22 nm, respectively. The insets in Frames A and B show the particle size distributions. The DR UV/Vis spectra of the materials are given in Frame C. As the supported silver particles are large enough to exhibit surface plasmon resonance, the position and intensity of the silver surface plasmon resonance peak in the DR UV/Vis spectra can be used to derive a surface-averaged silver particle size [48,202–204]. These surface-averaged silver particle sizes, calculated from the maximum peak positions using Equation 3.3 (see Section 3.2.3), are 45 nm for the silver on 30 m² g⁻¹ α -alumina, and 52 nm for the silver on 1 m² g⁻¹ α -alumina, and are in agreement with the surface-averaged silver sizes obtained from the SEM measurements.

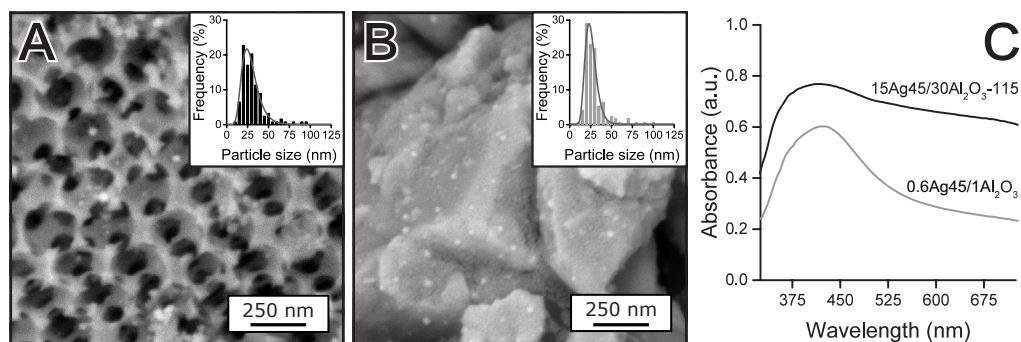


Figure 3.2 SEM images of 15 wt% silver particles supported on ordered macroporous α -alumina (15Ag45/30Al₂O₃-115, A) and non-porous α -alumina with a surface area of 1 m² g⁻¹ (0.6Ag45/1Al₂O₃, B) and the corresponding UV/Vis spectra in black and gray, respectively (C).

Table 3.2 Overview of silver on α -alumina materials, labeled in the form $wt\%AgD/SSAAl_2O_3$ -WS, with $wt\%$ being the theoretical silver weight loading, D the initial surface-averaged silver particle diameter, SSA the specific surface area of the α -alumina used as support material, and WS the number-averaged window size of the α -alumina, if applicable. For all prepared materials, the decomposition of the silver precursor during preparation was performed at 215 °C, at the gas composition listed in the second column.

Material	Gas composition during preparation	Silver		α -alumina support		
		Weight loading (wt%)	Particle size ^a (\varnothing , nm)	Surface area ($m^2 g^{-1}$)	Cage size (nm)	Window size (nm)
0.6Ag45/1Al ₂ O ₃	N ₂	0.6	44 ± 22	1	-	-
15Ag60/1Al ₂ O ₃	50% H ₂ in N ₂	15	63 ± 14	1	-	-
15Ag75/1Al ₂ O ₃	50% H ₂ in N ₂	15	74 ± 42	1	-	-
4.5Ag45/8Al ₂ O ₃	N ₂	4.5	35 ± 17	8	-	-
15Ag40/8Al ₂ O ₃	N ₂	15	41 ± 8	8	-	-
15Ag60/8Al ₂ O ₃	O ₂	15	56 ± 29	8	-	-
15Ag75/8Al ₂ O ₃	O ₂	15	75 ± 31	8	-	-
15Ag45/30Al ₂ O ₃ -115	N ₂	15	45 ± 22	33	205	115
15Ag60/30Al ₂ O ₃ -115	O ₂	15	61 ± 26	33	205	115
15Ag60/30Al ₂ O ₃ -80	O ₂	15	65 ± 23	30	190	80
15Ag60/30Al ₂ O ₃ -75	O ₂	15	59 ± 27	32	165	75
15Ag70/30Al ₂ O ₃ -55	O ₂	15	70 ± 40	31	160	55

^a Surface-averaged particle sizes and the width of the size distributions, obtained via SEM analysis. Small variations in the experimental preparation parameters, such as batch size, batch of reactants and the use of different ovens led to some variation in the silver particle sizes.

3.3.3 Silver thermal stability

Catalyst deactivation is typically slow, as significant deactivation may take months to years [100,205,206]. Investigating the deactivation process under industrially relevant conditions is therefore time consuming. To accelerate the deactivation, materials can be exposed to harsh conditions. In this study, the particle growth was accelerated by heating the silver-containing materials to relatively high temperatures. The stability of the silver was then investigated by measuring the particle size of the supported silver particles before and after subjecting the materials to these heat treatments.

Reductive versus oxidative atmosphere

First of all, the influence of the gas atmosphere during the heat treatment on the growth of the silver particles was investigated. The supported silver particles were subjected to heat treatments in an oxidative or a reductive atmosphere, as these represent conditions present during oxidation or reduction reactions. Heat treatments in an inert atmosphere were not performed, as during catalyst preparation, the size of the silver particles obtained in an inert atmosphere was in-between those of a reductive and an oxidative atmosphere. Figure 3.3 shows the silver particle size distributions of 15Ag40/8Al₂O₃ before and after an additional heat treatment at 200 °C or 400 °C,

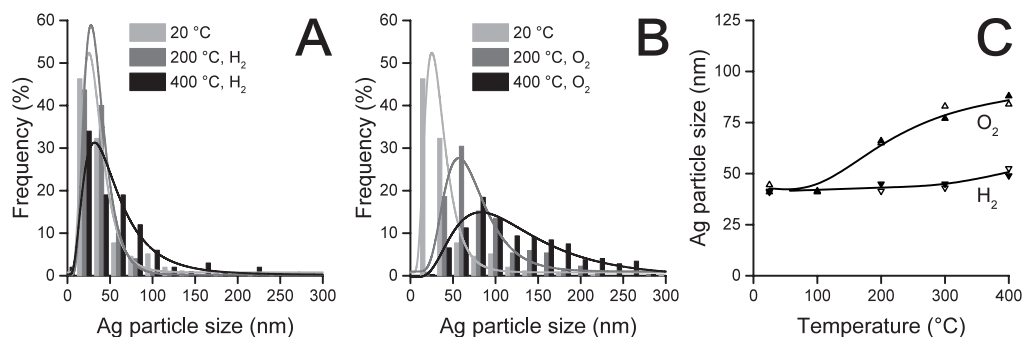


Figure 3.3 Silver particle size distributions of 15Ag40/8Al₂O₃ before and after additional heat treatments at elevated temperatures in hydrogen (A) or oxygen (B) and the surface-averaged silver particle size as a function of temperature (C). The surface-averaged particle sizes were determined using SEM (closed symbols) and DR UV/Vis (open symbols).

3

under a reductive atmosphere (Frame A) or an oxidative atmosphere (Frame B). Frame C gives an overview of the surface-averaged silver particle sizes after each heat treatment.

Upon heating the supported silver particles in hydrogen, almost no growth was observed for temperatures up to 400 °C (Frames A and C, red line). Contrarily, when heated in an oxygen atmosphere (Frames B and C, blue line), the size of the particles increased significantly. This shows that oxidized metal species are necessary for the mobility of the metal, as was reported in literature before [53,100,102,106,207,208]. In a study on the stability of gold nanoparticles, it was found that an oxidizing gas atmosphere was required to create mobile species [53]. Also for silver, the formation of mobile AgO_x clusters occurred in the presence of oxygen, and cationic species were stabilized by surface and/or gas-phase species under oxidizing conditions [209,210]. This is a strong indication that particle growth takes place via the Ostwald ripening mechanism, and that the mobile species consist of complexed silver cations [98]. The nature of these cationic species is unknown. Density functional theory (DFT) calculations showed that on copper particles for the methanol synthesis and water gas shift reaction, CuCO and Cu₂HCOO are the main transport species, but literature on the nature of silver cations is scarce [211]. Since no significant particle growth was observed in the absence of oxygen, and as for the epoxidation of ethylene the presence of oxygen is relevant, further heat treatments for exploring the thermal stability of the silver particles were performed under an oxygen atmosphere.

Interparticle distance silver particles

Next, the influence of support properties on the thermal stability of the silver was investigated. An important parameter is the surface area of the support, which affects also the distance between the supported silver particles for a given silver weight loading and particle size. Supported silver particles with the same initial silver particle size and weight loading were prepared on α -alumina with specific surface areas of 1, 8 or 30 m² g⁻¹. As a result, the estimated average interparticle distance (edge to edge) varied from 20 to 170 to 390 nm for the 1, 8 and 30 m² g⁻¹ α -alumina materials, respectively. In Figure 3.4, Frame A, the surface-averaged silver particle sizes of these

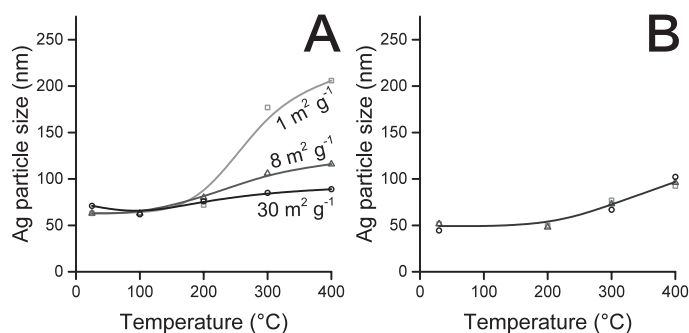


Figure 3.4 Surface-averaged particle sizes (obtained using DR UV/Vis spectroscopy) of silver supported on α -alumina with specific surface areas of 1 $\text{m}^2 \text{g}^{-1}$, 8 $\text{m}^2 \text{g}^{-1}$ or 30 $\text{m}^2 \text{g}^{-1}$, after heat treatment in an oxygen atmosphere. In (A) the silver weight loading was constant (15 wt%) while the estimated average initial interparticle distance varied from 20 nm (15Ag60/1Al₂O₃, \square), via 170 nm (15Ag60/8Al₂O₃, Δ) to 390 nm (15Ag60/30Al₂O₃-80, \circ). In (B) the weight loading of the silver was adjusted from 0.6 wt% (0.6Ag45/1Al₂O₃, \square), via 4.5 wt% (4.5Ag45/8Al₂O₃, Δ) to 15 wt% (15Ag45/30Al₂O₃-115, \circ), to obtain the same estimated average initial interparticle distance of 120 nm for all three catalysts.

catalysts are given as a function of the temperature of the thermal treatment. Up to 200 °C, the surface-averaged silver particle size was similar to the initial silver particle size of 60 nm. This was expected, as they have already been heated to 215 °C during material preparation. Large differences in particle growth are observed at higher temperatures. When the silver particles were supported on α -alumina with a specific surface area of 1 $\text{m}^2 \text{g}^{-1}$, the particle size increased from 60 to larger than 200 nm, while particle growth was modest for the silver particles supported on the 8 $\text{m}^2 \text{g}^{-1}$ and almost absent up to 400 °C for the particles on 30 $\text{m}^2 \text{g}^{-1}$ α -alumina material.

It is known that interparticle distances can have a large influence on particle stability [110,134]. Based on the previous results, it is not clear whether the differences in silver particle stability were due to support properties such as specific surface area, morphology and/or the chemical nature of the surface, or due to the interparticle distance. Hence, the thermal stability of silver on these three support materials was again evaluated, but now with a constant initial average interparticle distance. For the catalysts shown in Figure 3.4, Frame B, the silver weight loading was adjusted according to the specific surface area of the α -alumina. As the materials had the same initial surface-averaged particle size (45 nm) and silver surface density (30 atoms_{Ag} nm⁻²), they also had a similar average interparticle distance of 120 nm. In this case, the thermal stability of the silver on the catalysts with the same interparticle distance was very similar. This shows that the interparticle distance is a crucial parameter for the stability of supported silver particles.

Interparticle distance always plays an important role in the growth via particle diffusion and coalescence. However, for the Ostwald ripening mechanism, interparticle distance only has an important influence when the diffusion of the mobile metal-containing species is a rate limiting step for particle growth, while it becomes irrelevant if the formation of these mobile species, or their annihilation by attachment to another metal particle, is rate limiting [109,110]. If growth occurs mainly via particle diffusion and coalescence, it can be slowed down by restricting the

movement of complete particles [96,134]. In Figure 3.4, Frame B, the size of the silver particles (45 nm) was relatively small compared to the size of the windows (105 nm) interconnecting the cages in the $30 \text{ m}^2 \text{ g}^{-1}$ α -alumina support. It is expected that these small particles could freely move through the cages of the support material. Hence, α -alumina with a smaller window size and silver particles with a larger initial size were used to restrict the movement of complete particles, and thus to investigate which particle growth mechanism was dominant.

Support pore structure and window size

In Figure 3.5, silver particle sizes on three different macroporous α -alumina support materials with varying cage and window sizes (see Figure 3.1, Frames D–F) are shown. The specific surface area of these macroporous α -alumina materials was the same ($30 \text{ m}^2 \text{ g}^{-1}$), as were the silver weight loading (15 wt%) and initial silver particle size (60 nm). Therefore, also the interparticle distance for these three materials was similar. The only difference was the size of the cages and windows of the α -alumina support, with the window size ranging from 115 nm to 55 nm. Frames A and B show the particle size distributions after preparation (Frame A) and after an additional heat treatment at $400 \text{ }^\circ\text{C}$ (Frame B). Frame C shows the surface-averaged silver particle sizes versus the window size of the support, before and after the additional heat treatment.

For the silver particles supported on the macroporous α -alumina with window sizes of 75 or 115 nm, the surface-averaged sizes of the initial silver particles are smaller than the window sizes of the support, whereas for the α -alumina with window size of 55 nm, the initial surface-averaged particle size is larger than the window size. The surface-averaged silver particle size had increased to circa 115 nm for all three materials after the heat treatment at $400 \text{ }^\circ\text{C}$. Therefore, the growth of the silver particles was not restricted by window sizes smaller than the surface-averaged particle size, as would have been expected if particle diffusion and coalescence was the major mechanism behind particle growth. Although Ostwald ripening can be described and modeled quite accurately, this is unfortunately not the case for particle diffusion and coalescence, as

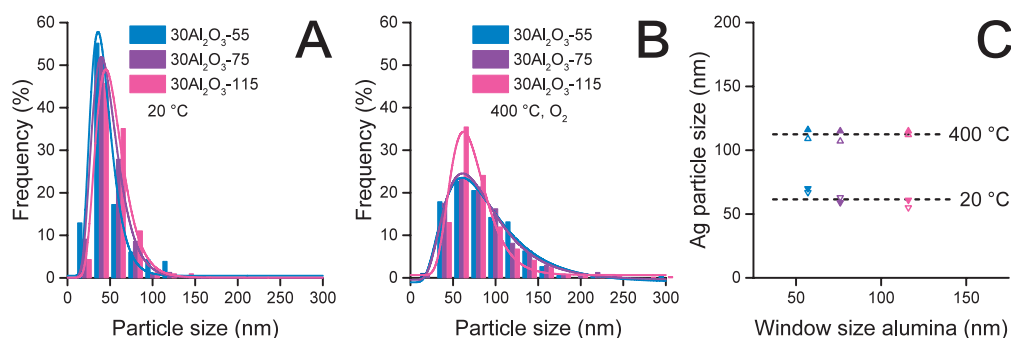


Figure 3.5 Silver particle size distributions of 15Ag70/30Al₂O₃-55 (blue), 15Ag60/30Al₂O₃-75 (purple), 15Ag60/30Al₂O₃-115 (pink) before (A) and after the additional heat treatments at $400 \text{ }^\circ\text{C}$ in an oxygen atmosphere (B) and the surface-averaged particle sizes before (\blacktriangledown) and after heat treatment (\blacktriangle) as a function of the window size of the support (C). The surface-averaged particle sizes were determined using SEM (closed symbols) and DR UV/Vis spectroscopy (open symbols).

essential parameters for modeling particle diffusion are unknown [137]. The unrestricted growth while having different window sizes, combined with the results from the heat treatments where the atmosphere was varied, strongly indicate that Ostwald ripening is the major mechanism behind the particle growth of silver particles, with diffusion of metal-containing species being the rate determining step for growth.

3.3.4 Ethylene epoxidation

The supported silver catalysts (15 wt% Ag/ α -alumina) were used in the epoxidation of ethylene. The activities of these catalysts, with apparent turnover frequencies (TOFs) in the range of 0.03–0.25 mol_{ethylene} mol_{Ag,surf}⁻¹ s⁻¹ at 180–200 °C, were in line with activities of similar ethylene epoxidation catalysts described in literature [157,196,199,212–214]. In Figure 3.6 the selectivity towards ethylene oxide versus the conversion of ethylene for silver particles supported on α -alumina with varying surface area is given. The surface-averaged size of the silver particles ranged from 60 to 75 nm. Particle size effects were not expected in this size range [48]. All catalysts showed a decrease in selectivity for higher conversion levels, as is also described and explained in previous studies [14,215–217]. The overall selectivity is highest for silver supported on the lowest surface area α -alumina (1 m² g⁻¹), with a selectivity between 30 and 60%, up to a conversion of 4%. These obtained selectivities are in accordance with literature on unpromoted silver catalysts, where selectivities between 30 and 40% are reported [50,189,218–220]. Upon increasing the surface area of the α -alumina to 8 or 30 m² g⁻¹, the selectivities of the catalysts slightly decreased, as a result of the larger gravimetric density of acid sites present on the support materials with higher specific surface areas (see Table 3.1). This is in agreement with theory, as the complete combustion of the product, ethylene oxide, is facilitated by hydroxyl groups on the surface of the support material, which decreases the overall selectivity [13–16,157].

Particle growth during accelerated aging is not the same as particle growth during the actual reaction as a result of, among others, different concentrations of oxidizing and reducing and potentially complexing species, and effective charges at the metal catalyst surface [135,221–223].

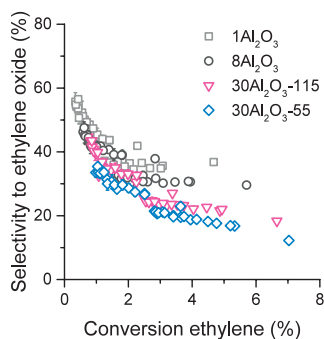


Figure 3.6 Selectivity to ethylene oxide versus the ethylene conversion for a selection of catalysts (25 mg catalyst used, 15 wt% Ag): 15Ag75/1Al₂O₃ (□), 15Ag75/8Al₂O₃ (○), 15Ag70/30Al₂O₃-55 (◇), 15Ag60/30Al₂O₃-115 (▽). Different conversions were obtained over a range of 350–1600 L g_{Ag}⁻¹ h⁻¹ (7.5% ethylene and 2.13% oxygen in helium) at 180 or 200 °C. See Appendix B, Figure B.4 for more details.

In our case, one large difference between the heat treatments and the catalytic reactions was the atmosphere. An oxidizing atmosphere was used during the heat treatments, whereas the atmosphere during catalysis contained both oxygen and reducing species, such as ethylene. Even though the stability of the silver particles under these conditions was not evaluated in depth, some conclusions can be drawn from the differences in the surface-averaged silver particle size of the catalysts before and after 120 h on stream, shown in Table 3.3. For the particle size distributions of these catalysts before and after catalysis, see Appendix B, Figure B.5.

When considering the differences between particle sizes before and after catalysis, there is only one catalyst that really stands out, which is the catalyst containing silver particles supported on $1 \text{ m}^2 \text{ g}^{-1}$ α -alumina, for which the surface-averaged silver particle size of the used catalyst was twice as large as the initial surface-averaged size. For the catalyst on $8 \text{ m}^2 \text{ g}^{-1}$ α -alumina there is a slight indication of some silver particle growth, while the silver catalysts supported on higher surface area alumina seemed fully stable. Looking in detail at the silver catalyst supported on $1 \text{ m}^2 \text{ g}^{-1}$ α -alumina, the particle growth occurs during the 90 min conditioning step at $270 \text{ }^\circ\text{C}$, as after that step no further deactivation is observed upon comparing the activity of the catalyst after the conditioning step and after 100 h on stream (see Appendix B, Figure B.6). To further investigate the kinetics of particle growth on $1 \text{ m}^2 \text{ g}^{-1}$ α -alumina during catalysis, and its influence on the activity, isothermal runs at $230 \text{ }^\circ\text{C}$ or $250 \text{ }^\circ\text{C}$ without a conditioning step were performed (see Appendix B, Figure B.7). Also at these temperatures, the particle growth was severe (from 74 nm to circa 160 nm in both cases, see Appendix B, Figure B.8) and fast, taking place within the first 10 hours of the run and hence overlapping with the activation period of the catalyst. This is in line with the fast observed growth during the heat treatments, when silver particles supported on $1 \text{ m}^2 \text{ g}^{-1}$ α -alumina with an initial size of 63 nm heated to $300 \text{ }^\circ\text{C}$ grew to about the same size (177 nm , $15\text{Ag}60/1\text{Al}_2\text{O}_3$, Figure 3.4, Frame A, heating from $200 \text{ }^\circ\text{C}$ to $300 \text{ }^\circ\text{C}$ took 20 min).

For the other catalysts, (almost) no growth of the silver particles was observed. First of all, the limited silver particle growth observed in $15\text{Ag}75/8\text{Al}_2\text{O}_3$ and the lack of particle growth in $15\text{Ag}60/30\text{Al}_2\text{O}_3-115$ and $15\text{Ag}70/30\text{Al}_2\text{O}_3-55$ confirms that the deactivation is indeed a slow process. Additionally, the particle growth that was observed after catalysis upholds the trends in particle growth observed upon the accelerated aging tests using heat treatments. The catalyst

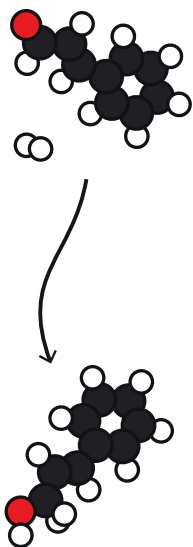
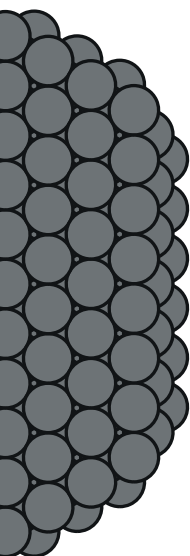
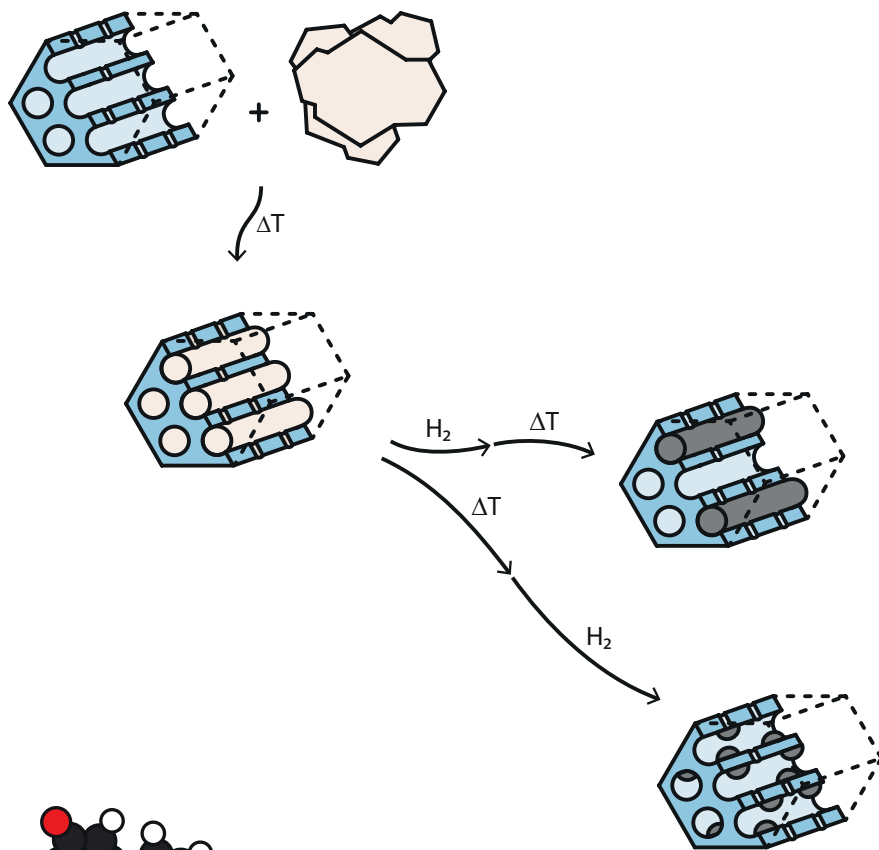
Table 3.3 Overview of the surface-averaged particle size obtained using SEM of supported silver of catalysts used in the epoxidation of ethylene after 120 h on stream at $180\text{-}200 \text{ }^\circ\text{C}$ (90 min at $270 \text{ }^\circ\text{C}$) in a flow of 350 and $1600 \text{ L g}_{\text{Ag}}^{-1} \text{ h}^{-1}$ containing 7.5% ethylene and 2.13% oxygen in helium at atmospheric pressure.

Material	Silver particle size before catalysis (\varnothing , nm)	Silver particle size after catalysis (\varnothing , nm)
$15\text{Ag}75/1\text{Al}_2\text{O}_3$	74	160
$15\text{Ag}75/8\text{Al}_2\text{O}_3$	75	80
$15\text{Ag}60/30\text{Al}_2\text{O}_3-115$	61	62
$15\text{Ag}70/30\text{Al}_2\text{O}_3-55$	70	72

stability is enhanced significantly by making use of high surface area support material at limited decrease in selectivity. This shows the promise of using α -alumina with a high specific surface area as support material in the epoxidation of ethylene.

3.4 Conclusions

The thermal stability of silver particles supported on α -alumina depends on the gas atmosphere. In hydrogen, almost no increase in the surface-averaged silver particle size was observed at temperatures up to 400 °C, with particle growth being pronounced in the presence of oxygen. The interparticle distance was an important parameter for growth, with a higher silver stability on α -alumina materials with higher specific surface areas, for a given silver weight loading and initial particle size. Restricting the movement of whole silver particles, by adjusting the support morphology, did not slow down particle growth. Based on these observations, Ostwald ripening is presumed to be the dominant particle growth mechanism, in which cationic silver complexes are the mobile species. Given that the interparticle distance is a key factor, the diffusion of these cation silver species is considered a rate determining step for particle growth. The silver particles supported on the different α -alumina materials were investigated for the epoxidation of ethylene. On the one hand, a higher surface area of the macroporous α -alumina materials led to a limited decrease in selectivity towards ethylene oxide. On the other hand, using a high surface area support provided larger interparticle distances, and hence is an excellent strategy to prevent particle growth. Support materials with high specific surface area are therefore interesting candidates for more stable catalysts in the epoxidation of ethylene.



Chapter 4

Supported silver catalysts prepared via melt infiltration

Heterogeneous supported catalysts are often synthesized by impregnation or precipitation methods. Recently, melt infiltration has emerged as an alternative method that allows high metal loadings and eliminates the need for a solvent, but challenges arise regarding control over the particle size and distribution. In this work, melt infiltration for the synthesis of supported silver catalysts is explored. The narrow pore size distribution of the chosen ordered mesoporous silica support, SBA-15, allowed in depth *in situ* and *ex situ* characterization of the infiltration of the precursor, molten silver nitrate, into the support and its subsequent decomposition to form metallic silver nanowires or nanoparticles. The heat treatment parameters during decomposition played a key role in determining whether nanowires or nanoparticles were formed. The supported silver catalysts containing high silver weight loadings were investigated in the selective hydrogenation of cinnamaldehyde, where the silver nanowires showed superior activity and selectivity over the nanoparticles. Hence, melt infiltration shows a great promise for the synthesis of supported silver catalysts containing high silver weight loadings, which are applicable in, e.g., selective oxidation or hydrogenation reactions.

4.1 Introduction

In industry, mostly impregnation and precipitation are used for the synthesis of heterogeneous catalysts [48,54–56]. For pore volume impregnation, on the one hand, the maximum weight loading is constrained by the limited solubility of precursors, and moreover, the inevitable drying step may lead to large intra- and interparticle heterogeneities in metal distribution [57,60,61]. Precipitation, on the other hand, allows high loadings but is accompanied by the production of large amounts of waste water [54]. For the synthesis of nanostructured materials for applications such as catalysis and batteries, melt infiltration has been proposed as an alternative method [86]. Melt infiltration can be used for the synthesis of materials with a high weight loading as it makes use of capillary forces to fill porous materials with a liquid precursor spontaneously.

There are restrictions to which precursors can be used for melt infiltration. For example, the precursor should not react with the support material during the infiltration process, and only precursors that have a relatively low melting temperature, at least below their decomposition temperature, can be used. Among inorganic salts, metal nitrates are particularly interesting because of their wide availability and easy decomposition into metal oxides. In literature, mainly metal nitrate hydrates have been reported, for which the low melting temperature results from the dissolution of the salt in its own crystal water [58,86,224]. For several catalysts synthesized via melt infiltration using metal nitrates, the decomposition pathways are well understood, and catalyst morphology and effectiveness were reported [93,224–226]. To the best of our knowledge, this is not the case for silver nitrate, whereas the low melting temperature of silver nitrate (212 °C) in combination with its high decomposition temperature (440 °C) makes this non-hydrated metal nitrate very interesting for the melt infiltrated synthesis of high weight loading silver catalysts. Moreover, the work of Worboys *et al.* already shows the promise of this synthesis method, as it was reported that the pores of SBA-15 can be infiltrated with silver nitrate [227].

In this chapter, the use of melt infiltration for the synthesis of highly loaded silver catalysts supported on silica is described. SBA-15 was used as model support, as its narrow pore size distribution provides the opportunity to follow the infiltration process with silver nitrate using differential scanning calorimetry. After the infiltration process is complete, the decomposition of the silver nitrate into metallic silver was followed both *in situ* and *ex situ* using X-ray diffraction and electron microscopy, showing how the morphology of the final catalyst is influenced by the decomposition parameters. Finally, we show the application of these catalysts in the selective hydrogenation of cinnamaldehyde, where the performance is coupled to the structural properties of the catalysts.

4.2 Experimental methods

4.2.1 Synthesis of the support

SBA-15 was prepared following the procedure of Lee *et al.* [228]. First, 23.4 g Pluronic P123 ($\text{EO}_{20}\text{PO}_{70}\text{EO}_{20}$, average Mw = 5800, Aldrich) was dissolved in 606.8 g deionized water and 146.4 g hydrochloric acid (HCl, 37 wt%, fuming, Merck, analysis grade) in a 1 L polypropylene bottle (cylindrical, 19.7 x 10.5 cm). After the mixture was vigorously stirred for at least 3 h in

an oil bath at 55 °C, the stirring rate was set to 600 rpm (PFTE stirring bar, 50 x 7 mm) and 50 g tetraethyl orthosilicate (TEOS, >99%, Aldrich) was added at once. After 2 min, the stirring bar was removed and the lid of the bottle was closed tightly. The mixture was first kept for 24 h at 55 °C, then for 24 h at 90 °C. Next, the material was filtrated and washed with deionized water using a Büchner funnel until the pH of the filtrate was around 5–6 (and hence no HCl was left in the solution). The filtrate was dried at 60 °C for 2–3 days and afterward crushed into a fine powder and calcined at 550 °C for 6 h (1 °C min⁻¹ heating ramp) in static air.

4.2.2 Synthesis of the catalysts

Silver was deposited on the SBA-15 via melt infiltration with silver nitrate and subsequent decomposition of the silver nitrate. In a typical synthesis, silver nitrate (AgNO₃ ≥ 99%, Sigma Aldrich) and SBA-15 were physically mixed in a 2:1 weight ratio inside a glovebox using a pestle and mortar for 5 min. This ratio corresponded to half of the pore volume of silica being filled with silver nitrate, resulting in a theoretical loading of 56 wt% Ag on SiO₂. The physical mixture was heated for 20 h at 250 °C under a top-down nitrogen flow (100 mL min⁻¹). The silver nitrate was decomposed by thermal treatment at 425 °C for 2 h (2 °C min⁻¹ heating ramp) in a nitrogen flow (100 mL min⁻¹) or by reduction for 2h in a 10% hydrogen in nitrogen flow (100 mL min⁻¹). This reduction either started at room temperature, whereupon the temperature was increased to 130 °C (0.1 or 1 °C min⁻¹ heating ramp) or started at 250 °C, after prior heating in a nitrogen flow. As a reference, a 15 wt% Ag/SBA-15 catalyst was prepared via impregnation and drying. SBA-15 was dried under vacuum for 2 h at 250 °C prior to impregnation with an aqueous AgNO₃ solution (1.64 M, 90% of pore volume). After impregnation, the composite was dried overnight under vacuum at room temperature. Next, the silver nitrate was decomposed by thermal treatment at 500 °C for 2 h (1 °C min⁻¹ heating ramp) in static air. After cooling down, the material was reduced for 2h at 250 °C (5 °C min⁻¹ heating ramp) in a 10% hydrogen in nitrogen flow (100 mL min⁻¹).

4.2.3 Characterization

The pore size, pore volume and surface area of the synthesized SBA-15 were analyzed using nitrogen physisorption. Isotherms were measured at -196 °C on a Micromeritics TriStar 3000 apparatus. The specific surface area of the support was calculated using the BET equation (0.05 < p/p₀ < 0.25). Differential scanning calorimetry (DSC) measurements were performed on a METTLER TOLEDO HP DSC 1 system by heating the sample in a 40 µL sealed aluminum pan to 250 °C with a heating ramp of 5 °C min⁻¹, at 2 bar, under an argon flow (10 mL min⁻¹). The SBA-15, the AgNO₃/SBA-15 composites before and after melt infiltration and the obtained Ag/SBA-15 composites were analyzed by transmission electron microscopy (TEM) using a Tecnai20FEG and Talos F200X microscope both operated at 200 kV. TEM samples were prepared by dropwise addition of a dispersion of the material in ethanol (SBA-15 and Ag/SBA-15) or hexane (AgNO₃/SBA-15) obtained by sonication to a TEM grid. To prevent decomposition of the silver nitrate by the electron beam, the TEM grid with the AgNO₃/SBA-15 composite and grid holder were cooled with liquid nitrogen to circa -180 °C. For spherical nanoparticles, the surface-averaged particle size (d_{ps}) and volume-averaged particle size (d_{pv}) and the standard

deviations in the width of the particle size distribution ($\sigma_{p,s}$ and $\sigma_{p,v}$) were calculated using Equations 4.1 and 4.2, with n the number of silver particles counted, and d_i the size of particle i .

$$d_{p,s} \pm \sigma_{p,s} = \frac{\sum_{i=1}^n d_i^3}{\sum_{i=1}^n d_i^2} \pm \sqrt{\frac{1}{n} \cdot \sum_{i=1}^n (d_{p,s} - d_i)^2} \quad (4.1)$$

$$d_{p,v} \pm \sigma_{p,v} = \frac{\sum_{i=1}^n d_i^4}{\sum_{i=1}^n d_i^3} \pm \sqrt{\frac{1}{n} \cdot \sum_{i=1}^n (d_{p,v} - d_i)^2} \quad (4.2)$$

For the silver nanowires, the surface-averaged wire diameter ($d_{w,s}$) and volume-averaged wire diameter ($d_{w,v}$) and the standard deviations in the width of the wire thickness distribution ($\sigma_{w,s}$ and $\sigma_{w,v}$) were calculated using Equation 4.3 and 4.4.

$$d_{w,s} \pm \sigma_{w,s} = \frac{\sum_{i=1}^n d_i^2}{\sum_{i=1}^n d_i} \pm \sqrt{\frac{1}{n} \cdot \sum_{i=1}^n (d_{w,s} - d_i)^2} \quad (4.3)$$

$$d_{w,v} \pm \sigma_{w,v} = \frac{\sum_{i=1}^n d_i^3}{\sum_{i=1}^n d_i^2} \pm \sqrt{\frac{1}{n} \cdot \sum_{i=1}^n (d_{w,v} - d_i)^2} \quad (4.4)$$

Crystal phase analysis was performed with X-ray diffraction (XRD), *in situ* on a Bruker D8 Phaser and *ex situ* on a Bruker D2 Phaser diffractometer, both equipped with a Co K_α source ($\lambda = 0.1789$ nm). The composite structures were analyzed by comparing the diffractograms with crystal structures from the PDF-4+ 2016 database. For the catalysts with a bimodal distribution of silver particles, TOPAS V5 software was used to deconvolute silver peaks into two silver phases and to calculate their crystallite sizes. Diffuse-Reflectance Ultraviolet/Visible (DR UV/Vis) spectra of the catalysts were obtained by measuring circa 100–200 mg material in the range of 800–200 nm with a 4 nm interval and a 4 nm slit size using a Perkin Elmer Lambda 950S UV/Vis-NIR spectrophotometer with an integrating sphere detector.

4.2.4 Catalytic testing

The catalysts (56 wt% Ag/SiO₂) were investigated for the liquid phase hydrogenation of cinnamaldehyde. The reaction was carried out at 70 °C and under 40 bar hydrogen pressure in an autoclave reactor containing 125 μ L t-cinnamaldehyde, 75 mg catalyst, 100 μ L tetradecane (internal standard), 6 mL isopropanol and 1 mL milliQ water. The reaction mixture was stirred at 900 rpm and samples were taken at regular time intervals of 1 or 2 h and analyzed using a Varian 430 GC. The conversion of cinnamaldehyde and selectivity towards cinnamyl alcohol were calculated using Equations 4.5 and 4.6. X and S stand for the conversion (in %) and selectivity (in %) respectively, while N_A stands for the moles of component A present at reaction time i (t_i).

$$X_{\text{Cinnamaldehyde},t_i} = \frac{N_{\text{Cinnamaldehyde},t_0} - N_{\text{Cinnamaldehyde},t_i}}{N_{\text{Cinnamaldehyde},t_0}} \cdot 100\% \quad (4.5)$$

$$S_{\text{Cinnamyl alcohol},t_i} = \frac{N_{\text{Cinnamyl alcohol},t_i}}{N_{\text{Hydrocinnamaldehyde},t_i} + N_{\text{Hydrocinnamyl alcohol},t_i} + N_{\text{Cinnamyl alcohol},t_i}} \cdot 100\% \quad (4.6)$$

The apparent turnover frequency (TOF), in mole of cinnamaldehyde converted per mole silver surface per hour, was determined using Equation 4.7, with t_i the reaction time (in h) m the mass of silver used (in mol), ϕ the fraction of the silver present inside the pores of the silica support (in %) and D_{Ag} the dispersion factor of silver. The dispersion factor is given in Equations 4.8 and 4.9 for

spheres and wires, respectively, with $V_{\text{Ag atom}}$ and $A_{\text{Ag atom}}$ the volume (in m^3) and surface area of a silver atom (in m^2), respectively (radius Ag atom = $1.44 \cdot 10^{-10}$ m), and d_s the surface-averaged diameter of the silver. The silver surface atoms were assumed to be the active sites. The first part of Equation 4.7 was used for determining the amount of cinnamaldehyde converted (in mol h^{-1}), and the bottom of the last part was used to estimate the silver surface (in mol).

$$TOF = \frac{N_{\text{Cinnamaldehyde},t_0} \cdot X_{\text{Cinnamaldehyde},t_i}}{t_i} \cdot \frac{1}{m_{\text{Ag}} \cdot \varphi_{\text{Ag in pores}} \cdot D_{\text{Ag}}} \quad (4.7)$$

$$D_{\text{Ag,spheres}} = \frac{6 \cdot V_{\text{Ag atom}}}{A_{\text{Ag atom}} \cdot d_{p,s}} \quad (4.8)$$

$$D_{\text{Ag,wires}} = \frac{4 \cdot V_{\text{Ag atom}}}{A_{\text{Ag atom}} \cdot d_{w,s}} \quad (4.9)$$

4.3 Results and discussion

4.3.1 Melt infiltration process

The SBA-15 particles had a specific surface area of $800 \text{ m}^2 \text{ g}^{-1}$ and a well-defined pore structure with mesopores of 6.8 nm (see Appendix C, Figure C.1). The monodisperse and ordered pore system of SBA-15 makes it possible to follow the melt infiltration process with silver nitrate by differential scanning calorimetry (DSC). With this technique, information about phase transitions of materials is obtained, as during these phase transitions, heat is released or consumed.

In Figure 4.1, DSC thermograms of $\text{AgNO}_3/\text{SBA-15}$ (Frame A) and macrocrystalline AgNO_3 (Frame B) are shown. Curve A shows the measured heat flow while heating a physical mixture of silver nitrate and SBA-15 to $250 \text{ }^\circ\text{C}$. Curves B and C show the same sample as in Curve A, but after *in situ* and *ex situ* melt infiltration, respectively. The amount of silver nitrate corresponded to 50% of the pore volume of the SBA-15. In all heating curves, including Curve D–F of macrocrystalline AgNO_3 , an endothermic peak is visible around $212 \text{ }^\circ\text{C}$. In Curve A, an additional endothermic peak is present at $200 \text{ }^\circ\text{C}$, while in Curve B and C, a second peak is observed at $148 \text{ }^\circ\text{C}$.

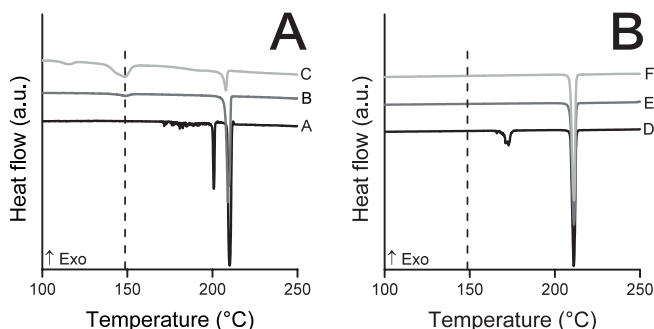


Figure 4.1 DSC thermograms of $\text{AgNO}_3/\text{SBA-15}$ composites (A) and macrocrystalline AgNO_3 (B) recorded during heating at $5 \text{ }^\circ\text{C min}^{-1}$. Curve A: physical mixture of AgNO_3 and SBA-15, kept at $250 \text{ }^\circ\text{C}$ for 4 hours; Curve B: second heating of composite shown in Curve A; Curve C: *ex situ* melt infiltrated material (20h, $250 \text{ }^\circ\text{C}$, nitrogen), Curve D, E and F: first, second and third heating of macrocrystalline AgNO_3 , respectively. Only thermograms during heating are displayed and they are offset for clarity.

All peaks in Figure 4.1 are ascribed to phase transitions of AgNO_3 . The endothermic peak at 200°C in Curve A is ascribed to a solid-solid phase transition of silver nitrate from the orthorhombic phase to the rhombohedral phase. X-ray diffraction (XRD) on the cooled down material confirms the transition to this rhombohedral phase and shows that the transition is irreversible (see Appendix C, Figure C.2). Therefore, this transition only occurred during the first heating ramp, and no peaks are visible at 200°C in Curve B and C. The solid-solid phase transition is not observed when silver nitrate was heated in the absence of silica (see Appendix C, Figure C.3) but has been reported before, upon heating a composite of silver nitrate and silica [227].

The melting of macrocrystalline silver nitrate gave an endothermic peak at 212°C (Curve D–F), which is in agreement with literature [229]. This peak is at the same position in every thermogram of macrocrystalline AgNO_3 (Curve D–F), while this peak slightly shifted to lower temperatures for the $\text{AgNO}_3/\text{SBA-15}$ composites in Curve B and C compared to Curve A. Presumably, during prior heating of materials in Curve B and C in the presence of the SBA-15, the macrocrystalline silver nitrate spread out over the external surface of the SBA-15 particles, which slightly lowered the melting temperature.

By comparing the second thermogram on the $\text{AgNO}_3/\text{SBA-15}$ composite (Curve B) with the second thermogram on macrocrystalline AgNO_3 (Curve E), it becomes evident that infiltration took place. In Curve E, only the peak corresponding to melting of macrocrystalline silver nitrate at 212°C is present, whereas in Curve B an extra peak at 148°C is visible, which corresponds to the melting of infiltrated silver nitrate. At the start of heating Curve A, the pores are empty, and therefore, only the melting of macrocrystalline silver nitrate is observed. Upon melting, part of the silver nitrate entered the pores of the SBA-15. The melting temperature of material inside nanopores is significantly lower, as a result of pore confinement [230]. Since the pores of the SBA-15 are uniform in size, the melting point depression is the same for all silver nitrate inside the pores. DSC thermograms of infiltrated material therefore show a single extra peak at lower temperature. The melting point depression of 64°C , is close to the expected maximum decrease in melting temperature of circa 70°C , calculated using the Gibbs-Thomson equation and assuming complete wetting, [230], see Appendix C, Section III. However, the low intensity of this peak and the high intensity of the peak corresponding to the melting of macrocrystalline silver nitrate indicate that most silver nitrate remained outside the pores and the *in situ* melt infiltration is not very effective.

Curve C in Figure 4.1 shows the heating of the composite after *ex situ* melt infiltration, where the mixture was heated for 20 hours at 250°C , under a nitrogen flow. The intensity of the peak of melting silver nitrate inside the pores at 148°C is significantly higher than for Curve B, while the intensity of the peak corresponding to the melting of macrocrystalline silver nitrate at 212°C is much lower. Since the surface area of a peak corresponds directly to the amount of molten silver nitrate, a quantitative analysis on the amount of silver nitrate that infiltrated the pores is possible. From the peaks at 212°C in Curve A and C, it was calculated that 93% of the silver nitrate infiltrated the pores of the SBA-15 during the *ex situ* melt infiltration. The higher efficiency of this *ex situ* melt infiltration is attributed to the improved contact between the silver nitrate and the SBA-15 as a result of the longer heating time.

Another method to analyze the outcome of the infiltration process is by transmission electron microscopy (TEM). With TEM, the pore structure and filling of the SBA-15 particles were imaged. In Figure 4.2, Frame A, a TEM image of pristine SBA-15 is shown. With the pore structure of an SBA-15 particle aligned with the electron beam, the ordered structure became visible. The inset shows the side of an SBA-15 particle, which shows the hexagonal ordering of the mesopores. Frame B shows the $\text{AgNO}_3/\text{SBA-15}$ composite (56 wt% $\text{Ag}/\text{SBA-15}$) after melt infiltration at 250 °C. Silver nitrate in an electron beam results in immediate decomposition of the silver nitrate, however, by cooling the TEM grid in liquid nitrogen, we were able to stabilize and image the silver nitrate. Here, approximately half of the pores are filled with silver nitrate and therefore, instead of bright pores, dark lines are visible within the silica structure, which confirms the successful infiltration.

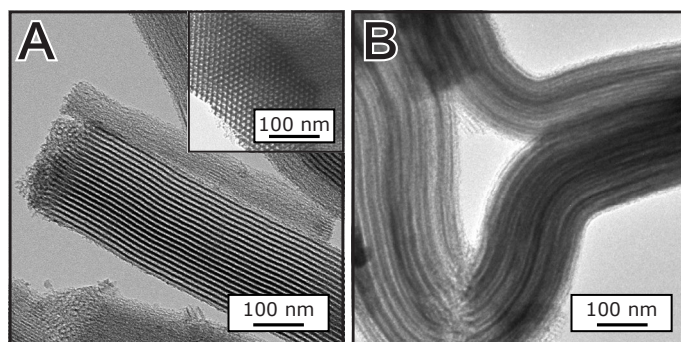


Figure 4.2 TEM images of pristine SBA-15 (A) and *ex situ* melt infiltrated $\text{AgNO}_3/\text{SBA-15}$ (20h, 250 °C, nitrogen, B).

4.3.2 Decomposition of the AgNO_3 precursor

After the distribution of the silver precursor over the support material, the precursor was decomposed to obtain metallic nanoparticles. For this, several methods are available, such as thermal decomposition (Chemical Equation 4.1), or reduction of silver nitrate (Chemical Equation 4.2). The particle size and morphology are influenced by the gas atmosphere, heating ramp and final temperature [48,231]. Using *in situ* XRD, we followed the decomposition of silver nitrate by heating the melt infiltrated $\text{AgNO}_3/\text{SBA-15}$ composite under an inert, oxidizing or reducing atmosphere up to 500 °C.



Figure 4.3 shows the diffractograms at different temperatures, where Frame A shows the thermal decomposition in a helium flow and Frame B shows its reduction in a 5% hydrogen in helium flow. In both graphs, peaks corresponding to silver nitrate in the rhombohedral structure are visible up to 100 °C, while large differences are observed at higher temperatures. In an inert atmosphere, the peaks corresponding to silver nitrate decreased in intensity when the temperature

was increased to 150 °C, and at 200 °C, crystalline phases were no longer observed. This is in line with the melting of the silver nitrate in the pores of the SBA-15, which takes place at the depressed melting temperature around 150 °C (see Figure 4.1). When the composite reached 450 °C, new peaks were observed, which increased in intensity upon further heating to 500 °C. These peaks correspond to silver, indicating the decomposition of the silver nitrate into metallic silver, as is expected for macrocrystalline silver nitrate which is reported to decompose at 450 °C [229]. More in-depth analysis on the composite showed that next to the formation of silver, also some silver silicate, $\text{Ag}_{10}\text{Si}_4\text{O}_{13}$, had formed (see Appendix C, Figure C.4). Literature on the formation of silver silicate by reaction of silver nitrate and silica has, to the best of our knowledge, not been reported before. The liquid silver nitrate presumably reacted with the silica support at high temperature to form silver silicate and nitrogen oxides. As is visible in the TEM image of this material (Figure 4.3, Frame C), the pore system of the SBA-15 was completely destroyed, indicating that this silver silicate formed at the expense of the silica pore walls.

Analogous to the composite heated in an inert atmosphere, the peaks in the diffractogram after heating at 30 to 50 °C in a reducing atmosphere correspond to the rhombohedral structure of silver nitrate. However, in this case, already at 100 °C a broad peak of metallic silver appeared. The diffractograms taken at 125 °C and higher contain only peaks of metallic silver. This shows that the silver nitrate was completely reduced at 125 °C, even before melting of the silver nitrate occurred. Furthermore, no formation of silver silicate was observed, probably because of the formation of metallic silver at a much lower temperature. Instead, silver nanowires had formed inside the pores (Frame D).

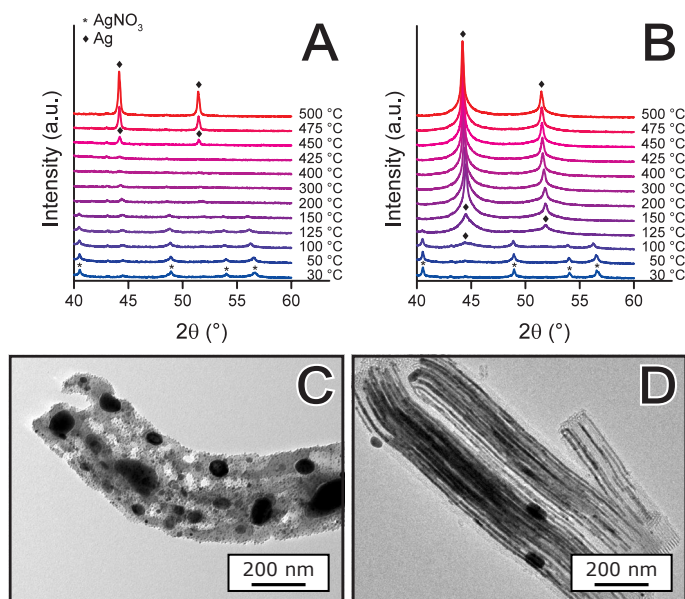


Figure 4.3 Diffraction patterns of melt infiltrated $\text{AgNO}_3/\text{SBA-15}$ treated in an inert atmosphere (helium, A) or a reducing atmosphere (5% hydrogen in helium, B) measured *in situ* and TEM images of the materials after cooling down (C and D, respectively). The diffraction patterns are offset for clarity.

Figure 4.4 shows TEM images of Ag/SBA-15 catalysts prepared by *ex situ* decomposition of the infiltrated material. In Frame A, silver nitrate was thermally decomposed by heating to 425 °C in a nitrogen flow. Just as with the material heated during the *in situ* XRD measurements, SBA-15 particles no longer contained ordered pores, due to the formation of silver silicate. In order to prevent the formation of silver silicate, the decomposition of the silver nitrate was in all other cases conducted under a reductive atmosphere, resulting in the materials shown in Figure 4.4, Frames B, C and D. Silver nanowires which filled some of the pores of the SBA-15 completely, are visible in Frame B and C, while small silver nanoparticles distributed over the pores are visible in Frame D.

The silver nanowires were obtained by starting the reduction at room temperature by applying a flow of 10% hydrogen in nitrogen, and by slowly heating the composite to 130 °C in this atmosphere. Both when a heating ramp of 0.1 °C min⁻¹ or 1 °C min⁻¹ was used, SBA-15 with silver nanowires inside the pores were obtained. Although the heating ramp was different, the silver nanowires were very similar in both catalysts, and the pores of the SBA-15 were either completely filled, or completely empty. The similarities of these samples are further supported by the similar plasmon absorption peaks in the Diffuse-Reflectance Ultraviolet/Visible (DR UV/Vis spectra, with a maximum absorption at 388 nm for both materials (see Appendix C, Figure C.5). Considering that the volume of silver nitrate is 3.8 times larger than metallic silver, it is striking

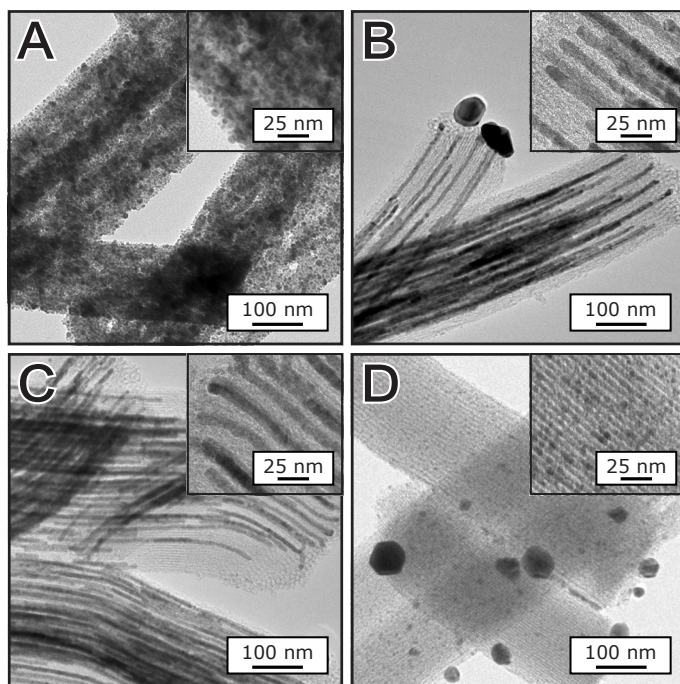


Figure 4.4 TEM images of Ag/SBA-15 composites after decomposition of the silver nitrate in nitrogen (A) and in 10% hydrogen in nitrogen (B–D). Silver nanowires inside the pores of the SBA-15 were obtained when the reduction was started at room temperature with a heating ramp of 1 °C min⁻¹ (B) or 0.1 °C min⁻¹ (C), while starting the reduction at 250 °C led to the formation of silver nanoparticles inside the pores (D).

that completely filled pores were observed. However, the formation of silver nanowires in SBA-15 has been reported before and is ascribed to the mobility of intermediate phases during the decomposition [227,231].

By altering the heat treatment parameters, the morphology of the silver was changed considerably. When the infiltrated material was first heated to 250 °C in an inert atmosphere, and the reduction was started at this temperature, the pores of the SBA-15 contained silver nanoparticles of 2.3 ± 0.7 nm (Figure 4.4, Frame D). The silver nanoparticles were uniformly distributed over the pores. The nanoparticles show a maximum plasmonic absorption at 368 nm (see Appendix C, Figure C.5). The intensity of this peak is lower than for the nanowires and the peak location is at a shorter wavelength, confirming the formation of smaller silver nanoparticles. By increasing the temperature before starting the reduction, probably more nuclei were created, just as with the “hot injection” synthesis method of colloidal particles [232]. This prevented the formation of nanowires and facilitated the formation of many small nanocrystallites.

Next to TEM, XRD was used to determine the average silver particle size, since the width and intensity of silver peaks gives information on the crystallite size of the material [169,170]. In Figure 4.5, the diffractograms of the Ag/SBA-15 composites are shown, in which all peaks correspond to metallic silver (black). The shape of these peaks indicates the presence of a bimodal size distribution, since the broad base of the peaks suggests the presence of small crystallites, whereas the sharp tips imply larger crystallites [170]. Using TOPAS V5 software, each peak in the diffractograms was deconvoluted into two separate peaks, one sharp peak for large crystallites (red) and one broad peak for smaller crystallites (green), where the sum of these two peaks, the total fit, is in good agreement with the experimental data (see Appendix C, Figure C.6). In doing so, both the average crystallite sizes and the percentages of silver in each phase were estimated [233].

In Table 4.1, an overview of the different materials with the measured particle sizes using TEM and the calculated crystallite sizes from the deconvoluted peaks and percentages of silver present in the small crystallites are given. The calculated size of the large crystallites overlaps with

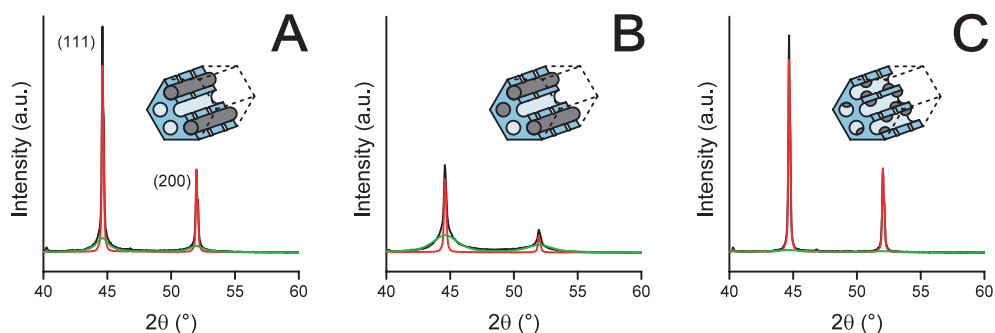


Figure 4.5 Diffractograms (black lines) of Ag/SBA-15 composites after decomposition in 10% hydrogen in nitrogen at 130 °C with a heating ramp of 1 °C min⁻¹ (A) or 0.1 °C min⁻¹ (B), or when heating in nitrogen and starting the reduction at 250 °C (C), and the deconvoluted peaks for small crystallites (green lines) and large crystallites (red lines).

the size of the large silver particles on the external surface area of the SBA-15, present in all three catalysts. The small crystallite sizes obtained from the XRD data were very similar to the measured nanowire thicknesses obtained via TEM. The small crystallite size calculated in Ag/SBA-15_N₂ however, was larger than the measured nanoparticle size on TEM images. This is expected, since in the TEM image analysis, only nanoparticles in the pores were measured, while for XRD, a volume-average of all smaller crystallites was taken, which includes some particles of 5–10 nm also present outside of the pores that shift the average to a higher value. Furthermore, silver nanoparticles below 2 nm give a very broad peak with a low intensity, barely visible in the diffractogram, and therefore, they are at least partly unaccounted for.

The amount of silver inside versus outside of the pores was estimated by assuming that the small crystallites were inside the pores of the SBA-15, while the larger crystallites were outside. These values are given in Table 4.1 and are clearly different for the three composites. When considering the two materials decomposed in hydrogen and containing silver nanowires, the heating ramp during the decomposition had a crucial influence on how much silver resided in the pores upon the decomposition of the silver nitrate. Much more silver remained in the pores when a very low heating ramp of 0.1 °C min⁻¹ was used (73%), compared to when a relatively high heating ramp of 1 °C min⁻¹ was used (39%). Likely, the gaseous decomposition products formed during the reduction pushed some of the silver nitrate out of the pores. By increasing the heating ramp, not only the amount of gas produced in a short time, but also the number of mobile species increased, leading to a higher expulsion of silver nitrate. When the reduction was started at 250 °C after heating in nitrogen (Ag/SBA-15_N₂), even less silver remained in the pores (only 19%). Here, probably complete reduction of all silver nitrate took place in a very short time, allowing the formation of silver nanoparticles, but also producing large volumes of decomposition products, pushing most of the silver nitrate out of the pores.

Even though part of the silver formed large particles outside the SBA-15 pores, for all three catalysts, more than 90% of the silver surface atoms was located on the intraporous silver nanowires and nanoparticles. These percentages were calculated using the obtained crystallite sizes and percentages of silver present inside the pores, and the high numbers are a result of the

Table 4.1 Overview of the particle and crystallite sizes of the Ag/SBA-15 composites, labeled in the form Ag/SBA-15_X, with X being the used heating ramp when the reduction was started at room temperature up to 130 °C, or X being the atmosphere used during heating when the reduction was started at 250 °C.

Sample	Heating ramp (°C min ⁻¹)	H ₂ during heating (%)	Ag nanowire / nanoparticle diameter ^a (nm)	Small / large crystallite sizes ^b (nm)	Small crystallites ^b (%)	Ag surface atoms inside pores ^c (%)
Ag/SBA-15_1	1	10	10.0 ± 1.4	9.9 / 252	39	92
Ag/SBA-15_0.1	0.1	10	9.1 ± 0.9	9.7 / 150	73	97
Ag/SBA-15_N ₂	2	0	2.3 ± 0.7	5.1 / 227	19	91

^a Volume-averaged sizes determined by TEM.

^b Calculated from deconvoluted XRD peaks using TOPAS V5 software.

^c Based on the volume-averaged crystallite sizes and fractions calculated using TOPAS V5 software.

high surface area to volume ratio of the silver nanowires and nanoparticles in comparison to the large silver particles outside of the pores. Therefore, we show the synthesis of supported silver catalysts, in which, by carefully tuning the decomposition parameters, we are able to tailor the shape of the silver and the amount of silver inside the pores of the SBA-15.

4.3.3 Catalysis

The supported silver catalysts (56 wt% Ag/SBA-15) were investigated for the hydrogenation of cinnamaldehyde. The reaction scheme of this reaction is given in Figure 4.6. Both the C=C and the C=O bond of the α,β -unsaturated aldehyde can be hydrogenated, to form hydrocinnamaldehyde and cinnamyl alcohol, respectively. Cinnamyl alcohol (CALC) is used in the pharmaceutical, flavor and perfume industry, and is therefore the preferred product [32,34]. However, the hydrogenation of the C=C bond is thermodynamically favored [33,234], showing the need for a selective catalyst. Furthermore, hydrogenation of both the C=C and the C=O bonds, yielding hydrocinnamyl alcohol, should be avoided. Although limited in activity, silver has proven to be more selective towards cinnamyl alcohol than gold, palladium, platinum and ruthenium catalysts [34].

In Figure 4.7, the conversion of cinnamaldehyde over three different Ag/SBA-15 catalysts, and the formation of products versus the reaction time is shown. The decreasing amount of cinnamaldehyde (\circ) shows that all three catalysts were active. At low conversions, mainly cinnamyl alcohol (\square) and hydrocinnamaldehyde (\triangle) formed, whereas hydrocinnamyl alcohol (\diamond) started to form only after high conversion levels ($> 90\%$) were reached. Control experiments confirmed that without silver and upon catalyst removal, no (more) cinnamaldehyde was converted (see Appendix C, Figure C.7). As a reference, the reaction was run with a catalyst containing 15 wt% Ag/SBA-15 prepared via impregnation and drying (see Appendix C, Figure C.8).

The three catalysts clearly showed different activities and selectivities. Full conversion of cinnamaldehyde within 24 or even 7 hours was reached for both catalysts containing silver nanowires (Frame A and B), but not for the catalyst with the silver nanoparticles (Frame C). This is partly explained by the presence of large silver crystallites in the latter, which do not contribute significantly to the catalysis. To better compare the activity of the catalysts, the apparent turnover frequencies (TOF) for all three catalysts and the reference catalyst prepared via impregnation and drying are listed in Table 4.2. These TOF values were calculated using the estimated values for the silver present inside the pores and using initial surface-averaged particle diameters from

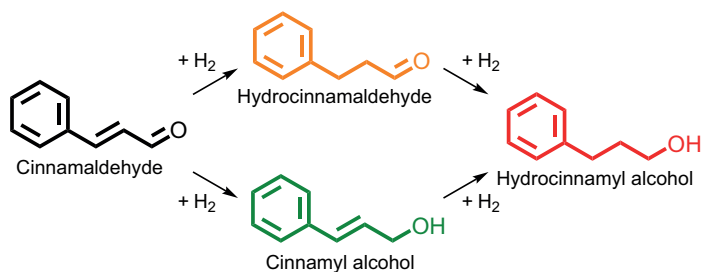


Figure 4.6 Schematic representation of the hydrogenation of cinnamaldehyde.

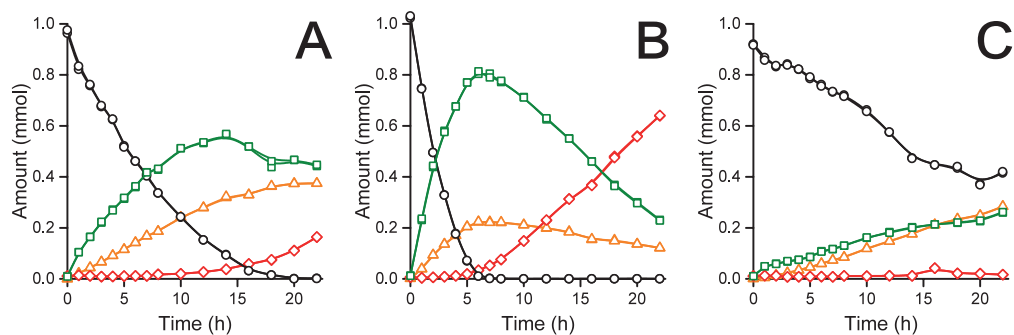


Figure 4.7 Amount of cinnamaldehyde (○) and products, cinnamyl alcohol (□), hydrocinnamaldehyde (△) and hydrocinnamyl alcohol (◇), during the hydrogenation of cinnamaldehyde over supported silver catalysts, Ag/SBA-15_1 (A), Ag/SBA-15_0.1 (B) and Ag/SBA-15_N₂ (C). Conditions: Cinnamaldehyde (1 mmol), catalyst (75 mg 56 wt% Ag/SiO₂, cinnamaldehyde to Ag mole ratio is 2.6), isopropanol (1 mL), water (1 mL), tetradecane (100 μL), hydrogen (40 bar), 70 °C, 900 rpm stirring.

TEM analysis. For the nanowires, only the surface area on the sides of the wires was considered. The obtained TOF values are in line with the activities of silver catalysts in the liquid phase hydrogenation of α,β -unsaturated aldehydes reported in literature [235–237].

For both the catalysts with silver nanowires, cinnamyl alcohol is the main product, whereas similar amounts of hydrocinnamaldehyde and cinnamyl alcohol are produced using Ag/SBA-15_N₂ (see Appendix C, Figure C.9). TEM analysis on the used catalysts (see Appendix C, Figure C.10) show that both catalysts containing silver nanowires were stable and retained their morphology during the hydrogenation reaction. However, this was not the case for both catalysts containing silver nanoparticles, which sintered to form significantly larger particles and nanowires. Since it is unknown when the sintering took place, no reliable conclusions for activity and selectivity based on particle size can be drawn. Still, the considerable difference in activity and selectivity between the catalyst containing nanoparticles or nanowires, suggests that large silver facets are favorable for the hydrogenation reaction, which is in agreement with literature on the hydrogenation of various unsaturated aldehydes [31,33,47].

Even though the nanoparticles were not stable, the low activity of this catalyst compared to the catalysts containing nanowires show that the silver inside the pores of the SBA-15 is active in

Table 4.2 Overview of the catalytic properties of the Ag/SBA-15 composites.

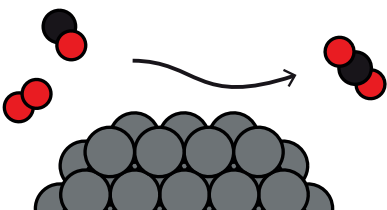
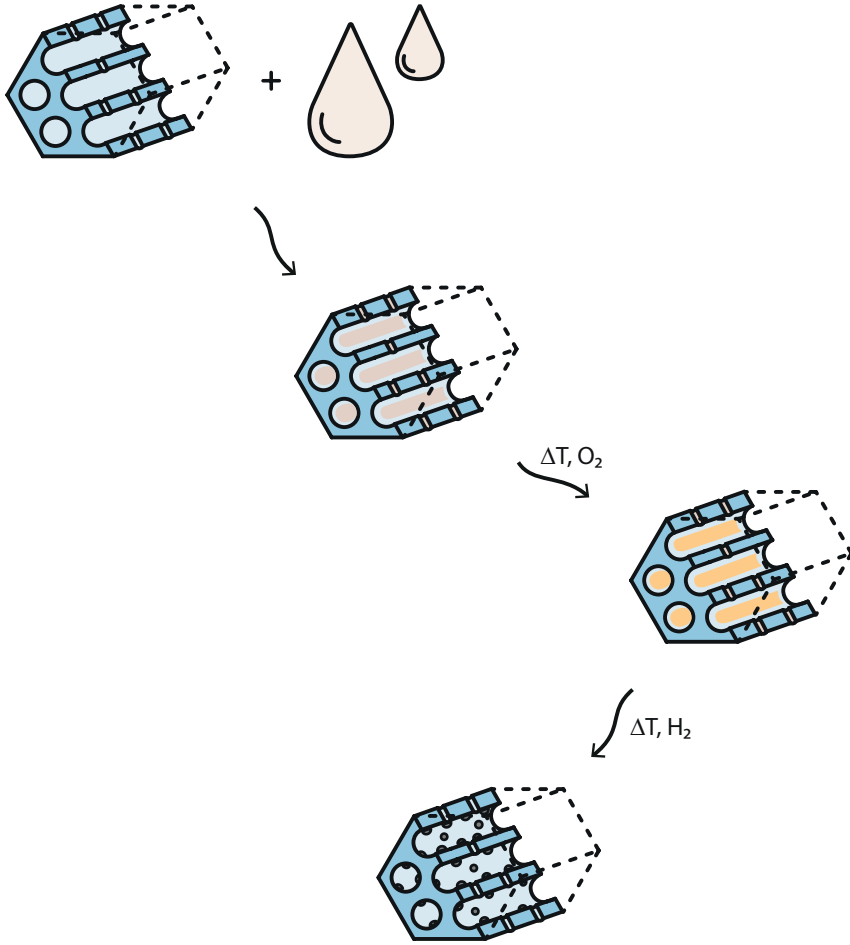
Catalyst	Shape Ag in pores	Ag in pores (%)	TOF Ag in pores ^a (mol _{CALC} mol _{Ag, surf} ⁻¹ h ⁻¹)	Selectivity to CALC at X _{50%} (%)
Ag/SBA-15_1	Nanowires	39	12	70
Ag/SBA-15_0.1	Nanowires	73	12	82
Ag/SBA-15_N ₂	Nanoparticles	19	1.4	50
15Ag/SBA-15_ref	Nanoparticles	N/A	1.0	80

^a Apparent TOF for first hour, based on the initial surface-averaged particle size determined by TEM.

the hydrogenation reaction, and that the activity of the silver outside of the pores can indeed be neglected. This is even further evidenced by the similar apparent TOF values for the two catalysts containing different amounts of silver nanowires. Moreover, this shows that even though the nanowires fill the pores of the SBA-15, the surfaces of the silver nanowires are accessible to the reactants. Most likely, the micropores present in the SBA-15 provide accessibility for products and reactants. This means however, that part of the surface of the silver nanowires is covered by the silica and therefore, the real active surface area is lower, and hence the real TOF values are even higher for the nanowires than reported here.

4.4 Conclusions

The synthesis of supported silver catalysts via melt infiltration and their application in the selective hydrogenation of cinnamaldehyde has been explored. After melt infiltration, over 90% of the precursor, silver nitrate, was inside the pores of the SBA-15. By subsequent reduction, supported silver catalysts with a weight loading of 56 wt% were obtained. Depending on the temperature of the reduction, either silver nanowires or silver nanoparticles had formed inside the pores. However, after reduction, also some silver was located outside the pores. The external silver particles were significantly larger than those inside the pores and could be neglected when evaluating the catalytic activity. The silver nanowires, although filling the pores of the SBA-15, were accessible for the reactants and provided more active and selective catalysts for the hydrogenation of cinnamaldehyde to cinnamyl alcohol than the silver nanoparticles.



Chapter 5

Utilization of silver silicate for highly dispersed silver on silica catalysts

Supported silver catalysts with small and uniform particle sizes are promising for selective hydrogenation or oxidation reactions. However, during catalyst preparation, transport of the silver precursors often leads to large silver particles, especially at higher silver loadings. In this chapter, the use of silver silicate as an intermediate for the preparation of silica-supported silver nanoparticles is reported. Supported silver silicate was prepared by reacting silver nitrate with silica. Subsequently, the silver silicate was reduced to prepare supported silver nanoparticles of ~ 2 nm in size at a loading of 15 wt% Ag. The utilization of silver silicate limited the transport of silver species during precursor decomposition, resulting in silver nanoparticles being 20 times smaller than those formed by direct reduction of a supported silver nitrate precursor. The catalysts were applied in carbon monoxide oxidation, which confirmed the high dispersion as well as the excellent stability of the supported silver nanoparticles thus prepared.

5.1 Introduction

As seen in Chapter 4, redistribution of the precursor both during the drying and precursor decomposition step may lead to large intra- and interparticle heterogeneities in the metal distribution, especially at relatively high metal loadings. Extensive research is dedicated to understanding and limiting this precursor redistribution [56–59]. There are several ways to prevent agglomeration of the metal during the decomposition step, including providing a stronger interaction between the support and the precursor or by changing decomposition parameters such as atmosphere and heating ramp to change the deactivation pathways [55,62–64]. Another way is to form an immobile intermediate, such as a metal silicate, to be further decomposed in a later step to form the desired metal nanoparticles [65]. By utilizing copper or nickel silicates as intermediates, supported copper or nickel catalysts with a high dispersion and narrow particle size were prepared, even at metal loadings up to 40 wt% [56,66–70]. To the best of our knowledge, deliberately utilizing the formation of silver silicate as an intermediate in the preparation of supported silver catalysts has not yet been explored.

In literature, preparation routes for several different silver silicates can be found [71–75]. These silver silicate compounds are proposed as photocatalysts, as they show a higher activity compared to metallic silver [76–83]. Whereas the synthesis of pure and highly crystalline silver silicate generally takes place under high oxygen pressures, supported silver silicate can be synthesized by letting a silica source react with silver nitrate at atmospheric pressure [84,85]. Also during the synthesis of supported silver nanoparticles on silica, silver silicate may form. In Chapter 4, we observed the formation of silver silicate upon the synthesis of supported silver catalysts using melt infiltration of silica with molten silver nitrate. Here, large crystallites of silver silicate were formed because of a high silver loading, which allowed us to identify the structure using X-ray diffraction. As the formation of silver silicate took place upon reacting silver nitrate and silica at elevated temperatures, many studies on the preparation of silica-supported silver nanoparticles, probably unknowingly involved the formation and decomposition of silver silicate. In some studies, these silver silicate species were designated as silver oxide, even when the temperatures used during heat treatments exceeded the decomposition temperature of silver oxides [238–242].

In this chapter, the use of silver silicate as an intermediate for the preparation of supported silver nanoparticles is discussed, also to better understand the role of silver silicate during the synthesis of supported silver catalyst. By using SBA-15 as model silica support material, we investigated both the formation of silver silicate in itself, and its influence on the structure of the SBA-15. Next, we studied the decomposition of silver silicate into highly dispersed silica-supported silver nanoparticles, and finally, the catalytic performance of these nanoparticles in the oxidation of carbon monoxide.

5.2 Experimental methods

5.2.1 Synthesis of silver silicate

SBA-15 was prepared via a sol-gel synthesis, according to the procedure described in Chapter 4. A silver precursor was deposited on the SBA-15 via incipient wetness impregnation. In a typical

synthesis, the SBA-15 powder was dried under dynamic vacuum in a round bottom flask at 200 °C for 2 h. Silver nitrate (99+%, Sigma-Aldrich) was dissolved in demineralized water. The amount of demineralized water was 90% of the pore volume of the support. The amount of silver nitrate was adjusted to obtain materials with a calculated loading of 15, 35 or 55 wt% silver upon full decomposition of the silver precursor. The precursor solution was added dropwise to the support material, under vacuum. A uniform distribution of the precursor solution over the support was facilitated by stirring the powder using a stirring bar. After the addition of the precursor, the material was dried overnight under dynamic vacuum at room temperature, under continuous stirring. The dried material, white powder (75–150 μm), was heated to 400 °C for 2–6 h (2 °C min^{-1} heating ramp) in a 100% oxygen or nitrogen flow. The temperature chosen is in between the melting temperature (212 °C) and the decomposition temperature (440 °C) of silver nitrate. After this heat treatment, the color of the material was orange, with a darker orange to brown-red color for materials with a higher silver loading.

5.2.2 Synthesis of supported silver nanoparticles

The silver silicate powder was treated at 150 °C for 1 h (0.5 °C min^{-1} heating ramp) in a flow of 1–10% carbon monoxide or hydrogen in nitrogen to decompose the silver precursor. A reference catalyst with a calculated loading of 15 wt% Ag was prepared by direct reduction of silver nitrate on SBA-15 after impregnation and drying. For this, SBA-15 was impregnated with silver nitrate and dried overnight, the same way as described above, then treated at 150 °C for 1 h (0.5 °C min^{-1} heating ramp) in a flow of 1% hydrogen in nitrogen.

5.2.3 Characterization

The pore size, pore volume and surface area of the materials were analyzed using nitrogen physisorption. Isotherms were measured at -196 °C on a Micromeritics TriStar 3000 apparatus. The specific surface area of the support was calculated using the BET equation ($0.05 < p/p_0 < 0.25$). The support material and silver-containing materials were analyzed by transmission electron microscopy (TEM) using bright field and high-angle annular dark-field mode on the Talos L120C and Talos F200X microscopes, operated at 120 and 200 kV, respectively. TEM samples were prepared by dispersing a dry powder onto a TEM grid, or via dropwise addition of a dispersion of the material in ethanol obtained by sonication to a TEM grid. To limit the decomposition of silver silicate materials by the electron beam, the TEM grids containing these materials and grid holder were cooled with liquid nitrogen to circa -180 °C during the measurements. Crystal phase analysis was performed using X-ray diffraction (XRD) on a Bruker D2 Phaser diffractometer, equipped with a Co K_{α} source ($\lambda = 0.1789$ nm). The composite structures were analyzed by comparing the diffractograms with crystal structures from the PDF-4+ 2016 database. Crystallite sizes were calculated from fits made using TOPAS V5 software. For details on the surface-averaged particle sizes and the particle size distributions obtained using TEM, and on the calculated crystallite sizes using XRD and TOPAS, see Appendix D, Section I. The weight loss of silver silicate during heating was determined using thermal gravimetric analysis (TGA) performed in a Perkin Elmer TGA 8000 equipped with a mass spectrometer (MS). 10–30 mg material was heated up to 700 °C (5 °C min^{-1} heating ramp) in a flow of argon or 5% hydrogen in argon (100 mL min^{-1}).

5.2.4 Catalytic testing

The catalytic performance of supported silver catalysts was investigated for the oxidation of carbon monoxide. In a typical catalysis experiment, 25 mg of catalyst grains (75–150 μm) diluted with 200 mg SiC (212–425 μm) was loaded in a plug flow reactor with an inner diameter of 4 mm between two layers of quartz wool. The reaction was carried out at 30–200 $^{\circ}\text{C}$ (1 $^{\circ}\text{C min}^{-1}$ heating ramp) at atmospheric pressure, in a flow of 20 or 40 mL min^{-1} containing 1% carbon monoxide and 1% oxygen in helium, resulting in a gas flow rate of 320 or 640 $\text{L g}_{\text{Ag}}^{-1} \text{h}^{-1}$. For the determination of the reaction order, the reaction was carried out at 50 $^{\circ}\text{C}$, with a gas flow rate of 640 $\text{L g}_{\text{Ag}}^{-1} \text{h}^{-1}$ and the concentration of carbon monoxide or oxygen was varied between 0.5% and 1.5%, while keeping the concentration of the other reactant at 1%. For details on reaction orders and activation energies, see Appendix D, Section II. The reaction products were analyzed every 2 min using online gas chromatography (Interscience) equipped with two separate channels containing an MXT-Msieve 5A column and an MXT-Q column, two thermal conductivity detectors and a flame ionization detector. The conversion of carbon monoxide during the oxidation reaction was calculated using Equation 5.1. X_{CO} stands for the conversion (in %) and p_{CO} is the partial pressure of carbon monoxide (in Pa).

$$X_{\text{CO}} = 1 - \frac{p_{\text{COout}}}{p_{\text{COin}}} \cdot 100\% \quad (5.1)$$

The apparent turnover frequency (TOF), in mole of carbon monoxide converted per mole silver surface per hour, was determined using Equation 5.2, where P is the pressure (101325 Pa), u is the flow velocity of carbon monoxide (in $\text{m}^3 \text{h}^{-1}$), R is the gas constant (8.314 $\text{J mol}^{-1} \text{K}^{-1}$), T is the ambient temperature (298 K), m is the mass of silver used (in mol), $V_{\text{Ag atom}}$ the volume of a silver atom (in m^3), $A_{\text{Ag atom}}$ the surface area of a silver atom (in m^2) and $d_{\text{p,s}}$ is the surface-averaged diameter of the silver particles (in m), used to calculate the dispersity (using an Ag atom radius of $1.44 \cdot 10^{-10}$ m). Assumed was that the silver particles were spherical and that the silver surface atoms were the active sites. The first part of Equation 5.2 was used for determining the amount of carbon monoxide converted (in mol h^{-1}), and the bottom of the last part was used to estimate the silver surface (in mol).

$$\text{TOF} = \frac{P \cdot u_{\text{CO}} \cdot X_{\text{CO}}}{R \cdot T} \cdot \frac{1}{m_{\text{Ag}} \frac{6 \cdot V_{\text{Ag atom}}}{A_{\text{Ag atom}} \cdot d_{\text{p,s}}}} \quad (5.2)$$

5.3 Results and discussion

5.3.1 Silver silicate

The silver silicate formation was studied using X-ray diffraction (XRD). Figure 5.1, Frame A, shows the diffractograms of pristine SBA-15 (black line), and of SBA-15 impregnated with silver nitrate and heat treated at 400 $^{\circ}\text{C}$ in oxygen (dark orange line). The theoretical silver loading of this material was 55 wt% assuming full decomposition of the silver precursor. The diffractogram of pristine SBA-15 only shows a broad peak around 27 $^{\circ}$, known for amorphous silica. After impregnation and drying and a heat treatment at 400 $^{\circ}\text{C}$ in oxygen, sharp peaks especially in the region of 35–48 $^{\circ}$ had formed, whereas the broad silica peak was no longer observed. In Appendix D, Figure D.5, the diffractogram is compared to the diffraction patterns of silver oxides

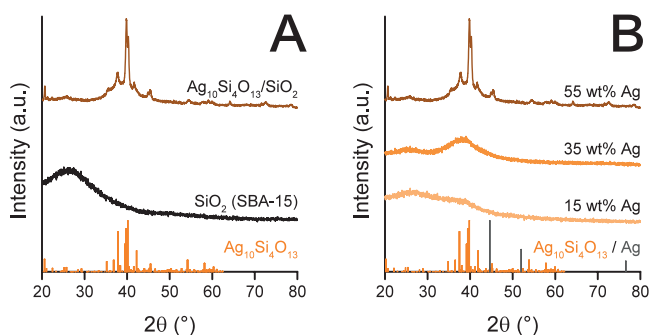
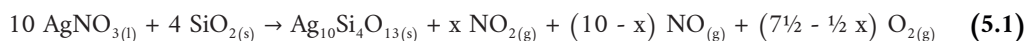


Figure 5.1 Diffractograms of pristine SBA-15 and silver silicate structures with silver loadings of 55 wt% Ag, 35 wt% Ag and 15 wt% Ag. As a reference, crystal structures of silver silicate (orange) and silver (gray) are added. The diffractograms are offset for clarity.

(AgO or Ag₂O) and other silver silicate materials, with Ag : Si ratios of 1–5. As in Chapter 4, the peak positions of the material obtained after the heat treatment shows an excellent match with the silver silicate crystal structure Ag₁₀Si₄O₁₃. The silver silicate had presumably formed following Chemical Equation 5.1.



The sharp peaks of the silver silicate with the highest silver loading indicate the formation of large crystals. The temperature of the heat treatment (400 °C) was close to the decomposition temperature of the silver nitrate (440 °C). Both silver silicate and metallic silver formed when nitrogen was used during the thermal treatment (see Appendix D, Figure D.6). Therefore, to prevent the formation of metallic silver, it is important to perform the heat treatment in an oxygen-containing atmosphere. Presumably, the presence of oxygen stabilizes the molten silver nitrate.

In Frame B, diffractograms of materials containing silver silicate with varying theoretical silver loadings are shown. The broad silica-related peak at 27 ° is present in the materials containing 15 and 35 wt% silver, which shows that less silica had reacted than in the material containing 55 wt% silver, although the intensity of these peaks is still much lower compared to the peak at 27 ° in the diffractogram of pristine SBA-15. Furthermore, these diffractograms do not contain any sharp peaks. Instead, for both samples a broad peak around 42 ° is visible, which is ascribed to amorphous silver silicate [243,244]. A broad peak at this location has been ascribed to silver oxide in literature before [238–242]. However, as silver oxides decompose below or around 200 °C, it is highly unlikely to be present after the heat treatment at 400 °C. Moreover, the orange color of the material is in line with literature [75,243,245]. These considerations, and the location of the broad peak at 42 ° coinciding with the location of the most intense peaks of the silver silicate structure, confirm the formation of the silver silicate.

The pore structure of the silver silicate materials was investigated using nitrogen physisorption. Figure 5.2 shows the isotherms (Frame A) and the pore volume distributions (Frame B) of

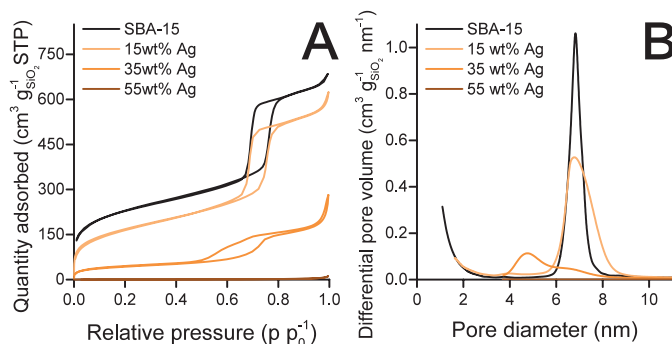


Figure 5.2 Nitrogen physisorption isotherms (A) and the corresponding pore size distributions (desorption, B) of pristine SBA-15 and silver silicate materials varying in silver loading.

pristine SBA-15 (black line) and the silver silicate materials (orange lines). Compared to pristine SBA-15, the surface area and volume of the silver silicate material containing 15 wt% silver was only slightly decreased, indicating that no significant deformation of the structure had occurred. However, upon increasing the silver loading, the surface area and pore volume decreased drastically. The collapse of the porous structure was observed in transmission electron microscopy (TEM) images of these materials (see Appendix D, Figure D.7). While some porosity was still present in the material containing 35 wt% silver, complete destruction of the pore structure resulted in the loss of all porosity for the 55 wt% material.

Supported silver particles were formed upon thermal decomposition or reduction of the silver silicate. Figure 5.3 shows the results of thermal gravimetric analysis (TGA) combined with mass spectrometry (MS). In argon, the thermal decomposition of silver silicate started around 440 °C (Frame A), while the reduction in hydrogen already started around 125 °C (Frame B). During the thermal decomposition of the silver silicate, oxygen was released, while during the reduction, water formed (MS signal, blue lines). No other decomposition products, such as nitrogen oxides,

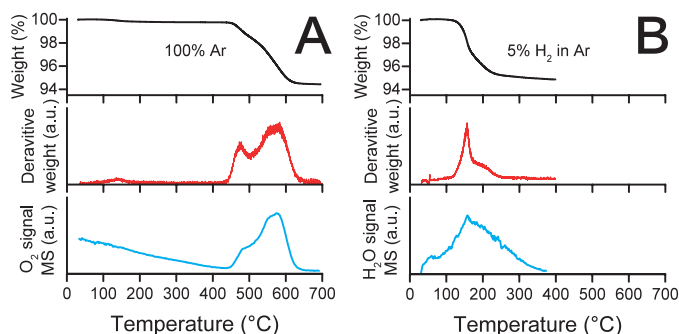
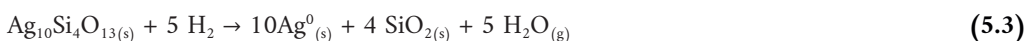


Figure 5.3 Decomposition of silver silicate with 55 wt% silver followed using TGA-MS with a heating ramp of 5 °C min⁻¹. The weight (top) and the derivative of the weight (middle) indicate the decomposition of silver silicate starting around 440 °C in an inert atmosphere (A), and around 125 °C in a reductive atmosphere (B). The MS signals (bottom) show the formation of oxygen or water during the decomposition in nitrogen or hydrogen, respectively.

were detected (see Appendix D, Figure D.8). The absence of these nitrogen oxides during the decomposition of silver silicate was in contrast with the nitric oxide and nitrogen dioxide that evolved upon heating supported silver nitrate (see Appendix D, Figure D.9), indicating that all silver nitrate had been converted during the heat treatment at 400 °C. The TGA-MS data show multiple decomposition steps, both during the thermal decomposition and the reduction. Probably some intermediate silver silicate structures varying in Ag : Si : O ratio formed during the decomposition process as has been reported before [71]. The overall thermal decomposition and reduction of the silver silicate presumably takes place via Chemical Equations 5.2 and 5.3, respectively. Considering these reactions and the silver weight loading, a weight loss of circa 4% was expected, which is in line with the measured weight loss of about 5% in both cases.



5.3.2 Preparation of supported silver catalysts

Decomposition of silver silicate via reduction for the materials containing 35 wt% or 55 wt% silver resulted in the formation of metallic silver with a broad particle size distribution (see Appendix D, Figure D.10). We were not able to prepare catalysts with a uniform silver particle size as a result of the tremendous decrease in surface area of the silica support material in combination with the high silver loading. Therefore, for the preparation of supported silver catalysts, we focused on materials containing 15 wt% silver. Supported silver nanoparticles were prepared via silver silicate, and, as a reference, via the direct reduction of silver nitrate on SBA-15. Both hydrogen and carbon monoxide were used to reduce the silver silicate. Table 5.1 summarizes the particle and crystallite sizes of all obtained supported silver nanoparticles discussed below.

Figure 5.4 shows TEM images of the materials after reduction of silver silicate at 150 °C in 1% hydrogen (15Ag_SN_SS-1H₂, Frame A) or 1% carbon monoxide (15Ag_SN_SS-1CO, Frame B) and their diffractograms (Frame C). At the peak position of metallic silver, broad peaks are visible in the diffractograms of both reduced materials, while the broad peak around

Table 5.1 Overview of crystallite sizes and surface-averaged diameters of silver nanoparticles supported on SBA-15, labeled in the form of wt%Ag_P_D_OR, with wt% being the theoretical silver weight loading, P the precursor(s) (SN = silver nitrate, SS = silver silicate), D the atmosphere during decomposition, and OR standing for extra oxidation and reduction treatments, if applicable. The crystallite sizes were obtained via XRD and particle diameters via TEM analysis. See Appendix D, Section I, for particle size distributions and fits of the diffractograms.

Material	Crystallite size (nm)	Diameter (nm)
15Ag_SN_SS-1H ₂	1.3	1.6 ± 0.4
15Ag_SN_SS-1CO	1.6	1.8 ± 0.5
15Ag_SN_SS-1CO_OR	1.7	1.5 ± 0.3
15Ag_SN-1H ₂	32	33 ± 13

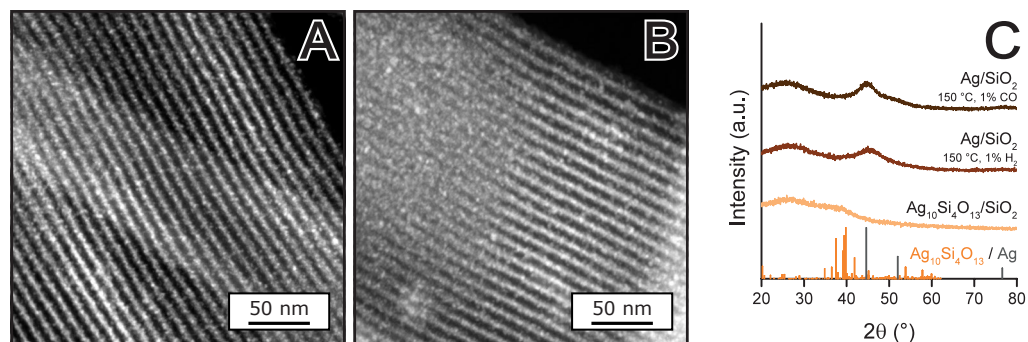


Figure 5.4 TEM images of the supported silver nanoparticles containing 15 wt% silver obtained via reduction of silver silicate in 1% hydrogen in nitrogen (15Ag_SN_SS-1H₂, A) or 1% carbon monoxide in nitrogen (15Ag_SN_SS-1CO, B) and diffractograms of the silver silicate before and after corresponding reductions (C). As a reference, crystal structures of silver silicate (orange) and silver (gray) are added. The diffractograms are offset for clarity.

42 ° is no longer visible. This shows that in both cases the reductions of the silver silicate resulted in the formation of metallic silver nanoparticles. In the TEM figures, next to the pore structure of the SBA-15, ultra-fine, highly dispersed white dots are visible, which are the metallic silver nanoparticles. The surface-averaged diameters of the nanoparticle, 1.6 nm ± 0.4 nm for the hydrogen reduced and 1.8 nm ± 0.5 nm for the carbon monoxide reduced, match the calculated crystallite sizes of the silver (see Table 5.1).

The high dispersion of the silver over the support made it possible to reform silver silicate, upon additional treatment at 400 °C in an oxygen atmosphere for 2 h. Figure 5.5 shows the diffractograms of silver silicate material, and of 15Ag_SN_SS-1CO before and after receiving consecutive heat treatments in an oxidizing (15Ag_SN_SS-1CO_O) and a reducing atmosphere (15Ag_SN_SS-1CO_OR) in Frame A, and a TEM image of the material obtained after the last heat treatment in Frame B. Upon treating 15Ag_SN_SS-1CO at 400 °C in an oxygen atmosphere, the broad peak around 42 °, indicative of silver silicate, had reformed and peaks corresponding

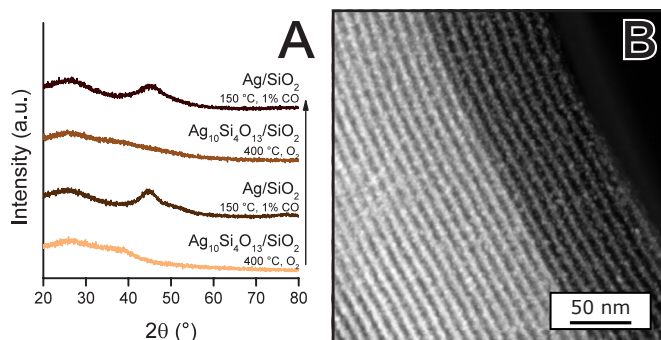


Figure 5.5 Diffractograms of silver-containing structures after various consecutive heat treatments in an oxidizing or a reducing atmosphere (A) and a TEM image of 15Ag_SN_SS-1CO_OR, the material obtained after the last reduction step (B). The diffractograms are offset for clarity.

5

to metallic silver could no longer be detected. The redispersion of silver over support materials, including the formation of silver silicate from silver oxide and silica, has been reported in literature before [71,73,246–248]. However, these changes generally occurred only at high temperatures and/or high oxygen pressures. In our case, due to the high dispersion of the metallic silver over the support, the silver silicate structure could be reformed under relative mild oxidative conditions (atmospheric pressure, 400 °C in oxygen). A second reductive treatment on the reformed silver silicate at 150 °C in 1% carbon monoxide again led to the formation of metallic silver (15Ag_SN_SS-1CO_OR). As shown in Figure 5.5, Frame B, the metallic silver once more was homogeneously distributed over the silica support, in the form of silver nanoparticles. With their surface-averaged diameter of $1.5 \text{ nm} \pm 0.3 \text{ nm}$, these particles were similar in size to the prepared silver nanoparticles before the two additional heat treatments.

The size and dispersion of the supported silver nanoparticles prepared via silver silicate as intermediate are remarkable, especially considering the relatively high silver loading of 15 wt%. To substantiate the effect of utilizing the formation of silver silicate, a reference catalyst, also containing 15 wt% silver, was prepared without the formation of silver silicate. SBA-15 containing silver nitrate was directly reduced at 150 °C, in a flow of 1% hydrogen in nitrogen (15Ag_SN-1H₂). Figure 5.6 shows TEM images of this material and diffractograms of the material before and after reduction. The diffractogram of the reduced material shows sharp peaks with a high intensity at the peak location of silver, indicative of relatively large silver crystals. Silver particles are clearly visible in the TEM images, with a surface-averaged diameter of $33 \pm 13 \text{ nm}$. Next to silver particles, also some silver nanowires had formed. While the wires were located inside the pores of the SBA-15, most of the silver particles were located on the outside of the SBA-15 particles, as is visible in Frame B. Transport and redistribution of the silver precursor, induced by the direct reduction of the silver nitrate, led to an inhomogeneous distribution of the silver over the SBA-15 support. Moreover, this led to a 20-fold increase in silver particle size compared to the materials prepared via the silver silicate route.

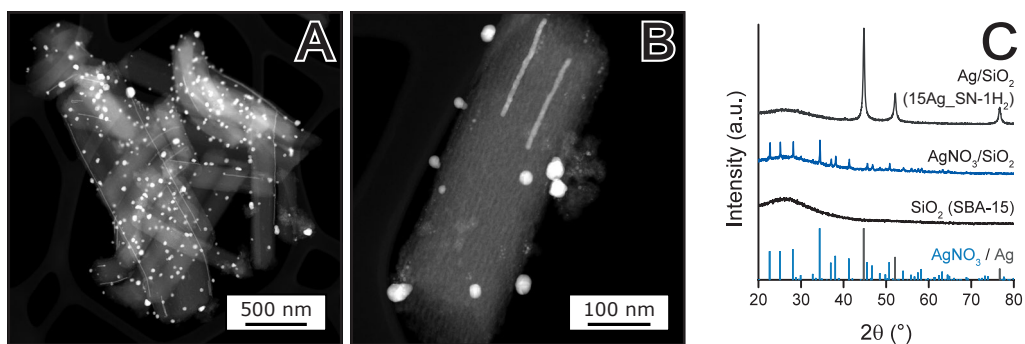


Figure 5.6 TEM images of silica-supported silver nanoparticles containing 15 wt% silver obtained via reduction of silver nitrate in 1% hydrogen in nitrogen (15Ag_SN-1H₂, A, B) and diffractograms of SBA-15, SBA-15 impregnated with silver nitrate and this material upon reduction in 1% hydrogen in nitrogen (C). As a reference, crystal structures of silver nitrate (blue) and silver (gray) are added. The diffractograms are offset for clarity.

5.3.3 Carbon monoxide oxidation

The catalysts were investigated for the oxidation of carbon monoxide to carbon dioxide. The catalytic runs consist of four heating and cooling cycles, two with a gas flow rate of $320 \text{ L g}_{\text{Ag}}^{-1} \text{ h}^{-1}$, and then two with a gas flow rate of $640 \text{ L g}_{\text{Ag}}^{-1} \text{ h}^{-1}$. Figure 5.7 shows the performance of the catalysts during the first two heating and cooling cycles and TEM images of the used catalysts, the catalytic performance during the last two cycles is given in Appendix D, Figure D.11. The catalytic performance of silver silicate reduced using 1% carbon monoxide in helium (similar to 15Ag_SN_SS-1CO) is shown in Frame A. The reduction of the silver silicate was performed in the carbon monoxide oxidation setup, to prevent oxidation of the silver particles before the catalysis started. Directly after the reduction, the catalyst showed a high activity already at room temperature, with 50% conversion of carbon monoxide at $35 \text{ }^\circ\text{C}$ and complete conversion around $100 \text{ }^\circ\text{C}$. This high activity was only observed during the first heating. After the first heating, the activity of the catalyst was lower, and hysteresis was observed.

The catalytic performance of 15Ag_SN-1H₂ is given in Figure 5.7, Frame C. The activity during the first heating was much lower compared to the activities observed during later heating and cooling. In this case, the catalyst had been exposed to air prior to the catalytic reaction, as the reduction was performed *ex situ*. A small silver oxide layer presumably covered the silver nanoparticles, which limited the catalytic activity. Once a temperature of circa $180 \text{ }^\circ\text{C}$ was

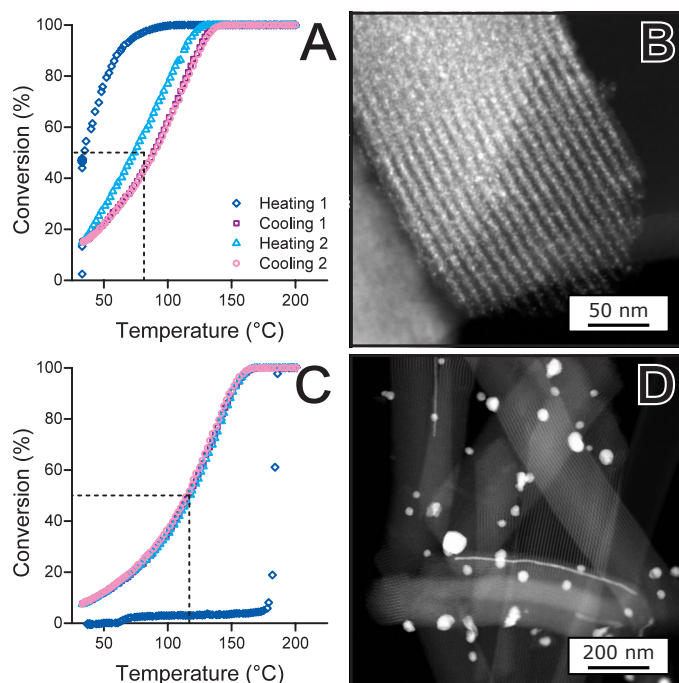


Figure 5.7 Conversion of carbon monoxide versus the reaction temperature during the oxidation of carbon monoxide (25 mg catalyst, gas flow rate of $320 \text{ L g}_{\text{Ag}}^{-1} \text{ h}^{-1}$, $1 \text{ }^\circ\text{C min}^{-1}$) using 15Ag_SN_SS-1CO (A) or 15Ag_SN-1H₂ (C) and TEM images of the used catalysts, respectively (B, D).

reached, the silver oxide decomposed to form the metallic silver and the conversion changed in two minutes time from almost none to full conversion.

In Table 5.2, the temperatures at which 50% of the carbon monoxide was converted ($T_{X=50\%}$) are listed, and Table 5.3 summarizes the apparent turnover frequency (TOF), calculated reaction orders and activation energy of both catalysts (for more details, see Appendix D, Section II). The TOFs per total amount of silver were comparable with values reported in literature [241,249]. The reaction order of carbon monoxide was higher than oxygen, indicating a lower carbon monoxide coverage at the silver surface. For 15Ag_SN_SS-1CO, the difference in $T_{X=50\%}$ between the heating and cooling was 15 °C for both gas flow rates, while the activity did not change significantly during heating or cooling for 15Ag_SN-1H₂. Additionally, the reaction order in carbon monoxide was similar for both catalysts, while the reaction order in oxygen was higher for 15Ag_SN_SS-1CO. This shows that these smaller silver particles were more sensitive to changes in oxygen concentration than the much larger silver particles present in 15Ag_SN-1H₂.

The activity, considered per mol of silver surface, was about 10 times lower on the small silver particles present in 15Ag_SN_SS-1CO, than on the larger silver particles present in 15Ag_SN-1H₂. Presumably, these larger particles were more metallic in nature, which caused a higher activity per active site. However, with a difference in $T_{X=50\%}$ of 30–45 °C, a higher overall activity was obtained for 15Ag_SN_SS-1CO than 15Ag_SN-1H₂, (see Table 5.2). This higher activity mainly results from the large number of active sites, facilitated by the high silver dispersion.

The higher activity on metallic silver surfaces may also explain the higher activity observed during the first heating, and the difference in activity observed during heating and cooling for 15Ag_SN_SS-1CO (Figure 5.7, Frame A). Directly after reduction of the silver silicate, the small silver nanoparticles were fully metallic, and showed a high catalytic activity. However, during catalysis, presumably the silver surface oxidation state and/or surface coverage of these

Table 5.2 Overview of the temperatures at which 50% of the carbon monoxide was converted ($T_{X=50\%}$) during carbon monoxide oxidation reactions.

Catalyst	$T_{X=50\%}$, gas flow rate = 320 L g _{Ag} ⁻¹ h ⁻¹				$T_{X=50\%}$, gas flow rate = 640 L g _{Ag} ⁻¹ h ⁻¹			
	Heating 1	Cooling 1	Heating 2	Cooling 2	Heating 3	Cooling 3	Heating 4	Cooling 4
15Ag_SN_SS-1CO	35 °C	90 °C	75 °C	90 °C	85 °C	100 °C	85 °C	100 °C
15Ag_SN-1H ₂	183 °C	118 °C	115 °C	118 °C	130 °C	130 °C	130 °C	130 °C

Table 5.3 Overview of reaction orders, activation energies and apparent turnover frequencies during carbon monoxide oxidation reactions using a gas flow rate of 640 L g_{Ag}⁻¹ h⁻¹.

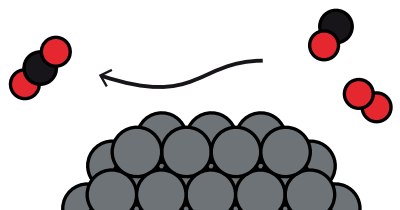
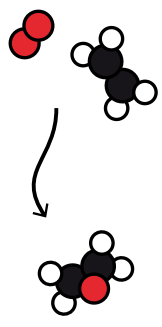
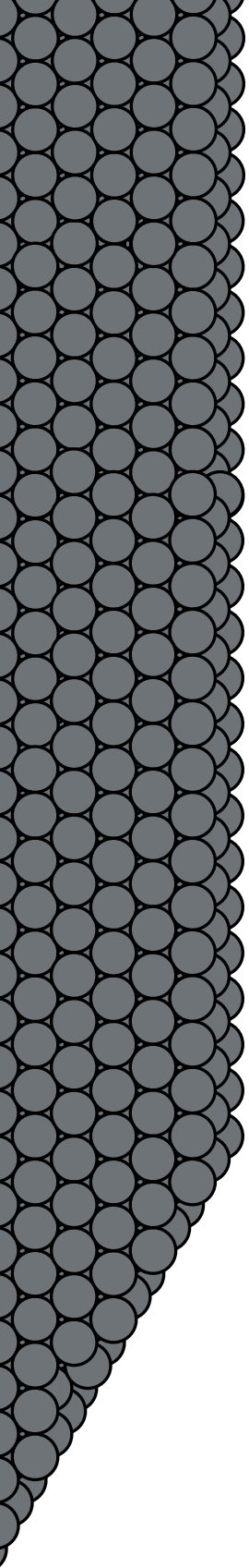
Catalyst	Reaction order		Activation energy (kJ mol ⁻¹)	TOF _{T=50 °C} (h ⁻¹)	
	CO	O ₂		mol _{CO} mol _{Ag,total} ⁻¹	mol _{CO} mol _{Ag,surface} ⁻¹
15Ag_SN_SS-1CO	0.56	0.27	23.3	3.1	4.6
15Ag_SN-1H ₂	0.61	0.10	27.6	1.8	50

highly dispersed silver nanoparticles changed, which in turn changed their activity. Presumably, upon continuous heating or cooling, the time needed for equilibrating was larger than the heating or cooling ramp provided. When the reaction temperature was heated stepwise, and kept at each temperature for a while, no differences in activity upon heating or cooling were observed (see Appendix D, Figure D.12). The corresponding measured conversion levels lied in between the those measured during continuous heating or cooling.

Despite the change in surface coverage, the activity did not change over time apart from the first heating only for 15Ag_SN-1H₂ and for the additional differences in activity between heating and cooling for 15Ag_SN_SS-1CO (see Appendix D, Figure D.11). Both catalysts therefore showed an excellent stability. The high stability of the silver nanoparticles was validated using TEM analysis, in Figure 5.7, Frames B and C, images of the used catalysts are shown. The surfaced average silver particle sizes of the used catalysts were 1.7 nm ± 0.4 nm and 33 nm ± 11 nm for 15Ag_SN_SS-1CO and 15Ag_SN-1H₂, respectively. After heating several times to 200 °C, their sizes were the same as the freshly prepared catalysts shown in Figure 5.4.

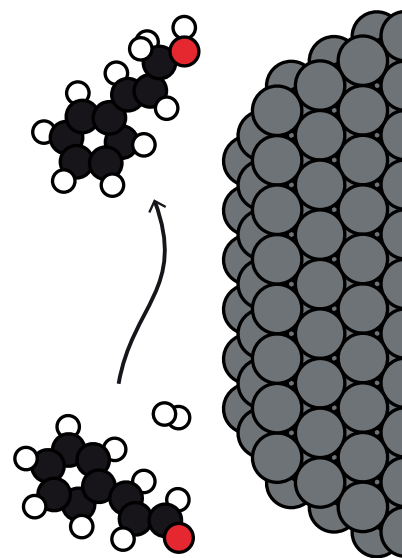
5.4 Conclusions

During the preparation of silica-supported silver catalysts, redistribution of the silver precursor can lead to an inhomogeneous distribution of the silver and the formation of large silver particles. We show the merit of utilizing the formation of silver silicate as an intermediate instead of directly decomposing the silver precursor into its metallic state. Transport of the silver was restricted by first letting the silver precursor, silver nitrate, react with the silica to form silver silicate. This enabled the preparation of highly dispersed silver nanoparticles on silica, even at 15 wt% silver. Silver silicate is readily formed upon heating impregnated silica with silver nitrate in an oxygen-containing atmosphere. For extreme silver loadings of 55 wt%, the formation of crystalline silver silicate in the form of Ag₁₀Si₄O₁₃ was observed, which deformed the pore structure of the silica. However, no deformation of the SBA-15 structure was observed when the silver loading was 15 wt%. Highly dispersed supported silver nanoparticles with a particle size of 1.6 nm and a narrow particle size distribution were obtained. The average size of the obtained silver was 20 times smaller than supported silver particles prepared via direct reduction of silver nitrate on SBA-15. Due to the large number of active sites, the catalyst prepared via silver silicate showed a higher overall catalytic activity in the oxidation of carbon monoxide compared to the catalyst prepared via direct reduction of the silver nitrate. Moreover, the catalyst showed excellent stability, and no particle growth was observed. In conclusion, the utilization of silver silicate allows the preparation of ultra-fine, highly dispersed supported silver nanoparticles, even at high silver loadings. The excellent stability of these silver nanoparticles during the oxidation of carbon monoxide makes them promising candidates for oxidation and possibly also for hydrogenation reactions.



Chapter 6

Conclusions and perspectives



6.1 Conclusions

Supported silver catalysts are essential, since they are used extensively in the chemical industry. In this thesis, research on several aspects of silver catalysts is described. These aspects range from preparing suitable support materials and the preparation of supported silver nanoparticles to the performance of these materials during catalysis. In **Chapter 1**, some background on the preparation and use of supported silver catalysts is given.

The support materials used were mostly model support materials with ordered pore structures. These kind of model systems are important, as they allow advanced characterization such that the influence of specific parameters during preparation or specific silver properties during catalysis can be understood. In **Chapter 2**, the preparation of macroporous α -alumina with a three-dimensionally ordered pore structure and a relatively high specific surface area ($30 \text{ m}^2 \text{ g}^{-1}$) is described. Starting from alumina precursors, the material goes through a number of solid-solid phase transitions, and α -alumina is formed by heat treatment above $1100 \text{ }^\circ\text{C}$. Because of these many phase transitions and the high temperature needed to obtain the α -phase, any porosity present is usually lost as a result of sintering and grain growth. Therefore, porous α -alumina with a high specific surface area is notoriously difficult to prepare.

The preparation method for macroporous α -alumina described in Chapter 2 makes use of a sacrificial polymer template, consisting of poly(methyl methacrylate) (PMMA) spheres, self-assembled into a colloidal crystal. Key to the preparation method is the protection of the porous structure during the heat treatment by a protective carbon coating, formed by pyrolysis of the original polymeric template. This carbon coating delayed the solid-state phase transitions of the alumina. γ -alumina with a high quality ordered macroporous structure still present after the heat treatment at $1150 \text{ }^\circ\text{C}$, instead of α -alumina. By simply applying a second heat treatment at $1150 \text{ }^\circ\text{C}$ in an oxidative atmosphere, the carbon was burned off and the γ -alumina was converted into α -alumina, with only minor losses in the quality of the ordered pore structure.

In **Chapter 3**, the stability of α -alumina-supported silver particles is discussed, to gain insight into the deactivation mechanisms of supported silver particles used industrially for the epoxidation of ethylene. One of the undesired secondary reactions, the oxidation of ethylene oxide into carbon dioxide and water, is facilitated by hydroxyl groups present on the catalyst support. Both the low density of these surface groups on α -alumina and its very low specific surface area, make α -alumina an ideal candidate as support material for this reaction. The major drawback is that the low specific surface area only provides limited stability of the silver particles against growth. This makes the loss of silver surface area as a result of particle growth one of the most important deactivation mechanisms of catalysts used in the epoxidation of ethylene. In order to minimize particle growth during catalysis, it is crucial to understand the underlying mechanism of the silver particle growth. Therefore, in Chapter 3, the growth of silver particles was systematically investigated by supporting them on various α -alumina materials, including the macroporous α -alumina described in Chapter 2. The α -alumina support materials used varied in surface area ($1\text{--}30 \text{ m}^2 \text{ g}^{-1}$), pore structure, and pore size, and the silver was deposited on the catalysts via impregnation.

First, thermal treatments were applied to the supported silver particles, to identify the parameters responsible for silver particle growth. Enhanced growth of the silver particle was found during heating in the presence of oxygen, while the growth was negligible in a hydrogen atmosphere. This indicates that the mobile species responsible for particle growth were oxidized silver species formed on the support surface upon heating the materials in the presence of oxygen. Additionally, a strong dependence of the growth on interparticle distances was found, while restricting the movement of complete silver particles did not slow down particle growth. This points to the fact that Ostwald ripening, rather than the diffusion and coalescence of whole silver particles, is the dominant mechanism behind silver particle growth, with the diffusion of oxidized silver species probably being a rate limiting factor. Additionally, the particle growth and catalytic performance of the supported silver particles during the epoxidation of ethylene were investigated. The cost of using high specific surface areas is a slight decrease in selectivity towards ethylene oxide, but results on catalyst stability were in line with thermal particle growth studies. α -alumina support materials with high specific surface areas, and hence large interparticle distances for the silver particles, substantially enhanced the stability of supported silver particles during the epoxidation of ethylene.

In **Chapter 4**, an alternative preparation method for supported silver catalysts was explored, where the distribution of the silver precursor over the support material was performed by making use of melt infiltration. One of the benefits of using melt infiltration rather than more conventional preparation methods such as impregnation or precipitation, is that melt infiltration is solvent free and can easily produce catalysts with high metal loadings. To explore the possibility of using melt infiltration for catalysts with high metal loadings, catalysts with 56 wt% silver were prepared.

To gain an understanding of both the melt infiltration process and the decomposition of the precursor, the model support material used was SBA-15, an ordered mesoporous silica. The well-defined pore structure allowed advanced *in situ* and *ex situ* characterization of the infiltration process. Upon completion of the melt infiltration, over 90% of the silver nitrate, the used silver precursor, resided inside the pores of the silica support. As a precursor volume corresponding to a pore filling of 50% was used, not all pores were filled completely. For most SBA-15 particles, some of the pores were completely filled, while other pores were completely empty. Even though melt infiltration is a promising method for the synthesis of supported catalysts, the distribution of the active component over the support was not optimal, although this holds for more conventional preparation methods too.

The accumulation of the silver nitrate within the pores made it difficult to control the size of the silver upon the decomposition of the silver nitrate. Supported silver nanowires or spherical nanoparticles were obtained by starting the silver nitrate reduction in hydrogen at room temperature or at 200 °C, respectively. During the formation of the silver wires, which completely filled some of the pores of the SBA-15, presumably decomposition gases could diffuse out of the pore network, while limited transport of the silver species allowed the formation of the silver nanowires inside the support pore structure. Therefore, most of the silver remained inside the SBA-15 particles, especially when using a slow heating ramp. However, during the

formation of silver nanoparticles (circa 2.5 nm, significantly smaller than the diameter of the pores) presumably a large quantity of decomposition gases had formed within a short time, which caused transport of most of the silver mass to the exterior of the support particles. This gave rise to the formation of very large silver particles (200 nm). In both cases however, the surface area of the silver located on the exterior support surface was much smaller than the surface area of the silver inside the pore network due to the large differences in their sizes. Therefore, both materials were investigated for the hydrogenation of cinnamaldehyde. Superior activity and selectivity were obtained using the silver nanowires, compared to when silver nanoparticles were used. The difference in performance probably resulted from the different facets present on the silver nanowires versus the nanoparticles. Additionally, the catalytic results showed that even though the silver nanowires completely filled some of the pores, the silver surface presumably remained accessible for the reactants via the micropores in the SBA-15.

In **Chapter 5**, the utilization of silver silicate during the preparation of silica-supported silver catalysts was explored, in order to have a better control over the transport of the silver precursor during its decomposition. Just as in Chapter 4, SBA-15 was used as model support material, and silver nitrate was used as precursor. To ensure a homogeneous distribution, the silver nitrate was distributed over the SBA-15 via solvent impregnation. Silver nitrate reacted to form silver silicate upon treating the material at 400 °C in an oxygen atmosphere, without the formation of metallic silver. Depending on the silver loading, either amorphous silver silicate or crystalline silver silicate ($\text{Ag}_{10}\text{Si}_4\text{O}_{13}$) formed. The pore structure of the SBA-15 was severely deformed for the materials containing very high silver loading materials (35–55 wt% Ag), whereas no significant deformation of the pore system was observed for materials containing 15 wt% silver. For this last material, still containing a relatively high silver loading, the decomposition of silver silicate in a 1% carbon monoxide in a helium atmosphere at 150 °C resulted in the formation of silver nanoparticles of about 1.5 nm in size. This was about 20 times smaller than the supported silver nanoparticles of the 15 wt% silver reference catalyst, prepared via direct reduction of the impregnated silver nitrate. For the reference catalyst, transport of the silver species during the reduction step led to the formation of these much larger silver particles, mainly at the exterior of the support particles, as observed in Chapter 4. The formation of the silver silicate proved to be an excellent way to affix the silver precursor inside the pores of the SBA-15, restricting transport during its decomposition. By applying both catalysts for carbon monoxide oxidation, the high dispersion of the silver nanoparticles prepared by silver silicate utilization became apparent, as these catalysts showed a much higher activity than the reference catalyst. Additionally, the catalyst showed excellent stability, as the used catalysts showed no growth of the supported particles.

6.2 Perspectives

By the new knowledge about what causes the deactivation of supported silver catalysts and how to prepare them, we can further enhance their functionality. The support material is one of the key enablers to reach higher activity and stability of silver catalysts. The use of an ordered pore structure was vital for exploring alternative catalyst preparation methods, and for finding the dominant growth mechanism of supported silver particles. The pyrolysis of the sacrificial

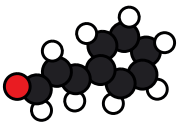
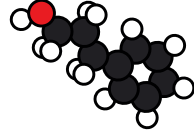
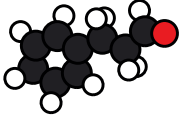
carbon-containing template to form a protective carbon coating is a method that can be applied to induce porosity in a wide range of materials [250–252], as the protective carbon coating is stable up to very high temperatures in an inert gas atmosphere, yet can be easily removed in air. Moreover, a wide variety of carbon materials can be used to form a carbon coating [159,163,253,254]. While we used templating methods to prepare ordered pore structures, there are multiple other ways to prepare ordered model systems, including by making use of lithography, (supra)colloidal systems or atomic layer deposition [76,255–258].

We found that any α -alumina with a relatively high specific surface area will help against silver particle growth. Without the need of an ordered pore structure, preparation routes for α -alumina with high specific surface areas (even exceeding $100 \text{ m}^2 \text{ g}^{-1}$) are reported in literature [164,165,259,260]. Especially the reported preparation route using ball milling of boehmite is of interest, where mechanochemically induced phase transformations at room temperature led to the formation of α -alumina with a high purity and a high specific surface area (circa $140 \text{ m}^2 \text{ g}^{-1}$) [260].

A higher specific surface area of the α -alumina is beneficial for the stability of the silver, but it is accompanied by a larger number of hydroxyl groups, which is detrimental for the selectivity in the epoxidation of ethylene. For silica-supported catalysts used in this reaction, passivation of the hydroxyl groups proved to be very effective to increase the selectivity [216]. For alumina-supported silver used in industry, promoters are added to increase the selectivity. Frequently used promoters are chloride, cesium and rhenium [7]. We found that for our system, without the use of promoters, Ostwald ripening is the dominant mechanism for particle growth. In particular chloride and cesium are expected to influence the stability of the silver and the formation of mobile silver clusters, as these promoters influence the silver-oxygen interaction [261,262]. To better understand the mechanisms at play during industrial ethylene epoxidation, further research on the influence of promoters on the stability of silver is needed.

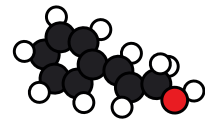
Next to the epoxidation reaction, we discussed the emerging use of supported silver catalysts for selective oxidation or hydrogenation reactions. While silver catalysts exhibit excellent selectivities, the main limitation of silver is its low activity, compared to other metals, including platinum, palladium and gold. By combining these metals with silver in bimetallic catalysts, the selectivity of the reaction can be increased without decreasing the activity too much [263]. Another way to overcome the low volume-based activity of solely silver catalysts is using catalysts with higher silver loadings. Melt infiltration is a promising technique for the preparation of silver catalysts with high metal loadings, although the distribution of the precursor over the support in this work was found to be inhomogeneous. The initial inhomogeneous precursor distribution resulted from using a precursor volume lower than the total pore volume of the support material. Mixing the precursor with a removable substance, so that the complete pore volume can be filled, may result in a more homogeneously distributed precursor throughout the pore network. The added substance could be removed during or after the decomposition of the precursor. Similarly, a removable substance can be used to homogeneously fill a part of the pore network. The remaining pore volume can then be filled with the precursor, whereupon the substance is removed [92–94].

Finally, upon investigating the decomposition of the silver nitrate, we inferred considerable transport of the silver species. We used the formation of silver silicate to limit the mobility of the silver species and afterward focused on the decomposition of silver silicate for the preparation of supported silver catalysts. However, silver silicate as such is reported to be (slightly) active as a photocatalyst and it might be interesting to further explore the catalytic properties of (supported) silver silicate [76,81].





Appendices



Appendix A - Supporting information Chapter 2

Section I - Calculation particle size of polymer spheres via UV/Vis

The average particle diameter of the poly(methyl methacrylate) (PMMA) spheres (D) can be estimated using Diffuse-Reflectance Ultraviolet/Visible (DR UV/Vis) spectroscopy. The unit cell parameter of the PMMA crystal (a) and C , the conversion factor between the two based on the crystal structure and diffraction plane can be used to determine the average particle size from the interplanar spacing d_{hkl} with Equations A.1 and A.2. We assume the colloidal crystal is stacked in a closed packed crystal structure. In Equation A.2, h , k and l are the lattice planes.

$$D = C \cdot a \quad (\text{A.1})$$

$$d_{hkl} = \frac{a}{\sqrt{h^2+k^2+l^2}} \quad (\text{A.2})$$

The interplanar spacing is obtained by using Equation A.3, in which m is the order of the Bragg diffraction, λ is the wavelength of the peak positions in the DR UV/Vis spectrum, $n_{\text{material,avg}}$ is average the refractive index of the material and θ is the angle between the incident light and the surface normal of the sample. The average refractive index of the PMMA crystal is calculated using Equation A.4, in which φ is the filling factor.

$$m\lambda = 2d_{hkl}\sqrt{n_{\text{material,avg}}^2 - \sin^2\theta} \quad (\text{A.3})$$

$$n_{\text{material,avg}} = n_{\text{material,bulk}} \cdot \varphi_{\text{material,bulk}} + n_{\text{air}} \cdot \varphi_{\text{air}} \quad (\text{A.4})$$

By combining Equation A.1 to A.4, and assuming $\theta = 0$ at the peak optimum due to diffraction at normal incidence [180], the particle size can be calculated using Equation A.5.

$$D = \frac{m\lambda}{2C \cdot \sqrt{h^2+k^2+l^2} n_{\text{material,avg}}} \quad (\text{A.5})$$

$$2C \cdot \sqrt{h^2+k^2+l^2} = 1.633 \quad (\text{A.6})$$

For a closed packed crystal structure, Equation A.6 can be used. The fraction of PMMA, $\varphi_{\text{PMMA,bulk}}$ is 0.26 and the fraction of air, φ_{air} is 0.74. $n_{\text{PMMA,bulk}}$ is 1.492 at 25 °C [264], which gives $n_{\text{PMMA,avg}}$ a value of 1.364.

A

Section II - Heat treatment of (impregnated) template

The weight loss during heat treatment was determined using thermal gravimetric analysis (TGA) performed in a Perkin Elmer Pyris 1 TGA under a 10 mL min⁻¹ flow of 20% oxygen in nitrogen. For these experiments the temperature was increased from 50 °C to 500 °C (5 °C min⁻¹ heating ramp). Figure A.1 shows the mass loss upon heating of the polymer template in air, ascribed to the burning off of the polymeric material, at 250 °C. The weight loss remained stable above circa 350 °C.

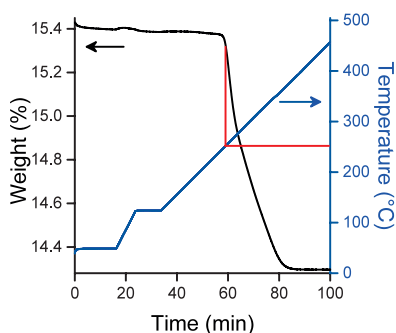


Figure A.1 Decomposition of the polymer template in air flow followed using TGA (black line) and the temperature program used (blue line).

In Figure A.2, three pictures show the impregnated template before (Frame A) and after heat treatments (Frames B and C). After a single heat treatment in nitrogen at 1150 °C for 6 h, a blue/green/black powder is obtained. After a second heat treatment in air at 1150 °C for 6 h, the material turned pristine white again. The volume and weight of the material decreased significantly during the first and only slightly during the second heat treatment. The volume and weight after two heat treatment steps are the same within experimental error as when the impregnated template was heat treated in an air flow directly.

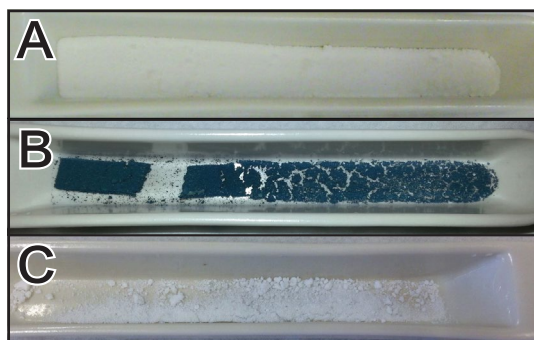


Figure A.2 Pictures of impregnated template with aluminum hydroxide before heat treatment (A), carbon-alumina composite after heat treatment under a nitrogen flow (B) and α -alumina after heat treatment in a nitrogen flow and subsequent heat treatment in air flow (C).

Section III - Additional analysis data of three-dimensional ordered macroporous γ -alumina

By performing the second heat treatment in air at 900 °C, the carbon was removed from the sample. At this temperature, the γ -alumina phase was maintained, as can be seen from the diffractogram in Figure A.3. Figure A.4 shows scanning electron microscopy (SEM) images of three-dimensionally ordered macroporous γ -alumina material obtained after a single heat treatment in an inert atmosphere in Frame A and the carbon-free macroporous γ -alumina obtained after a sequential heat treatment in an oxidizing atmosphere at 900 °C in Frame B. Both materials show a structured material with a recurring hexagonal pattern. The nodes and sticks in this material are nearly the same thickness, as opposed to the more rounded nodes and thinner sticks interconnecting the nodes in α -alumina visible in Figure 2.4 (Chapter 2).

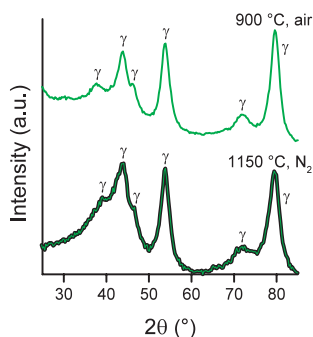


Figure A.3 Diffractograms of carbon-coated γ -alumina after heat treatment of infiltrated template at 1150 °C in a nitrogen flow (bottom) and carbon-free three-dimensionally ordered macroporous γ -alumina after a second heat treatment at 900 °C in an air flow to burn away the protective carbon layer (top). The diffractograms are offset for clarity.

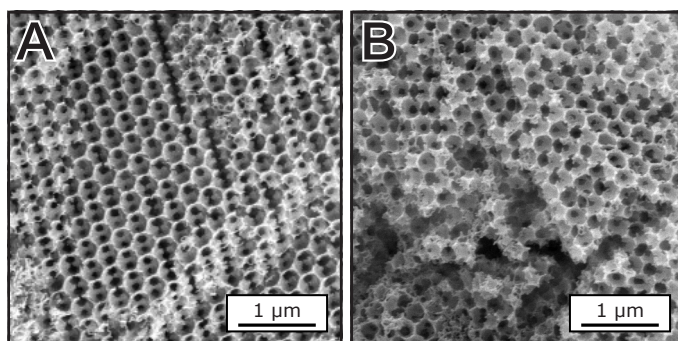


Figure A.4 SEM images of γ -alumina after heat treatment under a nitrogen flow (A) and after heat treatment under a nitrogen flow and subsequent air flow at 900 °C (B).

Section IV - Additional analysis data of three-dimensional ordered macroporous α -alumina

When the impregnated template was heated to 1150 °C in a nitrogen atmosphere, the γ -alumina phase remained predominant, as can be seen in the bottom diffractogram in Figure A.5. However, when this sample was heat treated a second time in an air flow at 1150 °C, only α -alumina diffraction peaks are visible (top diffractogram in Figure A5).

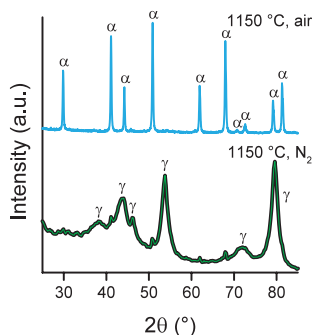


Figure A.5 Diffractograms of impregnated template heated to 1150 °C for 6 h in a nitrogen flow (bottom) and of this material after subsequent heat treatment at 1150 °C for 6 h in an air flow (top). The diffractograms are offset for clarity.

The surface area of the material is measured using nitrogen physisorption and mercury intrusion. Figure A.6 shows nitrogen physisorption results of 3DOM_3_N₂-air. The isotherms (Frame A) show no significant micro- or mesoporosity. A small hysteresis loop at high relative pressures is visible due to filling of interparticle and macropores. The particle size distribution (Frame B) from the desorption branch of the isotherm shows a sharp peak at 80-90 nm. Unfortunately, these pores are at the edge of the range in which nitrogen physisorption provides accurate data [265]. The 200 nm cages visible in SEM are therefore not probed with nitrogen physisorption and the observed pores are attributed to the windows of the macropores.

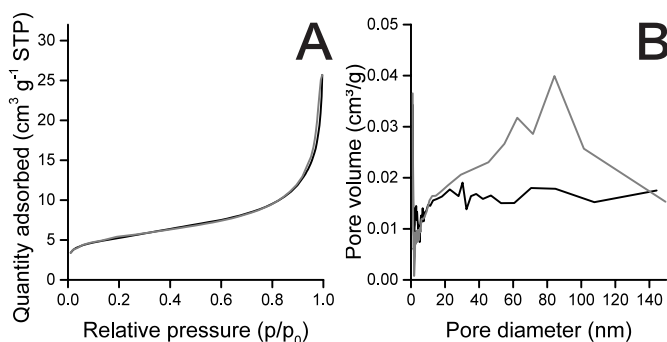


Figure A.6 Nitrogen physisorption isotherms (A) and the corresponding pore size distribution (B) of the adsorption (black) and desorption (gray) data on ordered macroporous α -alumina (3DOM_3_N₂-air).

Figure A.7 shows mercury porosimetry results of 3DOM_3_N₂_air. In Frame A, the isotherm of the intrusion step shows a multistep intrusion. The intrusion step at pressures of 0.01 to 0.2 MPa originates from filling interparticle pores, corresponding to 100-10 μm pores respectively. The second intrusion step occurs at 1 to 10 MPa, corresponding to the filling of 1-0.1 μm pores. In Frame B, the corresponding pore size distribution is shown. As the pore diameter is plotted against the surface area, the filling of the interparticle volume is reduced to a very small peak between 10¹ and 10² μm in the pore size distribution, while the filling of the 100-10 μm pores results in a large peak due to the inverse correlation between pore volume and surface area.

The pore size distribution shows a sharp peak at 100 nm, with a small shoulder around 300-500 nm corresponding to interparticle pores. Since the isotherm is measured during intrusion, this peak at 100 nm is ascribed to the windows of the material instead of to the cages themselves. The value of 100 nm for the window size is in agreement with nitrogen physisorption measurements and measurements performed on SEM images. As a result of the ink bottle morphology of the α -alumina, the mercury is retained inside the cages of the material during the extrusion step of the analysis [266]. Therefore, the cage size cannot be obtained by using mercury intrusion porosimetry.

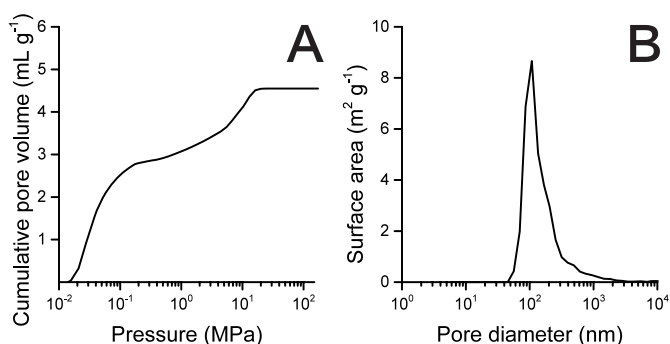


Figure A.7 Mercury intrusion porosimetry intrusion isotherm (A) and the corresponding pore size distribution (B) of ordered macroporous α -alumina (3DOM_3_N₂_air).

A common characterization technique for porous materials is electron microscopy. Figure A.8 shows an SEM image of a typical ordered macroporous α -alumina particle (3DOM_3_N₂_air), in which the pore structure ordering at a large scale is visible.

Due to the large pores of macroporous material, the grain size of the particles is too thick for transmission electron microscopy (TEM), while SEM does not provide insight in the porosity throughout the particle. By using microtomography and focused ion beam (FIB)-SEM (Nova-NanoLab600), the pore structure throughout the particle was visualized. A dispersion of α -alumina powder in a mixture of resin (polymer Epo-Fix cat. #1232) and hardener (ratio 2:15) was placed in an oven at 60 °C overnight to harden. This material was cut in slices and placed onto a TEM grid. Figure A.9, Frame A displays a microtomography of a 400 nm thick slice of a 3DOM_3_N₂_air particle. This thickness was chosen to be able to visualize two stacks of unit

cells in a single slice (top left image). In the top right and bottom left, the same slice is shown with a number of cages in a crystal plane denoted by black or white circles to guide the eye. In the bottom right image in this frame, the circles are overlaid to show a closed packed crystal structure. Frame B shows an SEM image after a focused ion beam was used to etch away the surface of a 3DOM_3_N₂_air particle, exposing porosity within the particle, even for sections in which the outer surface appears non-porous.

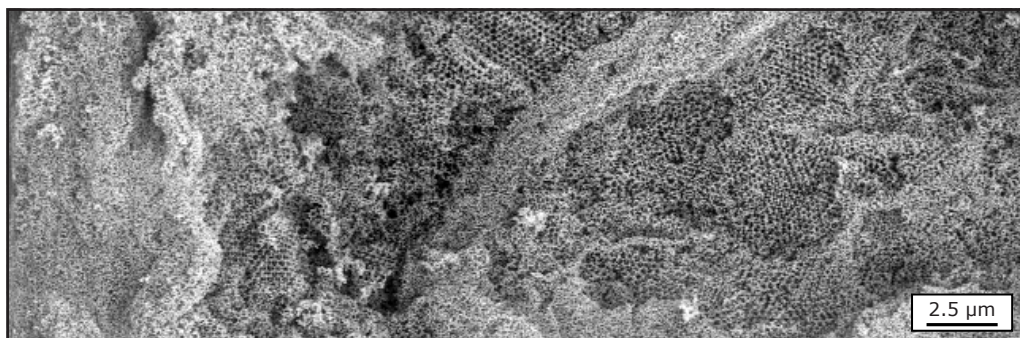


Figure A.8 SEM image of a typical 3DOM_3_N₂_air particle showing macroporosity extended over the entire particle surface, obtained after heat treatment in a nitrogen flow and subsequent heat treatment in an air flow.

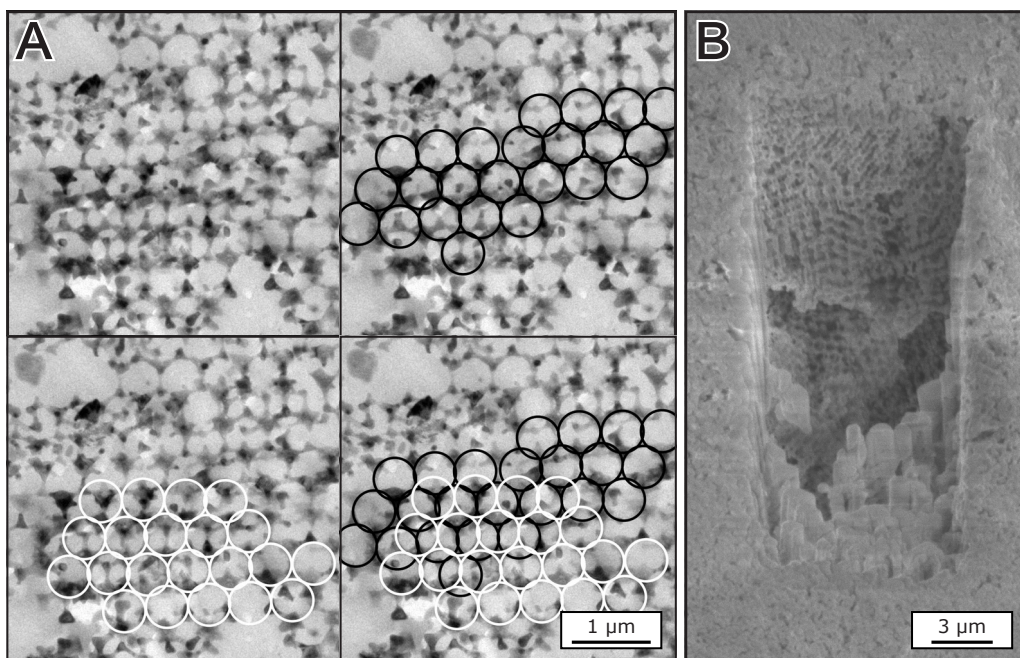


Figure A.9 Four times the same TEM image of microtomed 3DOM_3_N₂_air with a sample thickness of 400 nm obtained from the center of an α -alumina particle, with black and white circles added to indicate two layers of unit cells (A) and a FIB-SEM image of 3DOM_3_N₂_air in which 7.5 μm of the alumina top layer was removed using a focused ion beam, showing the ordered pore structure inside the particle (B).

Section V – Theoretical surface area of three-dimensional ordered macroporous α -alumina

The theoretical surface area of ordered macroporous α -alumina was calculated by dividing the surface area of one cage by the mass per cage. For this, a close packing of the pores was assumed. The used pore diameter and window size are 220 nm and 100 nm, respectively.

The surface area of a cage was calculated as follows: The surface area of one cage (without taking the loss of surface area due to the windows into account) is $1.52 \cdot 10^{-13} \text{ m}^2$ ($4 \cdot \pi \cdot r^2$). When assuming a close packed pore ordering such as fcc or hcp 12 windows are present per cage. These windows have a radius of 50 nm, which surface area needs to be subtracted from the total surface area. The surface area of one window, neglecting its curvature, is $7.85 \cdot 10^{-15} \text{ m}^2$ ($\pi \cdot r^2$). The total surface area of one pore is therefore $5.78 \cdot 10^{-14} \text{ m}^2$.

The mass of the alumina around one cage was calculated by dividing the volume of the cage by the volume fraction of air when assuming the inverse of a closed packed ordered structure, which is 0.74 (1-filling factor). This gives a volume of $7.53 \cdot 10^{-15} \text{ cm}^3$. An average density of the macroporous material of 1.03 g cm^{-3} is calculated the same way as the average refractive index (Equation A4). This gives the cage including the surrounding material a mass of $7.74 \cdot 10^{-15} \text{ g}$. In this case, the calculated theoretical surface area is $7.5 \text{ m}^2 \text{ g}^{-1}$.

Using the red shift in DR UV/Vis spectroscopy, we found that the filling factor is not 0.26, as is assumed for a closed packed structure, but 0.16 for 3DOM_3-N₂_air (Table 2.2). If we use this value, a theoretical surface area of $13.8 \text{ m}^2 \text{ g}^{-1}$ is obtained. From SEM images, the number of windows per pore seems to be lower than 12. The true surface area of the material would therefore probably be slightly higher, as the surface area increases with a lower number of pores per cage.

Appendix B - Supporting information Chapter 3

Section I - Calculations of mass and heat transfer during ethylene epoxidation

The occurrence of potential external or internal mass transfer limitations was checked using the Mears criterium (C_M , Equation B.1) and the Weisz-Prater criterium (C_{WP} , Equation B.2), respectively. External and internal heat transfer limitations were checked using Equations B.3 and B.4, respectively. In these equations, $r'_{A(\text{obs})}$ is the measured rate of the reaction in component A, m_{cat} is the mass of the catalyst used, V_{cat} is the volume of the catalyst used, ρ_{cat} is the density of the catalytic particles, R_{cat} is the radius of the largest catalyst particles, n is the reaction order, k_A is the mass transfer coefficient (calculated using the Sherwood number, Equation B.5, with D_{AB} the diffusivity of component A in B, u the flow velocity of the fluid (f) and μ the kinetic viscosity), C_A is the concentration of component A in the bulk (b) or on the catalyst surface (s), D_{eff} is the effective diffusivity (Equation B.6) with ϕ_{cat} being the porosity, σ_{cat} the constriction factor and τ_{cat} the tortuosity), Ca is the Carberry number, β is the Prater number for extern (e) and intern (i) heat transfer, γ is the dimensionless activation energy, a_s is the geometric surface area of the catalyst particle ($3/R$), ΔH is the reaction enthalpy for ethylene combustion (as this produces the most heat), h is the heat transfer coefficient (calculated using the Nusselt number, Equation B.7, with $Nu = 3.66$ for convection in a circular reactor with a uniform temperature, d_r the reactor diameter and λ the thermal conductivity), E_a is the activation energy, R_g is the gas constant, T is the temperature and $\lambda_{\text{cat,eff}}$ is the effective thermal conductivity (Equation B.8). These parameters are summarized in Table B.1. The values for all criteria are well below their limits of 0.15, 1 and 0.05 for C_M , C_{WP} and both the heat transfer checks, respectively, indicating that no transfer limitations were present during catalysis.

$$C_M = \frac{-r'_{A,\text{mcat(obs)}} R_{\text{cat}}^n}{k_A C_{A,b}} \quad (\text{B.1})$$

$$C_{WP} = \frac{-r'_{A,\text{Vcat(obs)}} \rho_{\text{cat}} R_{\text{cat}}^2}{D_{\text{eff}} C_{A,s}} \quad (\text{B.2})$$

$$Ca \cdot \beta_e \cdot \gamma_b = \frac{-r'_{\text{ethylene}} V_{\text{cat(obs)}}}{a_s k_A C_b} \cdot \frac{-\Delta H \cdot k_A C_b}{h \cdot T_b} \cdot \frac{E_a}{R_g T_b} \quad (\text{B.3})$$

$$\Phi \cdot \beta_i \cdot \gamma_s = \frac{-r'_{\text{ethylene}} V_{\text{cat(obs)}} \left(\frac{n+1}{2}\right)}{a_s^2 \cdot D_{\text{eff}} C_s} \cdot \frac{-\Delta H \cdot D_{\text{eff}} C_s}{\lambda_{\text{cat,eff}} T_s} \cdot \frac{E_a}{R_g T_s} \quad (\text{B.4})$$

$$Sh = \frac{k_A R_{\text{cat}}}{D_{AB}} = 2 + 0.6 \cdot \left(\frac{\rho_f \cdot u_f \cdot R_{\text{cat}}}{\mu_f}\right)^{\frac{1}{2}} \cdot \left(\frac{\mu_f}{\rho_f \cdot D_{AB}}\right)^{\frac{1}{3}} \quad (\text{B.5})$$

$$D_{\text{eff}} = \frac{D_{AB} \cdot \phi_{\text{cat}} \cdot \sigma_{\text{cat}}}{\tau_{\text{cat}}} \quad (\text{B.6})$$

$$Nu = \frac{h_f \cdot d_r}{\lambda_f} \quad (\text{B.7})$$

$$\lambda_{\text{cat,eff}} = \frac{\lambda_{\text{cat}} \cdot \phi_{\text{cat}} \cdot \sigma_{\text{cat}}}{\tau_{\text{cat}}} \quad (\text{B.8})$$



Appendix B

Table B.1 Parameters used in the calculations for internal and external mass and heat transfer limitations.

Parameters	Values
$r'_{\text{ethylene,Vcat(obs)}} \text{ (kmol kg}_{\text{cat}}^{-1} \text{ s}^{-1})$	$3.30 \cdot 10^{-6}$
$C_{\text{ethylene,b}} \text{ (kmol m}^{-3}) = C_{\text{ethylene,s}}$ without external mass transfer limitations	$2.85 \cdot 10^{-3}$
$D_{\text{ethylene in helium}} \text{ (m}^2 \text{ s}^{-1})$	$7.14 \cdot 10^{-5}$
$D_{\text{ethylene,eff}} \text{ (m}^2 \text{ s}^{-1})$	$7.62 \cdot 10^{-6}$
$k_{c,\text{ethylene}} \text{ (m s}^{-1})$	0.207
$r'_{\text{oxygen,mcat(obs)}} \text{ (kmol m}_{\text{cat}}^{-3} \text{ s}^{-1})$	$9.28 \cdot 10^{-7}$
$r'_{\text{oxygen,Vcat(obs)}} \text{ (kmol kg}_{\text{cat}}^{-1} \text{ s}^{-1})$	$2.33 \cdot 10^{-6}$
$C_{\text{oxygen,b}} \text{ (kmol m}^{-3}) = C_{\text{oxygen,s}}$ without external mass transfer limitations	$7.00 \cdot 10^{-4}$
$D_{\text{oxygen in helium}} \text{ (m}^2 \text{ s}^{-1})$	$7.63 \cdot 10^{-5}$
$D_{\text{oxygen,eff}} \text{ (m}^2 \text{ s}^{-1})$	$8.14 \cdot 10^{-6}$
$k_{c,\text{oxygen}} \text{ (m s}^{-1})$	0.222
$E_{a,\text{ethylene combustion}} \text{ (kJ mol}^{-1})^a$	70
$-\Delta H_{\text{ethylene combustion}} \text{ (kJ mol}^{-1})^b$	1411
$R_g \text{ (kJ K}^{-1} \text{ mol}^{-1})$	$8.31 \cdot 10^{-3}$
n	1
$T_b \text{ (K)} = T_s$ without external heat transfer limitations	473.15
$R_{\text{cat}} \text{ (m)}$	$7.5 \cdot 10^{-5}$
$a_s \text{ (m)}$	$4.00 \cdot 10^4$
$\rho_{\text{cat}} \text{ (kg m}^{-3})^c$	399
ϕ_{cat}	0.4
σ_{cat}	0.8
τ_{cat}	3
$\lambda_{\text{cat,eff}} \text{ (kJ m}^{-1} \text{ s}^{-1} \text{ K}^{-1})^c$	30
$\lambda_{\text{cat}} \text{ (kJ m}^{-1} \text{ s}^{-1} \text{ K}^{-1})$	$3.20 \cdot 10^{-3}$
$d_r \text{ (m)}$	$4 \cdot 10^{-3}$
$\rho_i \text{ (kg m}^{-3})^d$	0.1025
$u_i \text{ (m s}^{-1})$	$6.63 \cdot 10^{-3}$
$\mu_i \text{ (Pa s}^{-1})^d$	$1.73 \cdot 10^{-5}$
$\lambda_i \text{ (kJ m}^{-1} \text{ s}^{-1} \text{ K}^{-1})^d$	0.124
$h_i \text{ (kJ m}^{-2} \text{ s}^{-1} \text{ K}^{-1})$	0.113
C_M ethylene	$1.67 \cdot 10^{-7} \ll 0.15$
C_M oxygen	$4.49 \cdot 10^{-7} \ll 0.15$
C_{WP} ethylene	$3.79 \cdot 10^{-5} \ll 1$
C_{WP} oxygen	$1.02 \cdot 10^{-4} \ll 1$
$Ca \cdot \beta_e \cdot \gamma_b$	$7.68 \cdot 10^{-9} \ll 0.05$
$\Phi \cdot \beta_i \cdot \gamma_s$	$6.80 \cdot 10^{-12} \ll 0.05$

^a Ind. Eng. Chem. Res. 2000, 39, 7, 2148–2156

^b NIST chemistry webbook

^c alumina - <https://www.engineeringtoolbox.com/>

^d helium - <https://www.engineeringtoolbox.com/>

Section II – Additional analysis data of α -alumina support materials and catalysts

X-ray diffraction (XRD) was used to analyze the crystal structure of the alumina materials. The diffractograms are given in Figure B.1. For all three types of support material, the diffractograms only show peaks that are representative of α -alumina. The sharpness of the peaks in the diffractograms indicate a high degree of crystallinity and large crystallite sizes for all materials.

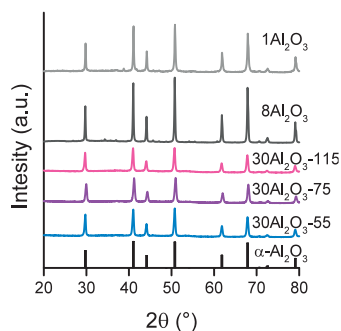


Figure B.1 Diffractograms of $1\text{ m}^2\text{ g}^{-1}$ α -alumina, $8\text{ m}^2\text{ g}^{-1}$ α -alumina and $30\text{ m}^2\text{ g}^{-1}$ α -alumina with varying pore and window sizes. As a reference, the crystal structure of α -alumina (black) is added. The diffractograms are offset for clarity.

Temperature programmed desorption (TPD) of ammonia on the support materials are given Figure B.2. The graphs were deconvoluted in three Gaussian peaks to determine the total graph area. Moreover, as the strength of the acid sites corresponds to the temperature of the ammonia desorption, the deconvoluted peaks show the ratios between the weaker and more strong acid sites.

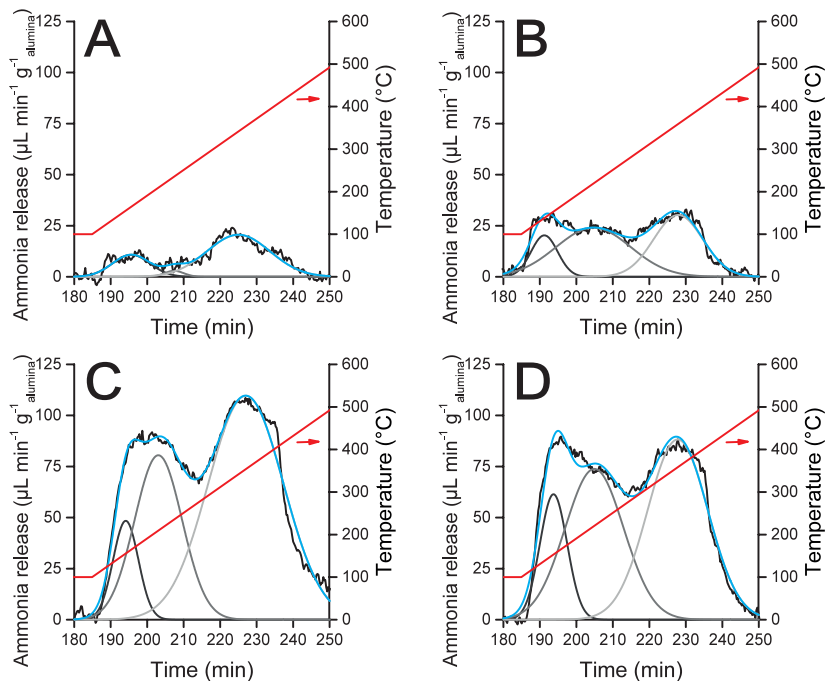


Figure B.2 Amount of ammonia released versus time during NH_3 -TPD measurements on the α -alumina support materials (black lines) and the measurement temperature (red lines). The graphs were fitted (blue lines show total fits) and deconvoluted into three Gaussian peaks (gray lines, dark gray for low temperature, light gray for high temperature).

Diffractiongrams of two materials after the addition of silver particles are given in Figure B.3, where extra peaks at the location of metallic silver are visible. No peaks corresponding to silver oxide were observed.

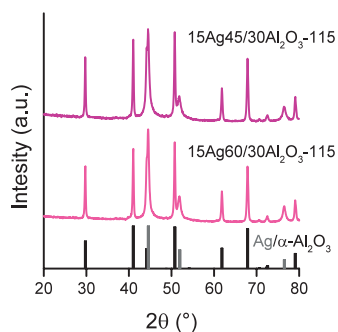


Figure B.3 Diffractiongrams of supported silver catalysts prepared via decomposition in oxygen (15Ag60/30Al₂O₃-115, bottom) or nitrogen (15Ag45/30Al₂O₃-115, top). As a reference, crystal structures of α -alumina (black) and silver (gray) are added. The diffractiongrams are offset for clarity.

Section III - Temperature effect during epoxidation of ethylene

The gas flow rate was varied to tune the ethylene conversion. Additionally, two different reaction temperatures were used, 180 °C and 200 °C. In Figure B.4, the data points obtained at each temperature are given (each data point is an average value of 6 measurements at the same gas flow rate).

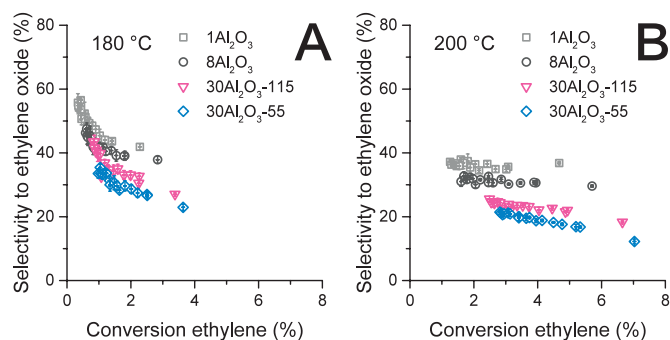


Figure B.4 Selectivity to ethylene oxide versus the ethylene conversion for a selection of catalysts: 15Ag75/1Al₂O₃ (□), 15Ag75/8Al₂O₃ (○), 15Ag70/30Al₂O₃-55 (◇), and 15Ag60/30Al₂O₃-115 (▽). Different conversions were obtained over a range of 350 - 1600 L g_{Ag}⁻¹ h⁻¹ at 180 (A) or 200 °C (B). Standard deviations are indicated with crosses in the data symbols (in Chapter 3, Figure 3.6 they are placed in the background, and hence often hidden behind the symbols).

Section IV - Stability catalysts in epoxidation of ethylene

The total run time of each catalytic test was circa 120 h. Figure B.5 shows the size distribution before and after catalysis of the silver on different support materials. At every temperature (180, 190 and 200 °C), the same gas flow rate was used twice, with an interval of 10 hours. In Figure B.6, the conversions at the gas flow rate of 350 L g_{Ag}⁻¹ h⁻¹ are given versus the time on stream. After the conditioning step at 270 °C, no deactivation is observed.

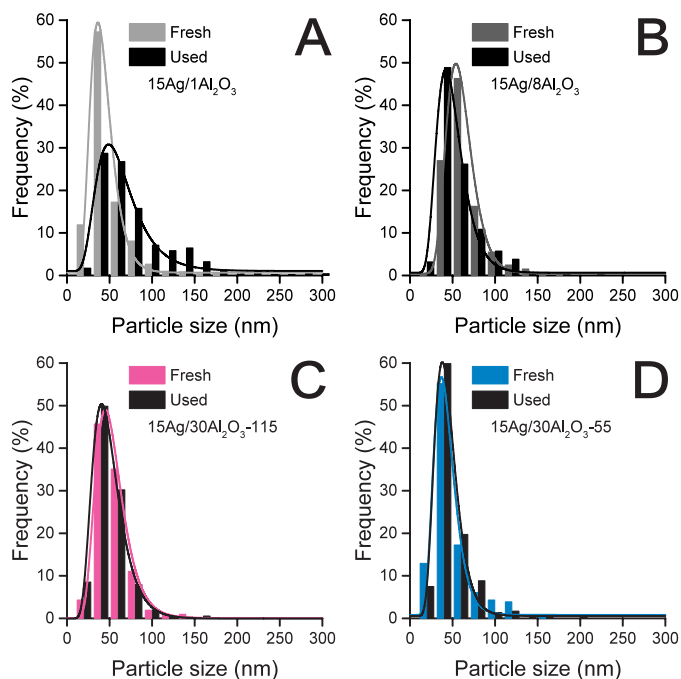


Figure B.5 Particle size distributions before and after catalysis of the catalysts for which the average particle sizes are given in Table 3.2 (Chapter 3).

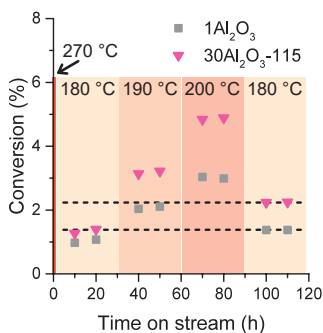


Figure B.6 Conversion of ethylene in the epoxidation of ethylene versus the time on stream of 15Ag75/1Al₂O₃ (■) and 15Ag70/30Al₂O₃-115 (▼), using a gas flow rate of 350 L g_{Ag}⁻¹ h⁻¹.

Additionally, isothermal catalytic runs were performed using the 15 wt% silver on $1 \text{ m}^2 \text{ g}^{-1}$ α -alumina catalyst ($15\text{Ag}75/1\text{Al}_2\text{O}_3$). These runs were carried out at either $230 \text{ }^\circ\text{C}$ or at $250 \text{ }^\circ\text{C}$, with a constant gas flow rate of $350 \text{ L g}_{\text{Ag}}^{-1} \text{ h}^{-1}$ to follow the activity of the catalyst over time. The conversion of ethylene versus the time on stream is shown in Figure B.7. Figure B.8 shows the particle size distribution and surface-averaged particle size of the supported silver particles before and after these catalytic runs.

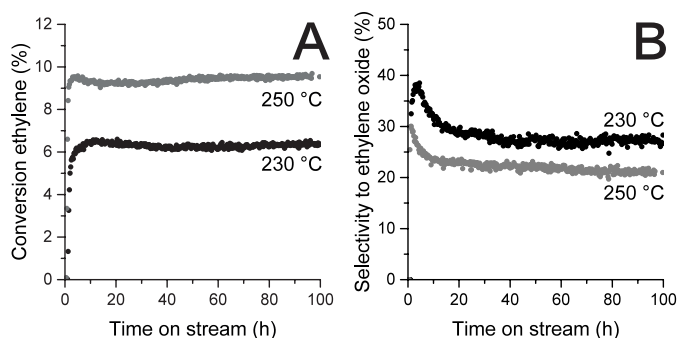


Figure B.7 Conversion of ethylene (A) or selectivity to ethylene oxide (B) versus time on stream of $15\text{Ag}75/1\text{Al}_2\text{O}_3$ catalyst in the epoxidation of ethylene at $230 \text{ }^\circ\text{C}$ (gray dots) or at $250 \text{ }^\circ\text{C}$ (black dots) using a constant gas flow rate of $350 \text{ L g}_{\text{Ag}}^{-1} \text{ h}^{-1}$.

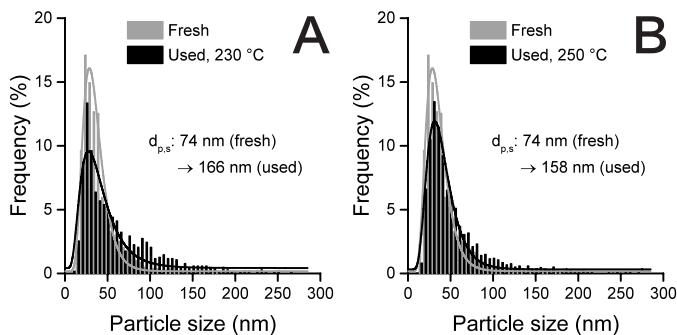


Figure B.8 Particle size distributions of $15\text{Ag}75/1\text{Al}_2\text{O}_3$ catalyst before (fresh, gray) and after being used (black) in the epoxidation of ethylene at $230 \text{ }^\circ\text{C}$ (A) or at $250 \text{ }^\circ\text{C}$ (B) for 100 h using a gas flow rate of $350 \text{ L g}_{\text{Ag}}^{-1} \text{ h}^{-1}$.

Appendix C - Supporting information Chapter 4

Section I - Additional analysis on the silica support material

The surface area and pore size distribution of the prepared SBA-15, the silica support material, was measured using nitrogen physisorption. Figure C.1 shows the adsorption and desorption isotherms in Frame A. The area below 0.1 relative pressure indicates the presence of micropores, and the hysteresis between the adsorption and desorption branch around 0.7-0.8 relative pressure indicates a large number of mesopores. Frame B shows the narrow size distribution of the pores, with a diameter of 6.8 nm.

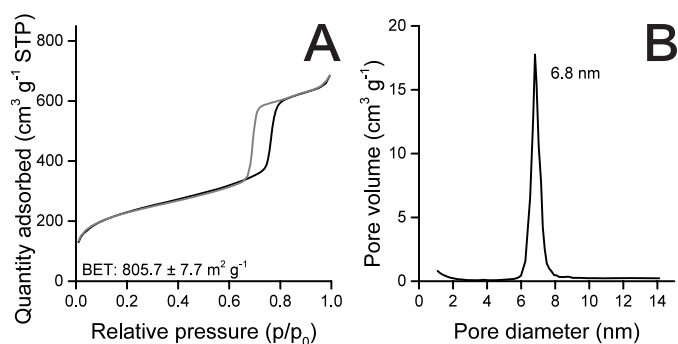


Figure C.1 Nitrogen physisorption isotherms of pristine SBA-15 (A), with adsorption in black and desorption in gray and the pore diameter distribution (B) calculated using the BHJ analysis on the desorption data.

C

Section II – Additional analysis on the silver nitrate-containing composites

The physical mixture of SBA-15 and silver nitrate was analyzed using X-ray diffraction (XRD). Figure C.2 shows diffractograms of the physical mixture before (Frame A) and after melt infiltration at 250 °C (Frame B). Before heating, only sharp peaks corresponding to silver nitrate in the orthorhombic phase can be observed, except for the broad peak around 27 ° corresponding to amorphous silica. After melt infiltration, these orthorhombic silver nitrate peaks were no longer observed. Instead, all sharp peaks correspond to silver nitrate in the rhombohedral phase. As a reference, diffractograms of silver nitrate without any silica present before and after heating to 250 °C are shown in Figure C.3. This time, no phase transition was observed, and the silver nitrate stayed in the orthorhombic phase.

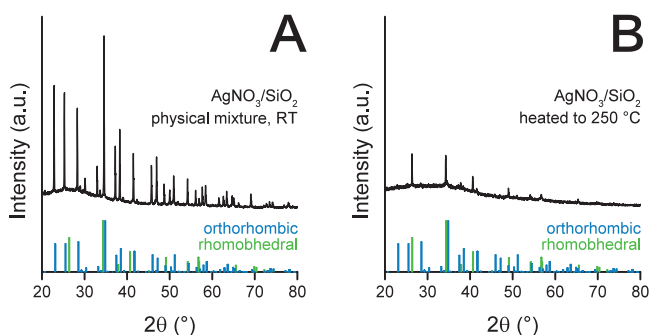


Figure C.2 Diffractograms of physical mixture of silver nitrate and SBA-15 before (A) and after heating (B). Diffractogram patterns of silver nitrate are shown in blue (orthorhombic phase) and green (rhombohedral phase).

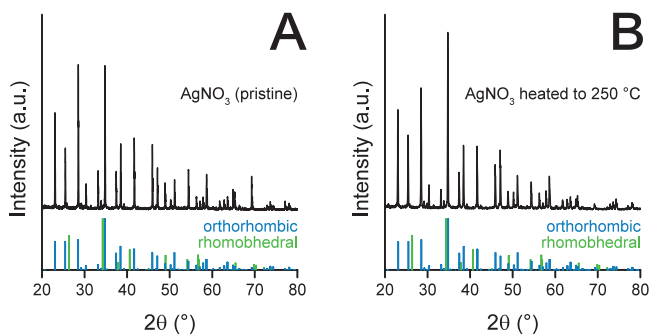


Figure C.3 Diffractograms of silver nitrate before (A) and after being heated to 250 °C (B). Diffractogram patterns of silver nitrate are shown in blue (orthorhombic phase) and green (rhombohedral phase). No peaks of silver nitrate in the rhombohedral phase are visible.

Section III - Calculation of the melting point depression

The expected melting point depression (ΔT) was calculated using the Gibbs-Thomson equation (Equation C.1) [230]. In this formula, the melting point of the silver nitrate inside the pores ($T_m(r)$) was correlated to the pore radius (r), the macrocrystalline melting temperature (T_0), the surface tension between the silica wall and solid silver nitrate (γ_{WS}) and the silica wall and liquid silver nitrate (γ_{WL}), the molar volume (v_1) and the molar enthalpy (heat) of fusion (ΔH_f).

$$\Delta T = T_0 - T_m(r) = \frac{2T_0(\gamma_{WS} - \gamma_{WL})v_1}{\Delta H_f r} \quad (\text{C.1})$$

The formula can be rewritten using Young's equation (Equation C.2). In this equation, γ_{SL} is the interfacial tension between liquid and solid silver nitrate, and θ is the contact angle between the silver nitrate and the wall.

$$\gamma_{WS} - \gamma_{WL} = \gamma_{SL} \cos \theta \quad (\text{C.2})$$

Despite that this angle is unknown, wetting can be assumed, since the silver nitrate enters the pores. By assuming complete wetting, $\theta = 0$, the maximum expected melting point depression is calculated. In doing so, Equation C.1 can be rewritten as Equation C.3.

$$\Delta T = T_0 - T_m(r) = \frac{2T_0 \gamma_{SL} v_1}{\Delta H_f r} \quad (\text{C.3})$$

The empirical formula proposed by Bertozzi and Sternheim (Equation C.4) was used to calculate the surface tension [267].

$$\gamma_{SL} = 163.7 - 0.066T \quad (\text{C.4})$$

In this formula, the temperature is in °C, and the surface tension in mN m⁻¹. By using $T = 148$ °C, a surface tension of 153.9 mN m⁻¹ was obtained. Combining this with the pore diameter of 6.8 nm, a ΔT of 71 °C was found, which is very close to the melting point depression observed in the experiments described in Chapter 4.

Section IV – Additional analysis on Ag/SBA-15 composites

Upon thermal decomposition, silver nitrate decomposes, and metallic silver forms. In the presence of silica, next to metallic silver, also silver silicate may form. Figure C.4 shows diffractograms of melt infiltrated composites containing silver nitrate and SBA-15, after being heating in an inert atmosphere to 425 °C *ex situ* (Frame A) and to 500 °C during *in situ* XRD measurements (Frame B). Both samples contain metallic silver and silver silicate ($\text{Ag}_{10}\text{Si}_4\text{O}_{13}$).

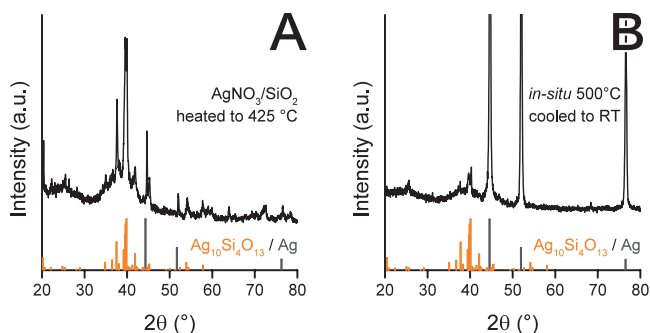


Figure C.4 Diffractograms of melt infiltrated $\text{AgNO}_3/\text{SBA-15}$ composites after thermal decomposition. Decomposition *ex situ* at 425 °C (A) and composite at room temperature after decomposition during *in situ* high temperature XRD measurements (B, same material as shown in Figure 4.3, Frame A). Diffraction patterns of metallic silver are shown in gray and of silver silicate ($\text{Ag}_{10}\text{Si}_4\text{O}_{13}$) in orange.

Diffuse-Reflectance Ultraviolet/Visible (DR UV/Vis) spectroscopy was used to analyze the catalysts. Surface plasmon resonance of the silver nanoparticles results in absorption visible in Figure C.5. The very similar adsorption behavior of the two catalysts containing nanowires (Ag/SBA-15_1 and $\text{Ag/SBA-15}_{0.1}$) further shows how similar these catalysts are. The lower intensity of the other material, $\text{Ag/SBA-15}_{\text{N}_2}$, indicates the presence of smaller, or much larger silver particles, as these exhibit less intense surface plasmon resonance.

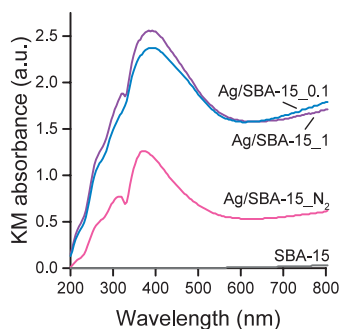


Figure C.5 DR UV/Vis spectra of pristine SBA-15 (gray line), Ag/SBA-15_1 (purple line), $\text{Ag/SBA-15}_{0.1}$ (blue line) and $\text{Ag/SBA-15}_{\text{N}_2}$ (pink line).

Using XRD analysis, the silver crystallite sizes of the silver in and outside the pores of the SBA-15 were determined. Figure C.6 shows the measured diffractograms of the three catalysts. Each peak corresponding to silver was deconvoluted into two separate peaks, one for large crystallites and one for small crystallites by using TOPAS V5 software. The convoluted peaks are presented in Chapter 4, Figure 4.5, while the sum of these convoluted peaks is given in Figure C.6 in blue, and the difference with the experimental data is shown in gray.

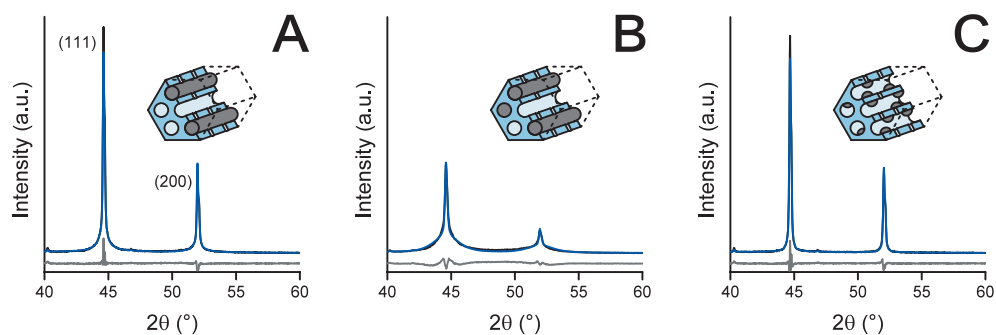


Figure C.6 Diffractograms (black lines) of Ag/SBA-15 composites after decomposition in 10% hydrogen in nitrogen at 130 °C with a heating ramp of 1 °C min⁻¹ (A) or 0.1 °C min⁻¹ (B), or when heating in nitrogen and starting the reduction at 250 °C (C), the total fit obtained via TOPAS V5 software (blue lines) and the difference between the experimental data and the fit (gray lines).

Section V – Additional catalytic data on cinnamaldehyde hydrogenation

Figure C.7 shows the catalytic results from control experiments. Without any catalyst (Frame A), or with only SBA-15 present (Frame B), no conversion of cinnamaldehyde was observed. When the test was started with catalyst present (Frame C), cinnamaldehyde was converted, but this conversion stopped after the catalyst was removed.

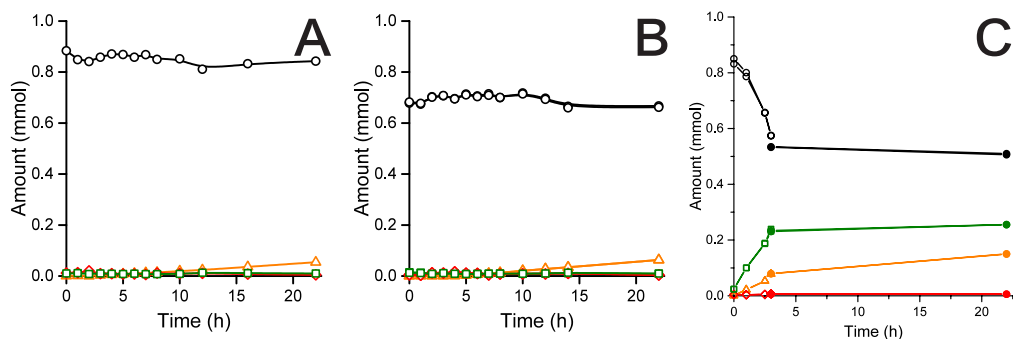


Figure C.7 The amounts of cinnamaldehyde (○) and of the formed products, cinnamyl alcohol (□), hydrocinnamaldehyde (△) and hydrocinnamyl alcohol (◇) present in the reaction mixture during control experiments. The reaction was performed without catalyst (A), with pristine support without silver (B) and with catalyst present during the first 3 hours of the reaction only (C, open symbols), whereupon the catalyst was removed by hot filtration and the reaction was continued without the catalyst present (closed symbols).

Figure C.8, Frame A, shows the catalytic results of a reference catalyst prepared via impregnation and drying. While the reference catalyst showed good activity and selectivity for the hydrogenation of cinnamaldehyde, transmission electron microscopy (TEM) images (Frames B and C) show that the silver nanoparticles grew significantly in size. After catalysis, the silver particles are the same size as the SBA-15 pore diameter. Therefore, the size of these pores probably restricted further growth of the silver.

The conversion of cinnamaldehyde versus the selectivity towards the desired product, cinnamyl alcohol, is given in Figure C.9. The selectivity is highest for the reference catalyst and Ag/SBA-15_0.1, followed by Ag/SBA-15_0.1 and finally Ag/SBA-15_N₂. Figure C.10 shows transmission electron microscopy (TEM) images of the used catalysts, which showed that the catalysts with the silver nanowires (Frames A and B) were more stable than the catalyst with the silver nanoparticles (Frame C). The small silver nanoparticles grew in size, just as was the case of the reference catalyst.

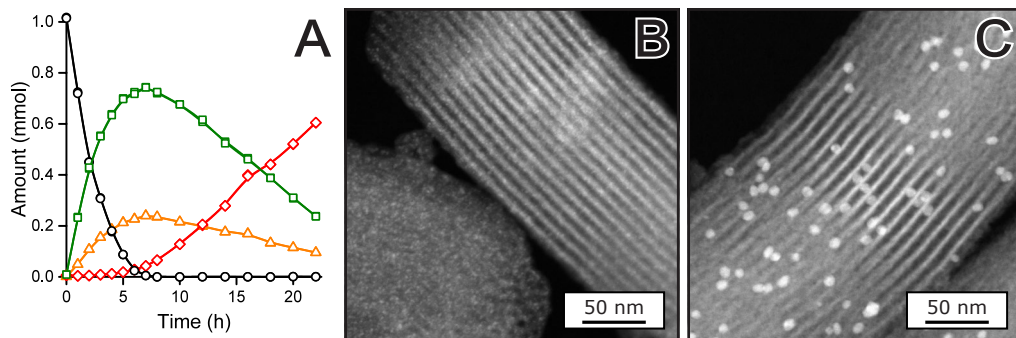


Figure C.8 Catalytic performance of 15 wt% Ag/SBA-15 synthesized via impregnation and drying (A) and TEM images of the fresh catalyst (B) and of the used catalyst (C). Amount of cinnamaldehyde (○) and products, cinnamyl alcohol (□), hydrocinnamaldehyde (△) and hydrocinnamyl alcohol (◇) versus time in the hydrogenation of cinnamaldehyde. Conditions: Cinnamaldehyde (1 mmol), catalyst (280 mg 15 wt% Ag/SiO₂, cinnamaldehyde to Ag mole ratio is 2.6), isopropanol (1 mL), water (1 mL), tetradecane (100 μL), hydrogen (40 bar), at 70 °C, 900 rpm stirring.

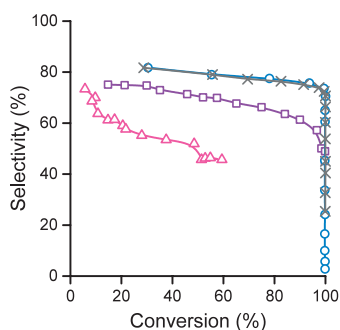


Figure C.9 Selectivity towards cinnamyl alcohol versus conversion of cinnamaldehyde over supported silver catalysts, Ag/SBA-15_1 (□), Ag/SBA-15_0.1 (○), Ag/SBA-15_N₂ (△) and 15Ag/SBA-15_ref (×) in the hydrogenation of cinnamaldehyde.

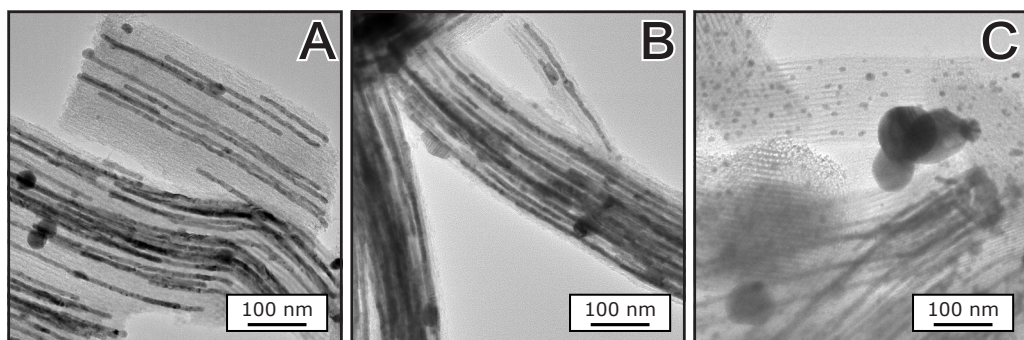


Figure C.10 TEM images of used catalysts after hydrogenation of cinnamaldehyde, Ag/SBA-15_1 (A), Ag/SBA-15_0.1 (B), Ag/SBA-15_N₂ (C).

Appendix D - Supporting information Chapter 5

Section I – Silver particle and crystallite size and size distributions

Using transmission electron microscopy (TEM), the sizes of silver particles were measured. The particle size distributions of the measured sizes are given in 1. No significantly larger silver particles were observed than the ones shown in the TEM images given in the main text.

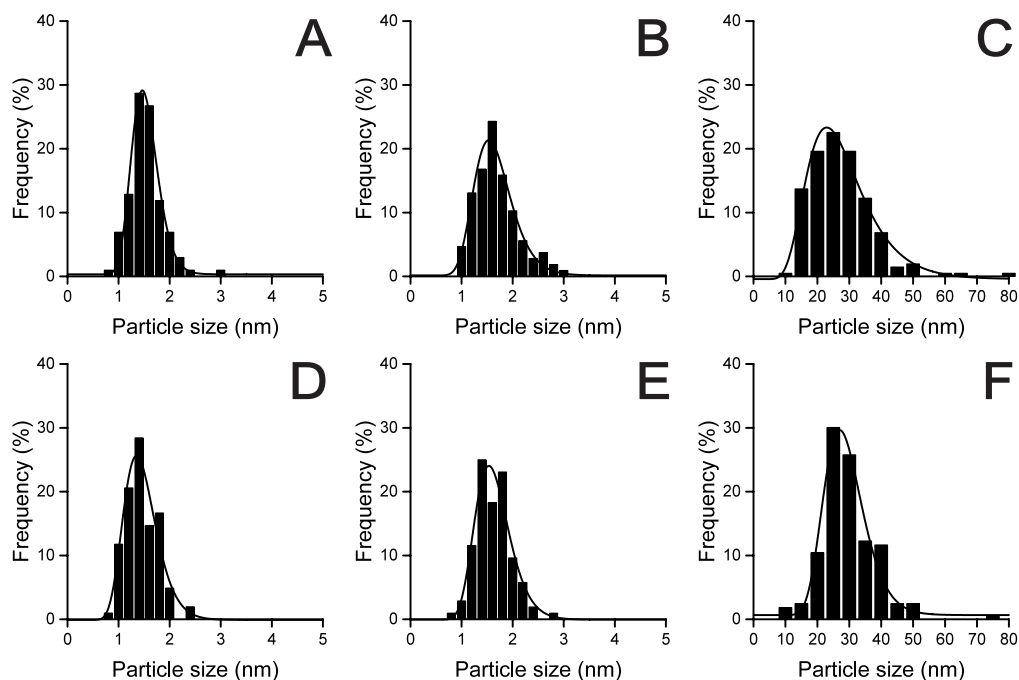


Figure D.1 Particle size distributions of supported silver particles prepared via reduction of silver silicate in 1% hydrogen in nitrogen (A), 1% carbon monoxide in nitrogen (B) or via direct reduction of silver nitrate in 1% hydrogen in nitrogen (C). (D) show distribution of additional consecutive treatments in oxygen and 1% carbon monoxide in nitrogen of (B), and (E) and (F) show the distributions of the silver of (B) and (C), respectively, after being used in catalysis.

The surface-averaged particle sizes ($d_{p,s}$) and the standard deviations in the width of the particle size distribution ($\sigma_{p,s}$) were calculated using the following Equation D.1, with n the number of silver particles counted, and d_i the size of particle i .

$$d_{p,s} \pm \sigma_{p,s} = \frac{\sum_{i=1}^n d_i^3}{\sum_{i=1}^n d_i^2} \pm \sqrt{\frac{1}{n} \cdot \sum_{i=1}^n (d_{p,s} - d_i)^2} \quad (\text{D.1})$$

D

The supported silver particles were analyzed using X-ray diffraction (XRD). Figure D.2 shows the diffractograms and the obtained fits, calculated using TOPAS V5 software. These fits were used to calculate the crystallite size of the silver nanoparticles. The absence of sharp and intense peaks at the silver peak positions in the diffractograms in Frame A confirm that no large silver particles were formed for the silver particles prepared via the formation of silver silicate.

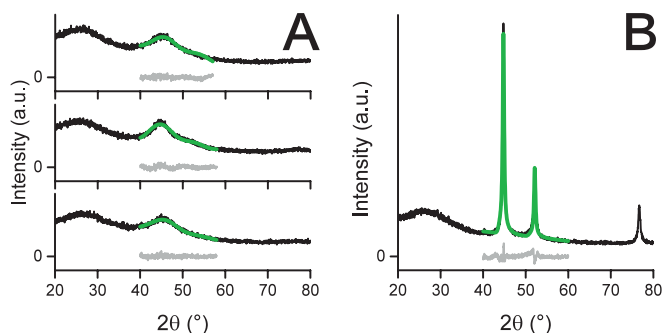


Figure D.2 Diffractograms of supported silver nanoparticles (black lines), the fit obtained via TOPAS V5 software (green lines) and the difference between the measured diffractogram and the fit (gray lines). Supported silver nanoparticles obtained via silver silicate, reduced in 1% hydrogen in nitrogen (A, bottom graph), reduced in 1% carbon monoxide in nitrogen (A, middle graph) and this last material after consecutive treatments in oxygen and in 1% carbon monoxide in nitrogen (A, top graph), and supported silver nanoparticles obtained via direct reduction of silver nitrate (B).

Section II – Determination of conversion levels, reaction orders, activation energies and turnover frequencies during carbon monoxide oxidation

The reaction orders of the catalysts were determined via plotting the partial pressure of the reactants versus the activity of the catalyst, as shown in Figure D.3. The concentration of oxygen or carbon monoxide was varied between 0.5 and 1.5%, while keeping the concentration of the other reactant at 1%.

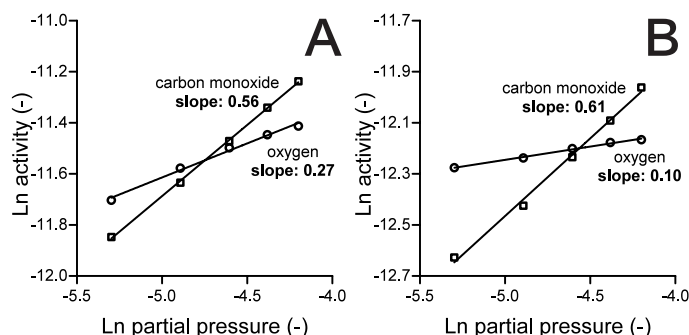


Figure D.3 Reaction rate orders of supported silver nanoparticles prepared via silver silicate utilization (A) or via the direct reduction of silver nitrate (B) in carbon monoxide oxidation, using 25 mg catalyst, a reaction temperature of 50 °C and a gas flow rate of 640 L g_{Ag}⁻¹ h⁻¹. The activity is given in mol_{CO,converted} s⁻¹ g_{Ag}⁻¹ and the conversion levels lied between 5–20%.

The activation energies of the catalysts were determined by plotting the reaction temperatures versus the reaction rate constants, as shown in Figure D.4. The reaction rate constants were derived using the reaction orders determined in Figure D.3.

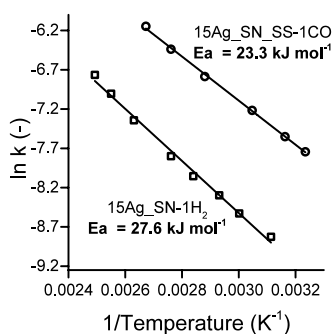


Figure D.4 Reaction rate constants versus the reaction temperature to calculate the activation energies of supported silver nanoparticles prepared via silver silicate utilization (circles) or via the direct reduction of silver nitrate (squares) in carbon monoxide oxidation. 25 mg catalyst and a gas flow rate of 640 L g_{Ag}⁻¹ h⁻¹ was used. Conversion levels up to 50% were taken into account and the activity used for the determination of k was in mol_{CO,converted} s⁻¹ g_{Ag}⁻¹.

Section III – Characteristics silver silicate

Using XRD, the crystal structure of the orange powder obtained after heating the impregnated SBA-15 to 400 °C was determined. In Figures D.5 and D.6, measured diffractograms are set against known diffraction patterns of silver, silver oxide and silver silicate.

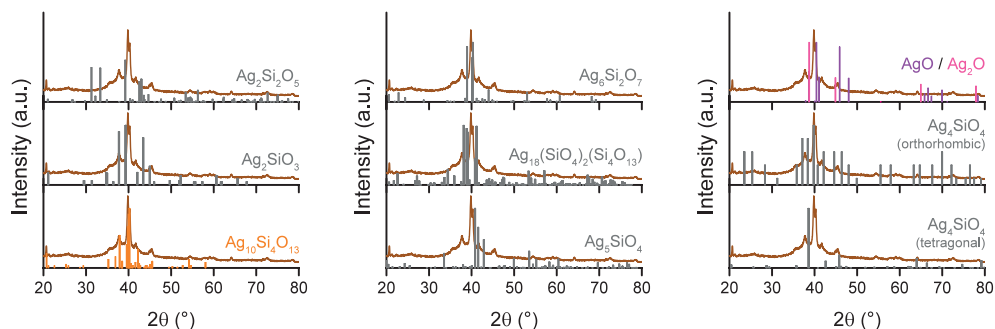


Figure D.5 Diffractograms of silver-containing material set against the diffraction patterns of silver oxides and silver silicates with Ag : Si ratio of 1–5.

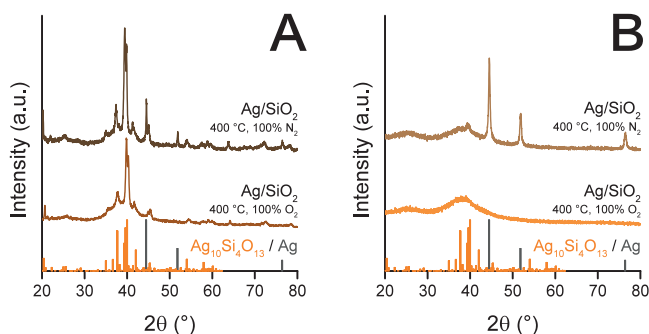


Figure D.6 Diffractograms of silver silicate formed in the presence of nitrogen or oxygen with a silver loading of 55 wt% (A) or 35 wt% (B). In the presence of nitrogen, both silver silicate and metallic silver formed, while under an oxygen atmosphere only silver silicate had formed. As a reference, crystal structures of silver silicate (orange) and silver (gray) are added. The diffractograms are offset for clarity.

The pore structure of the silver silicate was investigated using TEM. Figure D.7 shows TEM images of silver silicate with a silver loading of 35 wt% and 55 wt%. These images were obtained via cooling the TEM sample holder with liquid nitrogen to stabilize the silver silicate structure under the electron beam. Without cooling, silver silicate decomposed instantly when exposed to the electron beam.

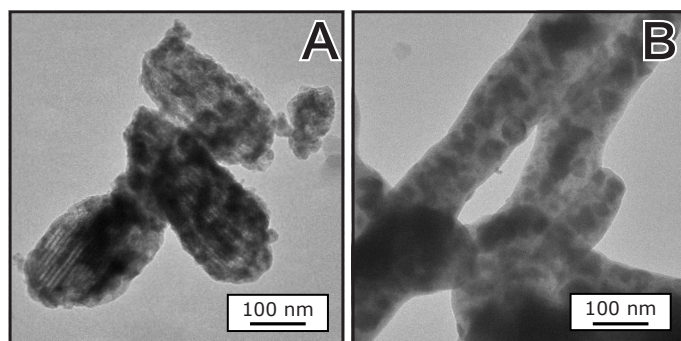


Figure D.7 TEM images of silver silicate with a silver loading of 35 wt% (A) or 55 wt% (B). While some of the original pore structure of SBA-15 was still present in the material containing 35 wt% silver, the pore structure was completely gone for the 55 wt% silver material.

Section IV – TGA-MS of silver-containing materials

Using thermal gravimetric analysis (TGA), the decomposition temperatures of the used and formed silver precursors were investigated. The decomposition products were identified using mass spectroscopy (MS). The MS signals of NO_x products upon decomposition of silver silicate are shown in Figure D.8. Figure D.9 shows the weight loss as a result of silver nitrate decomposition in argon and the corresponding NO_x decomposition products.

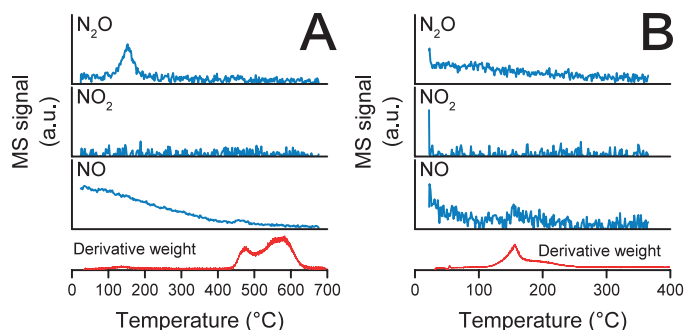


Figure D.8 The MS signals of nitrous oxide, nitrogen dioxide and nitric oxide (blue lines) and the derivative of the weight (red lines) of the silver silicate (circa 55 wt% Ag) during a TGA-MS measurement to 700 °C in argon (A) or to 400 °C in 5% hydrogen in argon (B).

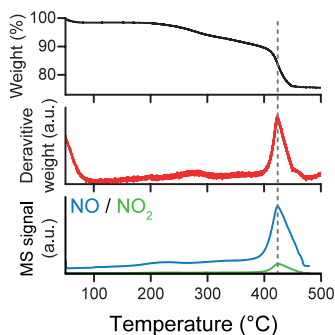


Figure D.9 Decomposition of silver nitrate on SBA-15 in argon followed using TGA-MS. The weight loss (top) and the derivative of the weight loss (middle) indicate the decomposition of silver nitrate starting around 400 °C in a 10 mL min^{-1} argon flow. The MS signal shows the formation of the decomposition products nitric oxide (bottom, blue line) and nitrogen dioxide (bottom, green line) at the same temperature.

Section V – Characteristics silver on silica materials

Figure D.10 shows TEM images of 55 wt% and 35 wt% silver on silica materials in Frames A and B, respectively, obtained via reduction of the silver silicate materials. Frame C shows the pore size distributions of the materials before (solid line) and after reduction (dotted line). Upon reduction of the silver silicate, no large changes in pore volume were detected.

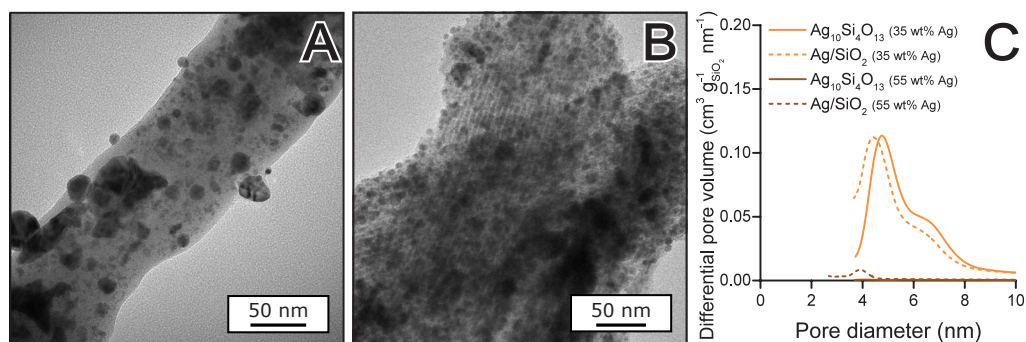


Figure D.10 TEM images of silver on silica with 55 wt% Ag (A) and 35 wt% Ag (B) after reduction of silver silicate materials in a 10% hydrogen in nitrogen flow and the pore size distributions of silver silicate (solid lines) and silver on silica (dashed lines) materials, obtained using nitrogen physisorption (desorption, C).

Section VI – Additional carbon monoxide oxidation measurements

All catalysts were tested at two different gas flow rates. First, the catalysts were heated twice to 200 °C (heating ramp of 1 °C min⁻¹) using a gas flow rate of 320 L g_{Ag}⁻¹ h⁻¹, whereupon the catalysts were heated for another two cycles using a gas flow rate of 640 L g_{Ag}⁻¹ h⁻¹. The catalytic performance of 15Ag_SN_SS-1CO or 15Ag_SN-1H₂ during the first two cycles is given in the main text, the catalytic performance during the last two cycles is given in Figure D.11.

During the catalytic runs, heating or cooling ramps of the catalysts was 1 °C min⁻¹ were used. For the catalyst prepared via silver silicate, this led to a difference in activity during heating and cooling. In Figure D.12, the catalytic activity of supported silver particles prepared via silver silicate utilization was first measured using the same heating ramp as in the main text and afterward the catalyst was heated stepwise. For this catalyst, the silver silicate was reduced *ex situ* using a flow of 1% carbon monoxide in nitrogen at 150 °C.

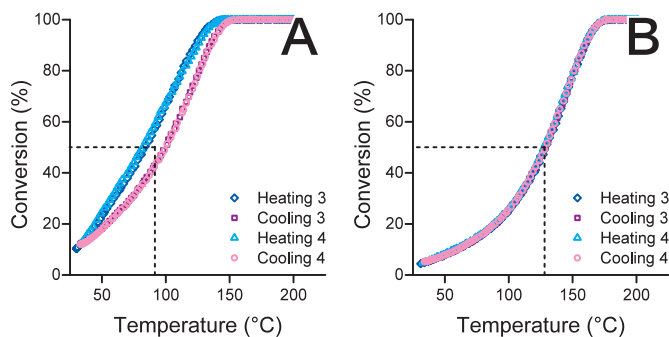


Figure D.11 Catalytic performance of 15Ag_SN_SS-1CO (A) or 15Ag_SN-1H₂ (B). Conversion of carbon monoxide versus reaction temperature, using 25 mg catalyst and a gas flow rate of 640 L g_{Ag}⁻¹ h⁻¹.

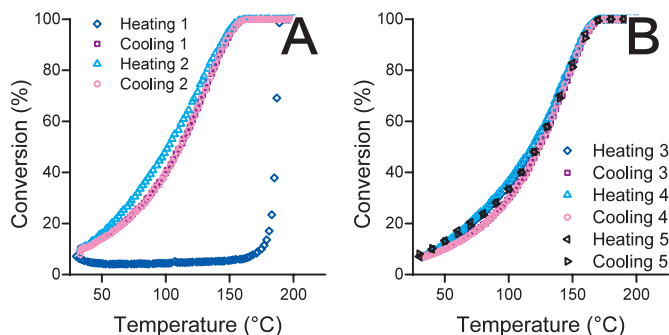


Figure D.12 Conversion of carbon monoxide versus reaction temperature, using 25 mg catalyst a gas flow rate of 320 L g_{Ag}⁻¹ h⁻¹ (A) or 640 L g_{Ag}⁻¹ h⁻¹ (B). For the first four heating and cooling cycles, the heating/cooling ramp was 1 °C min⁻¹, whereas for the fifth heating and cooling cycle, the reaction temperature was heated stepwise. For the stepwise heating and cooling cycle, the average conversion levels of the last 30 min at each temperature are given.



References

1. I. Chorkendorff, J.W. Niemantsverdriet, 'Concepts of modern catalysis and kinetics', 2nd edition, Wiley-VCH Verlag GmbH & Co. KGaA, 2007
2. K.P. de Jong, 'Synthesis of Solid Catalysts', 1st edition, Wiley-VCH Verlag GmbH & Co. KGaA, 2009
3. T.E. Lefort, 'Process for the production of ethylene oxide', US1998878A, 1–2, 1931
4. M. Mitsuhashi, F. Watanabe, T. Kumazawa, F. Watanabe, T. Kumazawa, 'Silver catalyst for production of ethylene oxide', 218700, 1–6, 1983
5. M.O. Özbek, I. Onal, R.A. Van Santen, 'Why silver is the unique catalyst for ethylene epoxidation', *Journal of Catalysis*, **284**, 230–235, 2011
6. T. Pu, H. Tian, M.E. Ford, S. Rangarajan, I.E. Wachs, 'Overview of selective oxidation of ethylene to ethylene oxide by Ag catalysts', *ACS Catalysis*, **9**, 10727–10750, 2019
7. L.G. Pinaeva, A.S. Noskov, 'Prospects for the development of ethylene oxide production catalysts and processes', *Petroleum Chemistry*, **60**, 1191–1206, 2020
8. TechNavio, 'Global ethylene oxide and ethylene glycol market 2016–2020', 2016
9. H. van Milligen, B. VanderWilp, G.J. Wells, 'Enhancements in ethylene oxide/ethylene glycol manufacturing technology', 2020
10. 'Global and China ethylene oxide (EO) industry report 2017-2021', 2017
11. P.A. Kilty, W.M.H. Sachtler, 'The mechanism of the selective oxidation of ethylene to ethylene oxide', *Catal Rev Sci Eng*, **10**, 1–16, 1974
12. S. Rebsdat, D. Mayer, 'Ethylene oxide', *Encyclopedia of industrial chemistry*, **13**, 547–572, 2001
13. M.O. Özbek, R.A. van Santen, 'The mechanism of ethylene epoxidation catalysis', *Catalysis Letters*, **143**, 131–141, 2013
14. O.O. Bernardini, E.A. Cherniak, 'Heterogeneous isomerization of ethylene oxide to acetaldehyde', *Canadian Journal of Chemistry*, **51**, 1371–1377, 1973
15. Y. Hui-Xing, C. Hua, H. De-Gang, 'The rate constant determination for the isomerization of ethylene oxide to acetaldehyde by chemical shock tube', *Acta Chimica Sinica*, 941–946, 1989
16. J.K. Lee, X.E. Verykios, R. Pitchai, 'Support participation in chemistry of ethylene oxidation on silver catalysts', *Applied Catalysis*, **44**, 223–237, 1988
17. I.E. Wachs, R.J. Madix, 'The oxidation of methanol on a silver (110) catalyst', *Surface Science*, **76**, 531–558, 1978
18. S. Kyuogo Yoshikawa, Y. Tadahiro Matsuzawa, 'Process for producing aqueous formaldehyde solution', 4594457, 1986
19. G.J. Millar, M. Collins, 'Industrial production of formaldehyde using polycrystalline silver catalyst', *Industrial and Engineering Chemistry Research*, **56**, 9247–9265, 2017
20. L. Pilato, 'Phenolic resins: a century of progress', Springer, 2010
21. O. V. Vodyankina, G. V. Mamontov, V. V. Dutov, T.S. Kharlamova, M.A. Salaev, 'Ag-containing nanomaterials in heterogeneous catalysis: Advances and recent trends', in *Advanced nanomaterials for catalysis and energy: synthesis, characterization and applications*, 143–175, Elsevier Inc., 2018

References

22. G. Liao, J. Fang, Q. Li, S. Li, Z. Xu, B. Fang, 'Ag-based nanocomposites: Synthesis and applications in catalysis', *Nanoscale*, **11**, 7062–7096, 2019
23. X. Zhang, Z. Qu, F. Yu, Y. Wang, 'Progress in carbon monoxide oxidation over nanosized Ag catalysts', *Chinese Journal of Catalysis*, **34**, 1277–1290, 2013
24. S. Dey, G.C. Dhal, 'Applications of silver nanocatalysts for low-temperature oxidation of carbon monoxide', *Inorganic Chemistry Communications*, **110**, 107614, 2019
25. V. V. Torbina, A.A. Vodyankin, S. Ten, G. V. Mamontov, M.A. Salaev, V.I. Sobolev, O. V. Vodyankina, 'Ag-based catalysts in heterogeneous selective oxidation of alcohols: A review', *Catalysts*, **8**, 2018
26. X.Y. Dong, Z.W. Gao, K.F. Yang, W.Q. Zhang, L.W. Xu, 'Nanosilver as a new generation of silver catalysts in organic transformations for efficient synthesis of fine chemicals', *Catalysis Science and Technology*, **5**, 2554–2574, 2015
27. K. Shimizu, K. Sawabe, A. Satsuma, 'Unique catalytic features of Ag nanoclusters for selective NO_x reduction and green chemical reactions', *Catalysis Science and Technology*, **1**, 331–341, 2011
28. J.P.A. Neeft, M. Makkee, J.A. Moulijn, 'Catalysts for the oxidation of soot from diesel exhaust gases. I. An exploratory study', *Applied Catalysis B: Environmental*, **8**, 57–78, 1996
29. E. Aneggi, J. Llorca, C. de Leitenburg, G. Dolcetti, A. Trovarelli, 'Soot combustion over silver-supported catalysts', *Applied Catalysis B: Environmental*, **91**, 489–498, 2009
30. K. ichi Shimizu, Y. Miyamoto, A. Satsuma, 'Size- and support-dependent silver cluster catalysis for chemoselective hydrogenation of nitroaromatics', *Journal of Catalysis*, **270**, 86–94, 2010
31. P. Claus, H. Hofmeister, 'Electron microscopy and catalytic study of silver catalysts: Structure sensitivity of the hydrogenation of crotonaldehyde', *The Journal of Physical Chemistry B*, **103**, 2766–2775, 1999
32. P. Gallezot, D. Richard, 'Selective hydrogenation of α,β -unsaturated aldehydes', *Catalysis Reviews - Science and Engineering*, **40**, 81–126, 1998
33. P. Claus, 'Selective hydrogenation of α,β -unsaturated aldehydes and other C=O and C=C bonds containing compounds', *Topics in Catalysis*, **5**, 51–62, 1998
34. Y. Yuan, S. Yao, M. Wang, S. Lou, N. Yan, 'Recent progress in chemoselective hydrogenation of α,β -unsaturated aldehyde to unsaturated alcohol over nanomaterials', *Current Organic Chemistry*, **17**, 400–413, 2013
35. K. Wang, B. Yang, 'Theoretical understanding on the selectivity of acrolein hydrogenation over silver surfaces: The non-Horiuti-Polanyi mechanism is the key', *Catal. Sci. Technol.*, **7**, 4024–4033, 2017
36. D. Sun, X. Xu, Y. Qin, S.P. Jiang, Z. Shao, 'Rational Design of Ag-Based Catalysts for the Electrochemical CO₂ Reduction to CO: A Review', *ChemSusChem*, **13**, 39–58, 2020
37. S.A. Mahyoub, F.A. Qaraah, C. Chen, F. Zhang, S. Yan, Z. Cheng, 'An overview on the recent developments of Ag-based electrodes in the electrochemical reduction of CO₂ to CO', *Sustainable Energy and Fuels*, **4**, 50–67, 2019
38. Q. Lu, F. Jiao, 'Electrochemical CO₂ reduction: Electrocatalyst, reaction mechanism, and process engineering', *Nano Energy*, **29**, 439–456, 2016
39. Q. Lu, J. Rosen, Y. Zhou, G.S. Hutchings, Y.C. Kimmel, J.G. Chen, F. Jiao, 'A selective and efficient electrocatalyst for carbon dioxide reduction', *Nature Communications*, **5**, 1–6, 2014

40. W. Hou, S.B. Cronin, 'A review of surface plasmon resonance-enhanced photocatalysis', *Advanced Functional Materials*, **23**, 1612–1619, 2013
41. S. Sarina, E.R. Waclawik, H. Zhu, 'Photocatalysis on supported gold and silver nanoparticles under ultraviolet and visible light irradiation', *Green Chemistry*, **15**, 1814–1833, 2013
42. C.R. Henry, 'Surface studies of supported model catalysts', *Surface Science Reports*, **31**, 231–233, 235–325, 1998
43. R.A. van Santen, 'Insensitive catalytic relationships', *Accounts of Chemical Research*, **42**, 57–66, 2009
44. J.P. den Breejen, P.B. Radstake, G.L. Bezemer, J.H. Bitter, V. Frøseth, A. Holmen, K.P. de Jong, 'On the origin of the cobalt particle size effects in Fischer-Tropsch catalysis', *Journal of the American Chemical Society*, **131**, 7197–7203, 2009
45. L. Yu, Y. Shi, Z. Zhao, H. Yin, Y. Wei, J. Liu, W. Kang, T. Jiang, A. Wang, 'Ultrasmall silver nanoparticles supported on silica and their catalytic performances for carbon monoxide oxidation', *Catalysis Communications*, **12**, 616–620, 2011
46. Z. Qu, W. Huang, M. Cheng, X. Bao, 'Restructuring and redispersion of silver on SiO₂ under oxidizing/reducing atmospheres and its activity toward CO oxidation', *Journal of Physical Chemistry B*, **109**, 15842–15848, 2005
47. H. Wei, C. Gomez, J. Liu, N. Guo, T. Wu, R. Lobo-Lapidus, C.L. Marshall, J.T. Miller, R.J. Meyer, 'Selective hydrogenation of acrolein on supported silver catalysts: A kinetics study of particle size effects', *Journal of Catalysis*, **298**, 18–26, 2013
48. J.E. van den Reijen, S. Kanungo, T.A.J. Welling, M. Versluijs-Helder, T.A. Nijhuis, K.P. de Jong, P.E. de Jongh, 'Preparation and particle size effects of Ag/ α -Al₂O₃ catalysts for ethylene epoxidation', *Journal of Catalysis*, **356**, 65–74, 2017
49. J.K. Lee, X.E. Verykios, R. Pitchai, 'Support and crystallite size effects in ethylene oxidation catalysis', *Applied Catalysis*, **50**, 171–188, 1989
50. S.N. Goncharova, E.A. Paukshtis, B.S. Bal'zhinimaev, 'Size effects in ethylene oxidation on silver catalysts. Influence of support and Cs promoter', *Applied Catalysis A: General*, **126**, 67–84, 1995
51. V.I. Bukhtiyarov, I.P. Prosvirin, R.I. Kvon, S.N. Goncharova, B.S. Bal'zhinimaev, 'XPS study of the size effect in ethene epoxidation on supported silver catalysts', *J. Chem. Soc., Faraday Trans*, **93**, 2323–2329, 1997
52. M.J. Ndolomingo, N. Bingwa, R. Meijboom, 'Review of supported metal nanoparticles: synthesis methodologies, advantages and application as catalysts', *Journal of Materials Science*, **55**, 6195–6241, 2020
53. N. Masoud, L. Delannoy, H. Schaink, A.M.J. van der Eerden, J.W. de Rijk, T.A.G. Silva, D. Banerjee, J.D. Meeldijk, K.P. de Jong, C. Louis, P.E. de Jongh, 'Superior stability of Au/SiO₂ compared to Au/TiO₂ catalysts for the selective hydrogenation of butadiene', *ACS Catalysis*, **7**, 5594–5603, 2017
54. P. Munnik, P.E. de Jongh, K.P. de Jong, 'Recent developments in the synthesis of supported catalysts', *Chemical Reviews*, **115**, 6687–6718, 2015
55. M. Wolters, L.J.W. Van Grotel, T.M. Eggenhuisen, J.R.A. Sietsma, K.P. de Jong, P.E. de Jongh, 'Combining confinement and NO calcination to arrive at highly dispersed supported nickel and cobalt oxide catalysts with a tunable particle size', *Catalysis Today*, **163**, 27–32, 2011

References

56. C.E. Pompe, M. Slagter, P.E. de Jongh, K.P. de Jong, 'Impact of heterogeneities in silica-supported copper catalysts on their stability for methanol synthesis', *Journal of Catalysis*, **365**, 1–9, 2018
57. E. Plessers, J.E. van den Reijen, P.E. de Jongh, K.P. de Jong, M.B.J. Roefsaers, 'Origin and abatement of heterogeneity at the support granule scale of silver on silica catalysts', *ChemCatChem*, **9**, 4562–4569, 2017
58. T.M. Eggenhuisen, H. Friedrich, F. Nudelman, J. Zec, N.A.J.M. Sommerdijk, P.E. de Jongh, K.P. de Jong, 'Controlling the Distribution of Supported Nanoparticles by Aqueous Synthesis', *Chemistry of Materials*, **25**, 890–896, 2013
59. T. Toupance, M. Kermarec, C. Louis, 'Metal particle size in silica-supported copper catalysts. Influence of the conditions of preparation and of thermal pretreatments', *Journal of Physical Chemistry B*, **104**, 965–972, 2000
60. E. Plessers, I. Stassen, S.P. Sree, K.P.F. Janssen, H. Yuan, J. Martens, J. Hofkens, D. De Vos, M.B.J. Roefsaers, 'Resolving interparticle heterogeneities in composition and hydrogenation performance between individual supported silver on silica catalysts', *ACS Catalysis*, **5**, 6690–6695, 2015
61. P. Munnik, N.A. Krans, P.E. de Jongh, K.P. de Jong, 'Effects of Drying Conditions on the Synthesis of Co/SiO₂ and Co/Al₂O₃ Fischer – Tropsch Catalysts', *ACS Catalysis*, **4**, 3219–3226, 2014
62. H. Hu, S. Lu, T. Li, Y. Zhang, C. Guo, H. Zhu, Y. Jin, M. Du, W. Zhang, 'Controlled growth of ultrafine metal nanoparticles mediated by solid supports', *Nanoscale Advances*, **3**, 1865–1886, 2021
63. S. Eskandari, A. Dong, L.T. De Castro, F. Bin AB Rahman, J. Lipp, D.A. Blom, J.R. Regalbuto, 'Pushing the limits of electrostatic adsorption: charge enhanced dry impregnation of SBA-15', *Catalysis Today*, **338**, 60–71, 2019
64. P. Munnik, M. Wolters, A. Gabriellson, S.D. Pollington, G. Headdock, J.H. Bitter, P.E. De Jongh, K.P. De Jong, 'Copper nitrate redispersion to arrive at highly active silica-supported copper catalysts', *Journal of Physical Chemistry C*, **115**, 14698–14706, 2011
65. Z. Bian, S. Kawi, 'Preparation, characterization and catalytic application of phyllosilicate: A review', *Catalysis Today*, **339**, 3–23, 2020
66. L.F. Chen, P.J. Guo, M.H. Qiao, S.R. Yan, H.X. Li, W. Shen, H.L. Xu, K.N. Fan, 'Cu/SiO₂ catalysts prepared by the ammonia-evaporation method: Texture, structure, and catalytic performance in hydrogenation of dimethyl oxalate to ethylene glycol', *Journal of Catalysis*, **257**, 172–180, 2008
67. J. Gong, H. Yue, Y. Zhao, S. Zhao, L. Zhao, J. Lv, S. Wang, X. Ma, 'Synthesis of ethanol via syngas on Cu/SiO₂ catalysts with balanced Cu 0-Cu + sites', *Journal of the American Chemical Society*, **134**, 13922–13925, 2012
68. F. Dong, G. Ding, H. Zheng, X. Xiang, L. Chen, Y. Zhu, Y. Li, 'Highly dispersed Cu nanoparticles as an efficient catalyst for the synthesis of the biofuel 2-methylfuran', *Catalysis Science and Technology*, **6**, 767–779, 2016
69. H. Liu, H. Wang, J. Shen, Y. Sun, Z. Liu, 'Preparation, characterization and activities of the nano-sized Ni/SBA-15 catalyst for producing CO_x-free hydrogen from ammonia', *Applied Catalysis A: General*, **337**, 138–147, 2008
70. P. Burattin, M. Che, C. Louis, 'Ni/SiO₂ materials prepared by deposition-precipitation: influence of the reduction conditions and mechanism of formation of metal particles', *Journal of Physical Chemistry B*, **104**, 10482–40489, 2000

71. W. Klein, M. Jansen, 'Synthesis and crystal structure of silver nesosilicate, Ag_4SiO_4 ', *Zeitschrift für Anorganische und Allgemeine Chemie*, **634**, 1077–1081, 2008
72. E. Thilo, F. Wodtcke, 'Chemische Untersuchungen von Silicaten. XX. Über die „neutralen“ Silbersilicate: Ag_4SiO_4 , $(\text{Ag}_2\text{SiO}_3)_n$, $(\text{Ag}_2\text{Si}_2\text{O}_5)_n$ und $\text{AgAl}_2\text{AgAl}_2[\text{AlSi}_3\text{O}_{10}](\text{OH})_2$; ihre Herstellung und Eigenschaften. Mit einer Bemerkung über die Silbercyanwasserstoffsäure $\text{H}[\text{Ag}(\text{CN})_2]$ ', *Zeitschrift für Anorganische und Allgemeine Chemie*, **295**, 247–261, 1958
73. M. Jansen, H.-L. Keller, ' $\text{Ag}_{10}\text{Si}_4\text{O}_{13}$, das erste Tetrasilicat', *Angewandte Chemie*, **91**, 500–500, 1979
74. K. Heidebrecht, M. Jansen, ' $\text{Ag}_{18}(\text{SiO}_4)_2(\text{Si}_4\text{O}_{13})$, das erste Silbersilicat mit gemischten Anionen', *ZAAC*, **597**, 79–86, 1991
75. A. Al-Keisy, L. Ren, D. Cui, Z. Xu, X. Xu, X. Su, W. Hao, S.X. Dou, Y. Du, 'A ferroelectric photocatalyst $\text{Ag}_{10}\text{Si}_4\text{O}_{13}$ with visible-light photooxidation properties', *Journal of Materials Chemistry A*, **4**, 10992–10999, 2016
76. L. Wang, J. Wu, 'A review of recent progress in silver silicate-based photocatalysts for organic pollutant degradation', *Inorganic Chemistry Communications*, **129**, 108619, 2021
77. R. Cao, H. Yang, X. Deng, S. Zhang, X. Xu, 'synthesis of amorphous silver silicate/carbonate composites for selective visible-light photocatalytic decomposition', *Scientific Reports*, **7**, 1–12, 2017
78. Y. Wang, Y. Jing, W. Li, M. Yu, X. Ao, Y. Xie, Q. Chen, 'Silicate silver/flower-like magnesium hydroxide composites for enhanced visible light photodegradation activities', *RSC Advances*, **8**, 23442–23450, 2018
79. T.G. Kim, D.H. Yeon, T. Kim, J. Lee, S.J. Im, 'Silver silicates with three-dimensional d^{10} - d^{10} interactions as visible light active photocatalysts for water oxidation', *Applied Physics Letters*, **103**, 1–5, 2013
80. M. V. Baidakova, N.A. Germanov, S.N. Golyandin, M.E. Kompan, S. V. Mochalov, A. V. Nashchekin, V.N. Nevedomskii, S.A. Pul'nev, M.K. Rabchinskii, V.P. Ulin, N. V. Ulin, 'Weakly ordered nanostructured silver disilicate and its colloidal solutions: Preparation and properties', *Technical Physics*, **64**, 884–892, 2019
81. Z. Lou, B. Huang, Z. Wang, X. Ma, R. Zhang, X. Zhang, X. Qin, Y. Dai, M.H. Whangbo, ' $\text{Ag}_6\text{Si}_2\text{O}_7$: A silicate photocatalyst for the visible region', *Chemistry of Materials*, **26**, 3873–3875, 2014
82. M.T. Galante, P. Sotelo, M.K. Hossain, A. Vali, A. Raamann, C. Longo, R.T. Macaluso, K. Rajeshwar, 'Silver oxide-based semiconductors for solar fuels production and environmental remediation: A solid-state chemistry approach', *ChemElectroChem*, **6**, 87–96, 2019
83. X. Zhu, P. Wang, B. Huang, X. Ma, X. Qin, X. Zhang, Y. Dai, 'Synthesis of novel visible light response $\text{Ag}_{10}\text{Si}_4\text{O}_{13}$ photocatalyst', *Applied Catalysis B: Environmental*, **199**, 315–322, 2016
84. X. Cui, S.H. Yu, L. Li, K. Li, B. Yu, 'Fabrication of $\text{Ag}_2\text{SiO}_3/\text{SiO}_2$ composite nanotubes using a one-step sacrificial templating solution approach', *Advanced Materials*, **16**, 1109–1112, 2004
85. J. Liu, W. Wu, Q. Tian, Z. Dai, Z. Wu, X. Xiao, C. Jiang, 'Anchoring of $\text{Ag}_6\text{Si}_2\text{O}_7$ nanoparticles on $\alpha\text{-Fe}_2\text{O}_3$ short nanotubes as a Z-scheme photocatalyst for improving their photocatalytic performances', *Dalton Transactions*, **45**, 12745–12755, 2016
86. P.E. de Jongh, T.M. Eggenhuisen, 'Melt infiltration: An emerging technique for the preparation of novel functional nanostructured materials', *Advanced Materials*, **25**, 6672–6690, 2013

References

87. P. Ngene, P. Adelhelm, A.M. Beale, K.P. de Jong, P.E. de Jongh, 'LiBH₄/SBA-15 nanocomposites prepared by melt infiltration under hydrogen pressure: Synthesis and hydrogen sorption properties', *Journal of Physical Chemistry C*, **114**, 6163–6168, 2010
88. N. Travitzky, 'Processing of ceramic–metal composites', *Advances in Applied Ceramics*, **111**, 286–300, 2012
89. L.M. de Kort, J. Harmel, P.E. de Jongh, P. Ngene, 'The effect of nanoscaffold porosity and surface chemistry on the Li-ion conductivity of LiBH₄-LiNH₂/metal oxide nanocomposites', *Journal of Materials Chemistry A*, **8**, 20687–20697, 2020
90. R. Zettl, L. de Kort, M. Gombotz, H.M.R. Wilkening, P.E. de Jongh, P. Ngene, 'Combined effects of anion substitution and nanoconfinement on the ionic conductivity of Li-based complex hydrides', *Journal of Physical Chemistry C*, **124**, 2806–2816, 2020
91. M.H.W. Verkuijlen, P. Ngene, D.W. De Kort, C. Barré, A. Nale, E.R.H. Van Eck, P.J.M. Van Bentum, P.E. De Jongh, A.P.M. Kentgens, 'Nanoconfined LiBH₄ and enhanced mobility of Li⁺ and BH₄⁻ studied by solid-state NMR', *Journal of Physical Chemistry C*, **116**, 22169–22178, 2012
92. C. Ciotonea, B. Dragoi, A. Ungureanu, C. Catrinescu, S. Petit, H. Alamdari, E. Marceau, E. Dumitriu, S. Royer, 'Improved dispersion of transition metals in mesoporous materials through a polymer-assisted melt infiltration method', *Catalysis Science and Technology*, **7**, 5448–5456, 2017
93. Y.M. Wang, Z.Y. Wu, L.Y. Shi, 'Rapid functionalization of mesoporous materials: Directly dispersing metal oxides into as-prepared SBA-15 occluded with template', *Advanced Materials*, **15**, 323–327, 2005
94. S. Chen, C. Ciotonea, A. Ungureanu, E. Dumitriu, C. Catrinescu, R. Wojcieszak, F. Dumeignil, S. Royer, 'Preparation of nickel (oxide) nanoparticles confined in the secondary pore network of mesoporous scaffolds using melt infiltration', *Catalysis Today*, **334**, 48–58, 2019
95. C.T. Campbell, 'The energetics of supported metal nanoparticles: Relationships to sintering rates and catalytic activity', *Accounts of Chemical Research*, **46**, 1712–1719, 2013
96. E.D. Goodman, J.A. Schwalbe, M. Cargnello, 'Mechanistic understanding and the rational design of sinter-resistant heterogeneous catalysts', *ACS Catalysis*, **7**, 7156–7173, 2017
97. C.H. Bartholomew, R.J. Farrauto, 'Fundamentals of industrial catalytic processes', *Fundamentals of industrial catalytic processes*, 2nd edition, John Wiley & Sons, Inc, 2005
98. C.H. Bartholomew, 'Mechanisms of catalyst deactivation', *Applied Catalysis A: General*, **212**, 17–60, 2001
99. M.D. Argyle, C.H. Bartholomew, 'Heterogeneous catalyst deactivation and regeneration: A review', *Catalysts*, **5**, 145–269, 2015
100. G. Boskovic, D. Wolf, A. Brückner, M. Baerns, 'Deactivation of a commercial catalyst in the epoxidation of ethylene to ethylene oxide - Basis for accelerated testing', *Journal of Catalysis*, **224**, 187–196, 2004
101. X.E. Verykios, F.P. Stein, R.W. Coughlin, 'Oxidation of ethylene over silver: Adsorption, kinetics, catalyst', *Catalysis Reviews*, **22**, 197–234, 1980
102. A.K. Datye, Q. Xu, K.C. Kharas, J.M. McCarty, 'Particle size distributions in heterogeneous catalysts: What do they tell us about the sintering mechanism?', *Catalysis Today*, **111**, 59–67, 2006
103. X.G. Zhou, W.K. Yuan, 'Modeling silver catalyst sintering and epoxidation selectivity evolution in ethylene oxidation', *Chemical Engineering Science*, **59**, 1723–1731, 2004

104. P. Wynblatt, N.A. Gjostein, 'Particle growth in model supported metal catalysts - I. Theory', *Acta Metallurgica*, **24**, 1165–1174, 1976
105. S.H. Joo, J.Y. Park, C.K. Tsung, Y. Yamada, P. Yang, G.A. Somorjai, 'Thermally stable Pt/mesoporous silica core-shell nanocatalysts for high-temperature reactions', *Nature Materials*, **8**, 126–131, 2009
106. P.J.F. Harris, 'Growth and structure of supported metal catalyst particles', *International Materials Reviews*, **40**, 97–115, 1995
107. G. Prieto, J. Zečević, H. Friedrich, K.P. de Jong, P.E. de Jongh, 'Towards stable catalysts by controlling collective properties of supported metal nanoparticles.', *Nature materials*, **12**, 34–39, 2013
108. T.W. Hansen, A.T. DeLaRiva, S.R. Challa, A.K. Datye, 'Sintering of catalytic nanoparticles: Particle migration or ostwald ripening?', *Accounts of Chemical Research*, **46**, 1720–1730, 2013
109. R. Ouyang, J.X. Liu, W.X. Li, 'Atomistic theory of ostwald ripening and disintegration of supported metal particles under reaction conditions', *Journal of the American Chemical Society*, **135**, 1760–1771, 2013
110. P. Munnik, M.E.Z. Velthoen, P.E. de Jongh, K.P. de Jong, C.J. Gommers, 'Nanoparticle growth in supported nickel catalysts during methanation reaction - larger is better.', *Angewandte Chemie*, **126**, 9647–9651, 2014
111. S. Hu, W.X. Li, 'Influence of particle size distribution on lifetime and thermal stability of ostwald ripening of supported particles', *ChemCatChem*, **10**, 2900–2907, 2018
112. I.M. Lifshitz, V. V. Slyozov, 'The kinetics of precipitation from supersaturated solid solutions', *Journal of Physics and Chemistry of Solids*, **19**, 35–50, 1961
113. C.E. Pompe, D.L. van Uunen, L.I. van der Wal, J.E.S. van der Hoeven, K.P. de Jong, P.E. de Jongh, 'Stability of mesocellular foam supported copper catalysts for methanol synthesis', *Catalysis Today*, 1–11, 2019
114. C. Hernández Mejía, C. Vogt, B.M. Weckhuysen, K.P. de Jong, 'Stable niobia-supported nickel catalysts for the hydrogenation of carbon monoxide to hydrocarbons', *Catalysis Today*, **343**, 56–62, 2020
115. A.R. Studart, U.T. Gonzenbach, E. Tervoort, L.J. Gauckler, 'Processing routes to macroporous ceramics: A review', *Journal of the American Ceramic Society*, **89**, 1771–1789, 2006
116. C.S. Cundy, P.A. Cox, 'The hydrothermal synthesis of zeolites: History and development from the earliest days to the present time', *Chemical Reviews*, **103**, 663–701, 2003
117. D. Zhao, Y. Wan, W. Zhou, 'Synthesis approach of mesoporous molecular sieves', in *Ordered Mesoporous Materials*, 5–54, Wiley-VCH Verlag GmbH & Co. KGaA, 2013
118. C.T. Kresge, M.E. Leonowicz, W.J. Roth, J.C. Vartuli, J.S. Beck, 'Ordered mesoporous molecular sieves synthesized by a liquid-crystal template mechanism', *Nature*, **359**, 710–712, 1992
119. D. Zhao, Y. Wan, W. Zhou, 'Mechanisms for formation of mesoporous materials', in *Ordered Mesoporous Materials*, 55–116, Wiley-VCH Verlag GmbH & Co. KGaA, 2013
120. P. Yang, D. Zhao, D. Margolese, 'Block copolymer templating syntheses of mesoporous metal oxides with large ordering lengths and semicrystalline framework', *Chemistry of Materials*, 2813–2826, 1999

121. D. Zhao, Q. Huo, J. Feng, B.F. Chmelka, G.D. Stucky, 'Nonionic triblock and star diblock copolymer and oligomeric surfactant syntheses of highly ordered, hydrothermally stable, mesoporous silica structures', *Journal of the American Chemical Society*, **120**, 6024–6036, 1998
122. D. Zhao, J. Feng, Q. Huo, N. Melosh, G.H. Fredrickson, B.F. Chmelka, G.D. Stucky, 'Triblock copolymer synthesis of mesoporous silica with periodic 50 to 300 angstrom pores', *Science*, **279**, 548–552, 1998
123. J.R.A. Sietsma, J.D. Meeldijk, M. Versluijs-Helder, A. Broersma, A. Jos Van Dillen, P.E. de Jongh, K.P. de Jong, 'Ordered mesoporous silica to study the preparation of Ni/SiO₂ ex nitrate catalysts: Impregnation, drying, and thermal treatments', *Chemistry of Materials*, **20**, 2921–2931, 2008
124. J.R.A. Sietsma, H. Friedrich, A. Broersma, M. Versluijs-Helder, A. Jos van Dillen, P.E. de Jongh, K.P. de Jong, 'How nitric oxide affects the decomposition of supported nickel nitrate to arrive at highly dispersed catalysts', *Journal of Catalysis*, **260**, 227–235, 2008
125. R.M. Rioux, H. Song, J.D. Hoefelmeyer, P. Yang, G.A. Somorjai, 'High-surface-area catalyst design: Synthesis, characterization, and reaction studies of platinum nanoparticles in mesoporous SBA-15 silica', *Journal of Physical Chemistry B*, **109**, 2192–2202, 2005
126. A. Martínez, C. López, F. Márquez, I. Díaz, 'Fischer-Tropsch synthesis of hydrocarbons over mesoporous Co/SBA-15 catalysts: The influence of metal loading, cobalt precursor, and promoters', *Journal of Catalysis*, **220**, 486–499, 2003
127. S. Singh, R. Kumar, H.D. Setiabudi, S. Nanda, D.V.N. Vo, 'Advanced synthesis strategies of mesoporous SBA-15 supported catalysts for catalytic reforming applications: A state-of-the-art review', *Applied Catalysis A: General*, **559**, 57–74, 2018
128. H. Nishihara, T. Kyotani, 'Templated nanocarbons for energy storage', *Advanced materials*, **24**, 4473–4498, 2012
129. N.D. Petkovich, A. Stein, 'Controlling macro- and mesostructures with hierarchical porosity through combined hard and soft templating', *Chemical Society reviews*, **42**, 3721–3739, 2013
130. A. Stein, R.C. Schroden, 'Colloidal crystal templating of three-dimensionally ordered macroporous solids: materials for photonics and beyond', *Solid State and Materials Science*, **5**, 553–564, 2002
131. R.C. Schroden, M. Al-Daous, C.F. Blanford, A. Stein, 'Optical properties of inverse opal photonic crystals', *Chemistry of Materials*, **14**, 3305–3315, 2002
132. O.D. Velev, T.A. Jede, R.F. Lobo, A.M. Lenhoff, 'Porous silica via colloidal crystallization', *Nature*, **389**, 447–448, 1997
133. D. Han, X. Li, L. Zhang, Y. Wang, Z. Yan, S. Liu, 'Hierarchically ordered meso/macroporous γ -alumina for enhanced hydrodesulfurization performance', *Microporous and Mesoporous Materials*, **158**, 1–6, 2012
134. G. Prieto, M. Shakeri, K.P. de Jong, P.E. de Jongh, 'Quantitative relationship between support porosity and the stability of pore-confined metal nanoparticles studied on CuZnO/SiO₂ methanol synthesis catalysts', *ACS Nano*, **8**, 2522–2531, 2014
135. N. Masoud, T. Partsch, K.P. de Jong, P.E. de Jongh, 'Thermal stability of oxide-supported Au nanoparticles', *Gold Bulletin*, **52**, 105–114, 2019
136. S. Zhang, M. Cargnello, W. Cai, C.B. Murray, G.W. Graham, X. Pan, 'Revealing particle growth mechanisms by combining high-surface-area catalysts made with monodisperse particles and electron microscopy conducted at atmospheric pressure', *Journal of Catalysis*, **337**, 240–247, 2016

137. G. Prieto, J.D. Meeldijk, K.P. De Jong, P.E. De Jongh, 'Interplay between pore size and nanoparticle spatial distribution: Consequences for the stability of CuZn/SiO₂ methanol synthesis catalysts', *Journal of Catalysis*, **303**, 31–40, 2013
138. P.I. Ravikovitch, A. V. Neimark, 'Characterization of nanoporous materials', *Colloids and Surfaces A: Physicochemical and Engineering Aspects*, **187–188**, 11–21, 2001
139. K. Cychosz, X. Guo, W. Fan, R. Cimino, 'Characterization of the pore structure of three-dimensionally ordered mesoporous carbons using high resolution gas sorption', *Langmuir*, **28**, 12647–54, 2012
140. R.M. Laine, J.C. Marchal, H.P. Sun, X.Q. Pan, 'Nano- α -Al₂O₃ by liquid-feed flame spray pyrolysis', *Nature Materials*, **5**, 710–712, 2006
141. L.P. Lefebvre, J. Banhart, D.C. Dunand, 'Porous metals and metallic foams: Current status and recent developments', *Advanced Engineering Materials*, **10**, 775–787, 2008
142. M. Abdullah, F. Iskandar, S. Shibamoto, T. Ogi, K. Okuyama, 'Preparation of oxide particles with ordered macropores by colloidal templating and spray pyrolysis', *Acta Materialia*, **52**, 5151–5156, 2004
143. A. Stein, 'Sphere templating methods for periodic porous solids', *Microporous and Mesoporous Materials*, **44–45**, 227–239, 2001
144. X. Chen, Z. Li, J. Ye, Z. Zou, 'Forced impregnation approach to fabrication of large-area, three-dimensionally ordered macroporous metal oxides', *Chemistry of Materials*, **22**, 3583–3585, 2010
145. G.R. Yi, J.H. Moon, S.M. Yang, 'Ordered macroporous particles by colloidal templating', *Chemistry of Materials*, **13**, 2613–2618, 2001
146. H. Yan, C.F. Blanford, B.T. Holland, W.H. Smyrl, A. Stein, 'General synthesis of periodic macroporous solids by templated salt precipitation and chemical conversion', *Chemistry of Materials*, **12**, 1134–1141, 2000
147. S.G. Rudisill, Z. Wang, A. Stein, 'Maintaining the structure of templated porous materials for reactive and high-temperature applications.', *Langmuir: the ACS journal of surfaces and colloids*, **28**, 7310–7324, 2012
148. M. Sadakane, T. Horiuchi, N. Kato, C. Takahashi, W. Ueda, 'Facile preparation of three-dimensionally ordered macroporous alumina, iron oxide, chromium oxide, manganese oxide, and their mixed-metal oxides with high porosity', *Chemistry of Materials*, **19**, 5779–5785, 2007
149. R.G. Munro, 'Evaluated material properties for a sintered α -alumina', *Journal of the American Ceramic Society*, **80**, 1919–1928, 1997
150. C. Sadik, I.E. El Amrani, A. Albizane, 'Recent advances in silica-alumina refractory: A review', *Journal of Asian Ceramic Societies*, **2**, 83–96, 2014
151. J.J. Amero, 'Sintered α -alumina and zirconia abrasive product and process', US3454385, 1–5, 1969
152. S.L. Conwell, W.P. Wood, 'Alpha alumina-based abrasive grain', US5516348, 1–20, 1996
153. M.J. Udy, 'Preparation of refractory products', US271822, 1–2, 1956
154. N. Setter, R. Waser, 'Electroceramic materials', *Acta Materialia*, **48**, 151–178, 2000
155. R.P. Nielsen, J.H. La Rochelle, 'Catalyst for production of ethylene oxide', US3962136, 1–22, 1976

References

156. M. Mitsuhashi, F. Watanabe, T. Kumazawa, F. Watanabe, T. Kumazawa, 'Silver catalyst for production of ethylene oxide', 4368144, 1–6, 1983
157. C.F. Mao, M. Albert Vannice, 'High surface area α -aluminas III. Oxidation of ethylene, ethylene oxide, and acetaldehyde over silver dispersed on high surface area α -alumina', *Applied Catalysis A, General*, **122**, 61–76, 1995
158. J.N. Pattison, 'Low surface area alpha alumina catalyst support for the selective hydrogenation of hydrocarbons', US3068303, 1–4, 1962
159. L.L. Murrell, D.C. Grenoble, J.P. DeLuca, 'Process for preparing ultra-stable, high surface area α -alumina', US4169883, 1976
160. R. van Santen, P. van Leeuwen, J. Moulijn, B.A. Averill, 'Preparation of catalyst support supports, zeolites and mesoporous materials', in *Catalysis: An Integrated Approach*, 433–457, 1999
161. M. Nguefack, A.F. Popa, S. Rossignol, C. Kappenstein, 'Preparation of alumina through a sol-gel process. Synthesis, characterization, thermal evolution and model of intermediate boehmite', *Phys. Chem. Chem. Phys.*, **5**, 4279–4289, 2003
162. J.G. Li, X. Sun, 'Synthesis and sintering behavior of a nanocrystalline α -alumina powder', *Acta Materialia*, **48**, 3103–3112, 2000
163. M.M. Martín-Ruiz, L.A. Pérez-Maqueda, T. Cordero, V. Balek, J. Subrt, N. Murafa, J. Pascual-Cosp, 'High surface area α -alumina preparation by using urban waste', *Ceramics International*, **35**, 2111–2117, 2009
164. K.P. Furlan, R.M. Pasquarelli, T. Krekeler, M. Ritter, R. Zierold, K. Nielsch, G.A. Schneider, R. Janssen, 'Highly porous α -Al₂O₃ ceramics obtained by sintering atomic layer deposited inverse opals', *Ceramics International*, **43**, 11260–11264, 2017
165. L. López Pérez, V. Zarubina, H.J. Heeres, I. Melia, 'Condensation-enhanced self-assembly as a route to high surface area α -aluminas', *Chemistry of Materials*, **25**, 3971–3978, 2013
166. S. Sokolov, D. Bell, A. Stein, 'Preparation and characterization of macroporous α -alumina', *Journal of the American Ceramic Society*, **86**, 1481–1486, 2003
167. D. Zou, S. Ma, M. Park, L. Sun, J.J. Aklonis, R. Salovey, 'Model filled polymers - V - Synthesis of crosslinked monodisperse polymethacrylate beads', *Journal of Polymer Science: Part A Polymer Chemistry*, **30**, 137–144, 1992
168. B. Holland, C. Blanford, A. Stein, 'Synthesis of macroporous minerals with highly ordered three-dimensional arrays of spheroidal voids', *Science*, **281**, 538–540, 1998
169. P. Scherrer, 'Bestimmung der inneren Struktur und der Größe von Kolloidteilchen mittels Röntgenstrahlen', *Kolloidchemie Ein Lehrbuch*, **277**, 387–409, 1912
170. J.I. Langford, A.J.C. Wilson, 'Scherrer after sixty years: A survey and some new results in the determination of crystallite size', *Journal of Applied Crystallography*, **11**, 102–113, 1978
171. K. Wefers, C. Misra, 'Oxides and hydroxides of aluminum', Alcoa Technical Paper No 19, 1987
172. J.Z. Mbese, P.A. Ajibade, 'Preparation and characterization of ZnS, CdS and HgS/poly(methyl methacrylate) nanocomposites', *Polymers*, **6**, 2332–2344, 2014
173. R.A. van Santen, P.W.N.M. van Leeuwen, J.A. Moulijn, B.A. Averil, 'Catalysis: An integrated approach', 1999
174. P. Souza Santos, H. Souza Santos, S.P. Toledo, 'Standard transition aluminas. Electron microscopy studies', *Materials Research*, **3**, 104–114, 2000

175. R. Román, M.T. Hernández, A. Ibarra, R. Vila, J. Mollá, P. Martín, M. González, 'The effect of carbon additives on the dielectric behaviour of alumina ceramics', *Acta Materialia*, **54**, 2777–2782, 2006
176. R. Besler, M. Rossetti Da Silva, J.J. Do Rosario, M. Dosta, S. Heinrich, R. Janssen, 'Sintering simulation of periodic macro porous alumina', *Journal of the American Ceramic Society*, **98**, 3496–3502, 2015
177. F.F. Lange, 'Densification of powder compacts: An unfinished story', *Journal of the European Ceramic Society*, **28**, 1509–1516, 2008
178. J.E. Palmer, C. V. Thompson, H.I. Smith, 'Grain growth and grain size distributions in thin germanium films', *Journal of Applied Physics*, **62**, 2492–2497, 1987
179. K. Assaker, C. Carteret, P. Durand, L. Aranda, M.J. St??b??, J.L. Blin, 'Hydrothermal stability of ordered surfactant-templated titania', *Journal of Physical Chemistry C*, **117**, 16500–16508, 2013
180. C.F. Blanford, R.C. Schrodin, M. Al-Daous, A. Stein, 'Tuning solvent-dependent color changes of three-dimensionally ordered macroporous (3DOM) materials through compositional and geometric modifications', *Advanced Materials*, **13**, 26–29, 2001
181. E.S. Zouboulis, M. Grimsditch, 'Refractive index and elastic properties of single-crystal corundum (α -Al₂O₃) up to 2100 K', *Journal of Applied Physics*, **70**, 772–776, 1991
182. R. Zhang, A. a. Elzatahry, S.S. Al-Deyab, D. Zhao, 'Mesoporous titania: From synthesis to application', *Nano Today*, **7**, 344–366, 2012
183. A.S. Deshpande, D.G. Shchukin, E. Ustinovich, M. Antonietti, R. a. Caruso, 'Titania and mixed titania/aluminum, gallium, or indium oxide spheres: Sol-gel/template synthesis and photocatalytic properties', *Advanced Functional Materials*, **15**, 239–245, 2005
184. A.J.F. Van Hoof, I.A.W. Filot, H. Friedrich, E.J.M. Hensen, 'Reversible restructuring of silver particles during ethylene epoxidation', *ACS Catalysis*, **8**, 11794–11800, 2018
185. C.T. Campbell, M.T. Paffett, 'Model studies of ethylene epoxidation catalyzed by the Ag(110) surface', *Surface Science*, **139**, 396–416, 1984
186. M. Mavrikakis, D.J. Doren, M.A. Barteau, 'Density functional theory calculations for simple oxametallacycles: Trends across the periodic table', *J. Phys. Chem. B*, **102**, 394–399, 1998
187. A.M. Lauritzen, 'Ethylene oxide catalyst and process for preparing the catalyst', US4761394, 1–27, 1988
188. S. Rebsdatt, D. Mayer, 'Arsenic and arsenic compounds.', *IARC monographs on the evaluation of the carcinogenic risk of chemicals to humans*, vol. 23 39–141, 1980
189. A. Ayame, Y. Uchida, H. Ono, T. Sato, H. Hayasaka, 'Epoxidation of ethene over silver catalysts supported on crystalline α -alumina carriers', *Studies in Surface Science and Catalysis*, **145**, 509–510, 2003
190. E. Ruckenstein, S.H. Lee, 'The behavior of model Ag/Al₂O₃ catalysts in various chemical environments', *Journal of Catalysis*, **109**, 100–119, 1988
191. M. Bowker, 'Effects of sintering on the active site distribution on promoted catalysts', *Applied Catalysis*, **45**, 115–130, 1988
192. T. Zambelli, J. Barth, J. Winterlin, 'Formation mechanism of the O-induced added-row reconstruction on Ag(110): A low-temperature STM study', *Physical Review B - Condensed Matter and Materials Physics*, **58**, 12663–12666, 1998

References

193. S.R. Seyedmonir, D.E. Strohmayer, G.J. Guskey, G.L. Geoffroy, M.A. Vannice, 'Characterization of supported silver catalysts. III. Effects of support, pretreatment, and gaseous environment on the dispersion of Ag', *Journal of Catalysis*, **93**, 288–302, 1985
194. A.J.F. van Hoof, R.C.J. van der Poll, H. Friedrich, E.J.M. Hensen, 'Dynamics of silver particles during ethylene epoxidation', *Applied Catalysis B: Environmental*, **272**, 118983, 2020
195. M. Matusz, 'Process for preparing ethylene oxide catalysts', 1–17, 1998
196. M.S.C. Chan, E. Marek, S.A. Scott, J.S. Dennis, 'Chemical looping epoxidation', *Journal of Catalysis*, **359**, 1–7, 2018
197. W.L. Suchanek, J.M. Garcés, P.F. Fulvio, M. Jaroniec, 'Hydrothermal synthesis and surface characteristics of novel alpha alumina nanosheets with controlled chemical composition', *Chemistry of Materials*, **22**, 6564–6574, 2010
198. D.L. Perry, 'Handbook of inorganic compounds', 1995
199. J. Lu, J.J. Bravo-Suárez, A. Takahashi, M. Haruta, S.T. Oyama, 'In situ UV-vis studies of the effect of particle size on the epoxidation of ethylene and propylene on supported silver catalysts with molecular oxygen', *Journal of Catalysis*, **232**, 85–95, 2005
200. S. Linic, M.A. Barteau, 'Formation of a stable surface oxametallacycle that produces ethylene oxide', *Journal of the American Chemical Society*, **124**, 310–317, 2002
201. M.O. Özbek, I. Onal, R.A. Van Santen, 'Effect of surface and oxygen coverage on ethylene epoxidation', *Topics in Catalysis*, **55**, 710–717, 2012
202. V. Amendola, O.M. Bakr, F. Stellacci, 'A study of the surface plasmon resonance of silver nanoparticles by the discrete dipole approximation method: Effect of shape, size, structure, and assembly', *Plasmonics*, **5**, 85–97, 2010
203. A. Liebsch, 'Surface-plasmon dispersion and size dependence of Mie resonance: Silver versus simple metals', *Physical Review B*, **48**, 11317–11328, 1993
204. Y. Han, R. Lupitsky, T.M. Chou, C.M. Stafford, H. Du, S. Sukhishvili, 'Effect of oxidation on surface-enhanced raman scattering activity of silver nanoparticles: A quantitative correlation', *Analytical Chemistry*, **83**, 5873–5880, 2011
205. G. Boskovic, N. Dropka, D. Wolf, A. Brückner, M. Baerns, 'Deactivation kinetics of Ag/Al₂O₃ catalyst for ethylene epoxidation', *Journal of Catalysis*, **226**, 334–342, 2004
206. B. Delmon, 'Characterization of catalyst deactivation: Industrial and laboratory time scales', *Applied Catalysis*, **15**, 1–16, 1985
207. A.E.B. Presland, G.L. Price, D.L. Trimm, 'Particle size effects during the sintering of silver oxidation catalysts', *Journal of catalysis*, **26**, 313–317, 1972
208. W.M. Shen, J.A. Dumesic, C.G. Hill, 'Criteria for stable Ni particle size under methanation reaction conditions: Nickel transport and particle size growth via nickel carbonyl', *Journal of Catalysis*, **68**, 152–165, 1981
209. D. Guo, Q. Guo, K. Zheng, E.G. Wang, X. Bao, 'Initial growth and oxygen adsorption of silver on Al₂O₃ film', *Journal of Physical Chemistry C*, **111**, 3981–3985, 2007
210. C. Petitto, G. Delahay, 'A new way for silver alumina catalyst preparation', *Catalysis Letters*, **142**, 433–438, 2012

211. D.B. Rasmussen, T.V.W. Janssens, B. Temel, T. Bligaard, B. Hinnemann, S. Helveg, J. Sehested, 'The energies of formation and mobilities of Cu surface species on Cu and ZnO in methanol and water gas shift atmospheres studied by DFT', *Journal of Catalysis*, **293**, 205–214, 2012
212. S.R. Seyedmonir, J.K. Plischke, M.A. Vannice, H.W. Young, 'Ethylene oxidation over small silver crystallites', *Journal of Catalysis*, **123**, 534–549, 1990
213. W.E. Evans, P.I. Chipman, 'Process for operating the epoxidation of ethylene', WO2001096324A2, 2001
214. S.T. Oyama, 'Mechanisms in homogeneous and heterogeneous epoxidation catalysis', 1st edition, Elsevier B.V., 2008
215. R.E. Kenson, M. Lapkin, 'Kinetics and mechanism of ethylene oxidation. Reactions of ethylene and ethylene oxide on a silver catalyst', *The Journal of Physical Chemistry*, **74**, 1493–1502, 1970
216. J.E. van den Reijen, W.C. Versluis, S. Kanungo, M.F. D'Angelo, K.P. de Jong, P.E. de Jongh, 'From qualitative to quantitative understanding of support effects on the selectivity in silver catalyzed ethylene epoxidation', *Catalysis Today*, **338**, 31–39, 2019
217. J.H. Miller, A. Joshi, X. Li, A. Bhan, 'Catalytic degradation of ethylene oxide over Ag/ α -Al₂O₃', *Journal of Catalysis*, **389**, 714–720, 2020
218. J.T. Jankowiak, M.A. Barteau, 'Ethylene epoxidation over silver and copper-silver bimetallic catalysts: II. Cs and Cl promotion', *Journal of Catalysis*, **236**, 379–386, 2005
219. J.C. Dellamorte, J. Lauterbach, M.A. Barteau, 'Rhenium promotion of Ag and Cu-Ag bimetallic catalysts for ethylene epoxidation', *Catalysis Today*, **120**, 182–185, 2007
220. J.T. Jankowiak, M.A. Barteau, 'Ethylene epoxidation over silver and copper-silver bimetallic catalysts: I. Kinetics and selectivity', *Journal of Catalysis*, **236**, 366–378, 2005
221. A.R. Fiorucci, L.M. Saran, E.T.G. Cavalheiro, E.A. Neves, 'Thermal stability and bonding in the silver complexes of ethylenediaminetetraacetic acid', *Thermochimica Acta*, **356**, 71–78, 2000
222. P. Petit, D. Salem, M. He, M. Paillet, R. Parret, J.L. Sauvajol, A. Zahab, 'Study of the thermal stability of supported catalytic nanoparticles for the growth of single-walled carbon nanotubes with narrow diameter distribution by chemical vapor deposition of methane', *Journal of Physical Chemistry C*, **116**, 24123–24129, 2012
223. D.L. Trimm, 'Thermal stability of catalyst supports', *Studies in Surface Science and Catalysis*, **68**, 29–51, 1991
224. T.M. Eggenhuisen, J.P. den Breejen, D. Verdoes, P.E. de Jongh, K.P. de Jong, 'Fundamentals of melt infiltration for the preparation of supported metal catalysts. The case of Co/SiO₂ for Fischer-Tropsch synthesis', *Journal of American Chemical Society*, **132**, 18318–18325, 2010
225. M.Y. Wang, Z.Y. Wu, H.J. Wang, J.H. Zhu, 'Fabrication of metal oxides occluded in ordered mesoporous hosts via a solid-state grinding route: The influence of host – guest interactions', *Advanced Functional Materials*, **16**, 2374–2386, 2006
226. S. Yang, W. Su, S.D. Lin, J. Rick, J. Cheng, J. Liu, C. Pan, D. Liu, J. Lee, T. Chan, H. Sheu, B. Hwang, 'Preparation of nano-sized Cu from a rod-like CuFe₂O₄: Suitable for high performance catalytic applications', *Applied Catalysis B: Environmental*, **106**, 650–656, 2011
227. L.M. Worboys, P.P. Edwards, P.A. Anderson, 'Silver nanowires: inclusion in and extrusion from a mesoporous template', *Chemical Communications*, **2**, 2894–2895, 2002

References

228. H.I. Lee, J.H. Kim, G.D. Stucky, Y. Shi, C. Pak, J.M. Kim, 'Morphology-selective synthesis of mesoporous SBA-15 particles over micrometer, submicrometer and nanometer scales', *Journal of Materials Chemistry*, **20**, 8483–8487, 2010
229. K.H. Stern, 'High temperature properties and decomposition of inorganic salts Part 3. Nitrates and nitrites', *Journal of Physical and Chemical Reference Data*, **1**, 747–772, 1972
230. G.H. Findenegg, S. Jähnert, D. Akcakayiran, A. Schreiber, 'Freezing and melting of water confined in silica nanopores', *ChemPhysChem*, **9**, 2651–2659, 2008
231. R.L. Oliveira, M. Shakeri, J.D. Meeldijk, K.P. de Jong, P.E. de Jongh, 'Mapping nanocavities in plugged SBA-15 with confined silver nanostructures', *Microporous and Mesoporous Materials*, **201**, 234–239, 2015
232. C. de Mello Donegá, P. Liljeroth, D. Vanmaekelbergh, 'Physicochemical evaluation of the hot-injection method, a synthesis route for monodisperse nanocrystals', *Small*, **1**, 1152–1162, 2005
233. V. Uvarov, I. Popov, 'An estimation of the correctness of XRD results obtained from the analysis of materials with bimodal crystallite size distribution', *CrystEngComm*, **17**, 8300–8306, 2015
234. M.A. Vannice, B. Sen, 'Metal-support effects on the intramolecular selectivity of crotonaldehyde hydrogenation over platinum', *Journal of Catalysis*, **115**, 65–78, 1989
235. E. Plessers, D.E. De Vos, M.B.J. Roeflaers, 'Chemoselective reduction of α,β -unsaturated carbonyl compounds with UiO-66 materials', *Journal of Catalysis*, **340**, 136–143, 2016
236. P.G.N. Mertens, P. Vandezande, X. Ye, H. Poelman, I.F.J. Vankelecom, D.E. De Vos, 'Recyclable Au⁰, Ag⁰ and Au⁰-Ag⁰ nanocolloids for the chemoselective hydrogenation of α,β -unsaturated aldehydes and ketones to allylic alcohols', *Applied Catalysis A: General*, **355**, 176–183, 2009
237. X. Yang, A. Wang, X. Wang, T. Zhang, K. Han, J. Li, 'Combined experimental and theoretical investigation on the selectivities of Ag, Au, and Pt catalysts for hydrogenation of crotonaldehyde', *Journal of Physical Chemistry C*, **113**, 20918–20926, 2009
238. X. Zhang, Z. Qu, X. Li, M. Wen, X. Quan, D. Ma, J. Wu, 'Studies of silver species for low-temperature CO oxidation on Ag/SiO₂ catalysts', *Separation and Purification Technology*, **72**, 395–400, 2010
239. Z. Qu, M. Cheng, W. Huang, X. Bao, 'Formation of subsurface oxygen species and its high activity toward CO oxidation over silver catalysts', *Journal of Catalysis*, **229**, 446–458, 2005
240. K.A. Bethke, H.H. Kung, 'Supported Ag catalysts for the lean reduction of NO with C₃H₆', *Journal of Catalysis*, **172**, 93–102, 1997
241. V. V. Dutov, G. V. Mamontov, V.I. Zaikovskii, L.F. Liotta, O. V. Vodyankina, 'Low-temperature CO oxidation over Ag/SiO₂ catalysts: Effect of OH/Ag ratio', *Applied Catalysis B: Environmental*, **221**, 598–609, 2018
242. G. Corro, U. Pal, E. Ayala, E. Vidal, 'Diesel soot oxidation over silver-loaded SiO₂ catalysts', *Catalysis Today*, **212**, 63–69, 2013
243. Z. Lou, Z. Wang, B. Huang, Y. Dai, G. Wang, Z. Jiang, X. Zhang, X. Qin, Y. Li, 'One-step synthesis of amorphous silver silicates with tunable light absorption spectra and photocatalytic activities in the visible region', *Chemistry - A European Journal*, **21**, 8706–8710, 2015
244. S. Zhang, H. Gao, X. Liu, Y. Huang, X. Xu, N.S. Alharbi, T. Hayat, J. Li, 'Hybrid 0D-2D nanoheterostructures: In situ growth of amorphous silver silicates dots on g-C₃N₄ nanosheets for full-spectrum photocatalysis', *ACS Applied Materials and Interfaces*, **8**, 35138–35149, 2016

245. M. Jansen, 'Homoatomic d^{10} - d^{10} interactions: Their effects on structure and chemical and physical properties', *Angewandte Chemie International Edition in English*, **26**, 1098–1110, 1987
246. H. Beyer, P.A. Jacobs, J.B. Uytterhoeven, 'Redox behaviour of transition metal ions in zeolites. Part 2. - Kinetic study of the reduction and reoxidation of silver-Y zeolites', *J. Chem. Soc., Faraday Trans. 1*, **72**, 674–685, 1976
247. L.R. Gellens, W.J. Mortier, J.B. Uytterhoeven, 'Oxidation and reduction of silver in zeolite Y: A structural study', *Zeolites*, **1**, 85–90, 1981
248. K. ichi Shimizu, K. Sawabe, A. Satsuma, 'Self-regenerative silver nanocluster catalyst for CO oxidation', *ChemCatChem*, **3**, 1290–1293, 2011
249. X. Zhang, H. Dong, Y. Wang, N. Liu, Y. Zuo, L. Cui, 'Study of catalytic activity at the Ag/Al-SBA-15 catalysts for CO oxidation and selective CO oxidation', *Chemical Engineering Journal*, **283**, 1097–1107, 2016
250. R.P. Zhang, W.C. Li, G.P. Hao, A.H. Lu, 'Confined nanospace pyrolysis: A versatile strategy to create hollow structured porous carbons', *Nano Research*, **12**, 1–15, 2021
251. X.L. Zhou, H. Zhang, L.M. Shao, F. Lü, P.J. He, 'Preparation and application of hierarchical porous carbon materials from waste and biomass: A review', *Waste and Biomass Valorization*, **12**, 1699–1724, 2021
252. C. Hernández Mejía, J.H. den Otter, J.L. Weber, K.P. de Jong, 'Crystalline niobia with tailored porosity as support for cobalt catalysts for the Fischer–Tropsch synthesis', *Applied Catalysis A: General*, **548**, 143–149, 2017
253. M. Iwasaki, S.A. Davis, S. Mann, 'Spongelike macroporous TiO_2 monoliths prepared from starch gel template', *Journal of Sol-Gel Science and Technology*, **32**, 99–105, 2004
254. E.J. Foster, N. Zahed, C. Tallon, 'The transformative and versatile role of cellulose nanomaterials in templating and shaping multiscale mesostructured ceramics', *Small*, **14**, 1–5, 2018
255. J.Y. Park, 'Lithographically patterned micro-/nanostructures via colloidal lithography', *Korean Journal of Chemical Engineering*, **31**, 541–547, 2014
256. M. Pisco, F. Galeotti, 'Nano- and micropatterning on optical fibers by bottom-up approach: The importance of being ordered', *Applied Sciences*, **11**, 1–24, 2021
257. M.A. Moradi, E.D. Eren, M. Chiappini, S. Rzadkiewicz, M. Goudzwaard, M.M.J. van Rijt, A.D.A. Keizer, A.F. Routh, M. Dijkstra, G. de With, N. Sommerdijk, H. Friedrich, J.P. Patterson, 'Spontaneous organization of supracolloids into three-dimensional structured materials', *Nature Materials*, **20**, 541–547, 2021
258. S.M. George, 'Atomic layer deposition: An overview', *Chemical Reviews*, **110**, 111–131, 2010
259. S. Pu, L. Li, J. Ma, F. Lu, J. Li, 'Disperse fine equiaxed alpha alumina nanoparticles with narrow size distribution synthesised by selective corrosion and coagulation separation', *Scientific Reports*, **5**, 1–8, 2015
260. A.P. Amrute, Z. Łodziana, H. Schreyer, C. Weidenthaler, F. Schüth, 'High-surface-area corundum by mechanochemically induced phase transformation of boehmite', *Science*, **366**, 485–489, 2019
261. T.C.R. Rocha, M. Hävecker, A. Knop-Gericke, R. Schlögl, 'Promoters in heterogeneous catalysis: The role of Cl on ethylene epoxidation over Ag', *Journal of Catalysis*, **312**, 12–16, 2014
262. M.O. Özbek, I. Önal, R.A. VanSanten, 'Chlorine and caesium promotion of silver ethylene epoxidation catalysts', *ChemCatChem*, **5**, 443–451, 2013

References

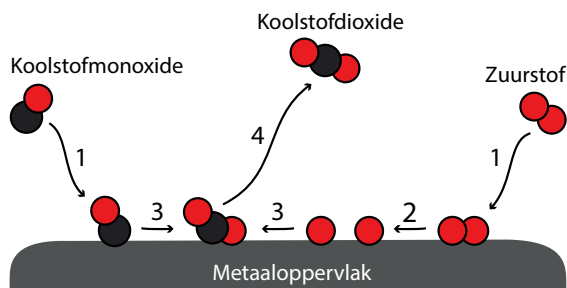
263. K. Loza, M. Heggen, M. Epple, 'Synthesis, structure, properties, and applications of bimetallic nanoparticles of noble metals', *Advanced Functional Materials*, **30**, 1–14, 2020
264. G.I.N. Waterhouse, M.R. Waterland, 'Opal and inverse opal photonic crystals: Fabrication and characterization', *Polyhedron*, **26**, 356–368, 2007
265. L.M. Anovitz, D.R. Cole, 'Characterization and analysis of porosity and pore structures', *Reviews in Mineralogy and Geochemistry*, **80**, 61–164, 2015
266. Ö.Z. Cebeci, 'Mercury intrusion porosimetry theory and its application to air-entrained cement pastes and mortars', 1977
267. G. Bertozzi, G. Sternheim, 'Surface tension of liquid nitrate systems', *The Journal of Physical Chemistry*, **68**, 2908–2912, 1964

Nederlandse samenvatting voor iedereen

Dit proefschrift gaat over gedragen zilverkatalysatoren. In deze samenvatting probeer ik uit te leggen waar het onderzoek over gaat en wat de belangrijkste resultaten van mijn onderzoek zijn. Ik hoop dat je hierdoor een beter beeld kunt krijgen van de inhoud van dit proefschrift, ook als je geen of weinig chemische kennis hebt. Voordat ik begin over wat ik heb onderzocht, geef ik eerst een korte achtergrond over katalyse in het algemeen, en gedragen zilverkatalysatoren in het bijzonder.

Waarom zijn katalysatoren belangrijk? Bij meer dan 85% van alle chemicaliën en materialen die industrieel geproduceerd worden, wordt gebruik gemaakt van een katalysator. Katalysatoren kunnen alternatieve reactiepaden bieden, waardoor specifieke chemische reacties beter lopen. Hierdoor kunnen chemische reacties onder gunstigere reactieomstandigheden plaatsvinden of, nog belangrijker, kan de opbrengst van het gewenste materiaal worden geoptimaliseerd, waarbij er zo min mogelijk bijproducten worden gevormd.

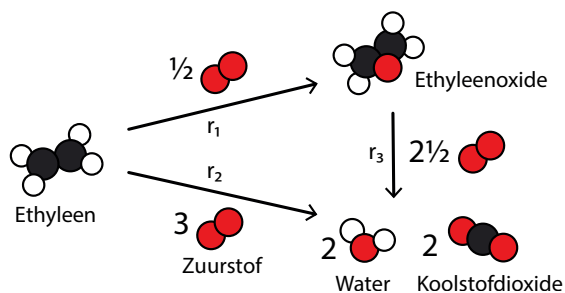
In dit proefschrift wordt gebruik gemaakt van heterogene katalysatoren. Dit zijn katalysatoren die in een andere fase zijn (meestal zijn katalysatoren vaste stoffen) dan de reactanten en producten (meestal zijn dit vloeistoffen of gassen). Binnen de heterogene katalyse wordt vaak gebruik gemaakt van metalen, waarvan alleen het oppervlak van het metaal actief is. Door de interactie van de moleculen met het metaaloppervlak kunnen reacties plaatsvinden, die niet zonder dit metaaloppervlak hadden kunnen plaatsvinden. In Figuur 1 is een versimpelde weergave van de oxidatie van koolstofmonoxide op een metaaloppervlak uitgebeeld. In de eerste stap gaan de reactanten, bestaande uit koolstofmonoxide (CO) en zuurstof (O_2) moleculen, een interactie aan met het metaaloppervlak (1). Door deze interactie verzwakken de bindingen in de moleculen. Sommige moleculen blijven intact, zoals hier koolstofmonoxide, terwijl andere moleculen splitsen, zoals hier zuurstof, dat in twee losse zuurstofatomen (O) splitst (2). Een van deze zuurstofatomen gaat een reactie aan met koolstofmonoxide, waarbij koolstofdioxide (CO_2) wordt gevormd (3). Het gevormde koolstofdioxide verlaat hierna het oppervlak (4), om ruimte te maken voor een volgende reactie.



Figuur 1 Schematische weergave van de oxidatie van koolstofmonoxide op een metaaloppervlak. Eerst adsorberen beide reactanten, koolstofmonoxide (CO) en zuurstof (O_2), op het metaaloppervlak (1), waarbij zuurstof splitst in twee losse atomen (2). Daarna vindt een reactie plaats waarbij koolstofdioxide (CO_2) wordt gevormd (3) en het metaaloppervlak verlaat (4).

De werking van de katalysator hangt af van de specifieke bindingssterkte tussen het metaaloppervlak en de moleculen, zowel de reactanten als de producten. Deze bindingssterkte moet precies goed zijn voor de juiste werking, en is bepalend voor de activiteit van de katalysator. Bij een te zwakke binding tussen de reactanten en het metaaloppervlak zie geen effect van de katalysator, omdat de bindingen binnen de reactanten dan niet genoeg verzwakt worden. Aan de andere kant loopt de reactie ook niet goed als de interactie te sterk is, want dan blijven de producten op het metaaloppervlak zitten. Elk metaal heeft een specifieke interactie met elk soort molecuul. Daarnaast hangt de bindingssterkte ook af van de vorm van de metaaldeeltjes, de directe omgeving van deze deeltjes en van de reactieomstandigheden, zoals temperatuur en druk. Omdat de optimale interactie tussen het metaaloppervlak en de moleculen zo belangrijk is, zijn er katalysatoren in heel veel verschillende soorten en maten.

Waarom zijn zilverkatalysatoren belangrijk? Voor de meeste chemische reacties zijn meerdere metalen geschikt als katalysator, omdat deze allemaal een goede bindingssterkte met zowel de reactanten als de producten hebben. Voor sommige reacties is de keuze uit metalen erg gelimiteerd. Een voorbeeld is de epoxidatie van ethyleen (ook etheen genoemd) naar ethyleenoxide (etheenoxide). Deze reactie is uitgebeeld in Figuur 2. Ethyleenoxide is een belangrijke chemische bouwsteen, met een jaarlijkse, wereldwijde productie van meer dan 35 miljard kilogram. Het wordt vooral gebruikt voor het maken van antivriesvloeistof en kunststoffen. Een katalysator is voor deze reactie nodig, omdat de vorming van ethyleenoxide (r_1) energetisch minder gunstig is dan de verbranding van ethyleen, waarbij koolstofdioxide en water ontstaan (r_2). De selectiviteit van de reactie, de vorming van ethyleenoxide in plaats van water en koolstofdioxide, is dus erg belangrijk. Ethyleenoxide is een epoxide (vandaar de naam “epoxidatiereactie”), wat betekent dat het molecuul een ring structuur heeft bestaande uit een zuurstofatoom en twee koolstofatomen. Door deze ring, waar als het ware spanning op staat, is ethyleenoxide niet erg stabiel. Hierdoor kan het gemakkelijk verder reageren naar water en koolstofdioxide (r_3). Met de juiste interactie tussen zilver en zuurstof, ethyleen en ethyleenoxide, is zilver een van de weinige katalysatoren waarmee ethyleenoxide gevormd kan worden dat het metaaloppervlak kan verlaten voordat het verder reageert.



Figuur 2 Schematische weergave van de oxidatie van ethyleen, waarbij ethyleenoxide (r_1) of water en koolstofdioxide (r_2) kan worden gevormd. Daarnaast kan ethyleenoxide na vorming verder oxideren tot water en koolstofdioxide (r_3).

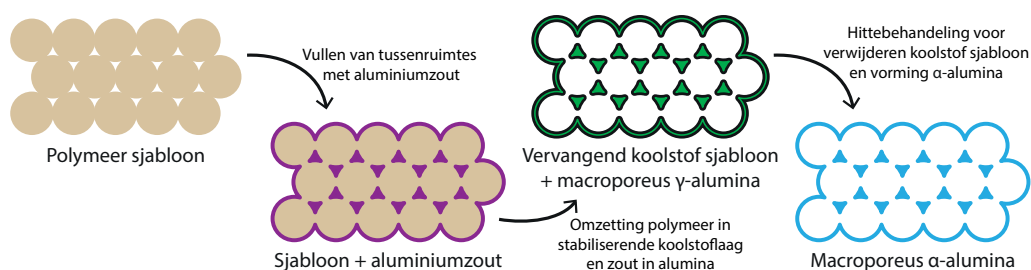
Een andere reactie waarbij op grote schaal zilverkatalysatoren gebruikt worden is de productie van formaldehyde uit methanol. Formaldehyde is een chemische bouwsteen, die voornamelijk wordt gebruikt voor het maken van industriële hars voor bindmiddelen, lijmen en afwerkmiddelen. Naast onderzoek voor het gebruiken van zilverkatalysatoren voor deze industriële toepassingen, wordt er steeds meer academisch onderzoek gedaan naar het gebruik van zilver voor andere (selectieve) oxidatie- en hydrogenatiereacties (het toevoegen van zuurstof- respectievelijk waterstofatomen aan reactanten) en het gebruik van zilver als foto- en elektrokatalysator (waarbij licht of elektriciteit als energiebron wordt gebruikt). Voor de meeste reacties weten we dat er metalen zijn die meer reactanten per tijdseenheid (hogere activiteit) kunnen omzetten dan zilver. Echter, in veel gevallen laat zilver een hogere selectiviteit zien naar de gewenste producten, waardoor katalysatoren met zilver toch heel interessant kunnen zijn.

Meestal wordt gebruik gemaakt van kleine metaaldeeltjes voor de beste katalytische prestaties. De activiteit van de katalysator per hoeveelheid zilver wordt groter, naarmate de zilverdeeltjes kleiner worden. Bij kleinere deeltjes is er namelijk meer actief oppervlakte beschikbaar, per hoeveelheid zilver, dan bij grotere deeltjes. Ook zijn de grootte en vorm van de deeltjes belangrijk voor de activiteit en selectiviteit van de chemische reactie, aangezien deze eigenschappen van invloed zijn op de interactie met de moleculen. Het is daarom van groot belang dat de zilverdeeltjes hun grootte en vorm tijdens de chemische reacties behouden. Echter, de meeste chemische reacties vinden plaats op relatief hoge temperaturen en onder verhoogde druk, waardoor kleine zilverdeeltjes gemakkelijk weer kunnen samensmelten. Om de stabiliteit van de zilverdeeltjes te verbeteren, worden ze veelal op een dragermateriaal afgezet. Dit dragermateriaal is meestal een poreus materiaal, met een hoog oppervlak, zodat er ruimte is tussen de individuele zilverdeeltjes. Daarnaast zijn de poriën nodig voor de toe- en afvoer van reactanten en producten van en naar de zilverdeeltjes. Populaire dragermaterialen zijn metaaloxiden, zoals alumina of silica, omdat deze goedkoop, mechanisch sterk, en gemakkelijk te vormen zijn.

Waarom is dit onderzoek naar gedragen zilverkatalysatoren belangrijk? Door katalysatoren verder te verbeteren, kunnen we chemische reacties nog efficiënter maken. Dit is nodig om bijvoorbeeld de uitstoot van koolstofdioxide verder te verminderen. Op dit moment wordt de jaarlijkse uitstoot van koolstofdioxide als bijproduct van de epoxidatie van ethyleen (Figuur 2) op 28 miljard kilogram geschat, wat bijna evenveel is als de productie van ethyleenoxide zelf. Door meer onderzoek te doen naar de werking van katalysatoren kunnen we de chemische processen die op de katalysator plaatsvinden steeds beter begrijpen, waardoor we de prestaties van de katalysatoren nog beter kunnen maken.

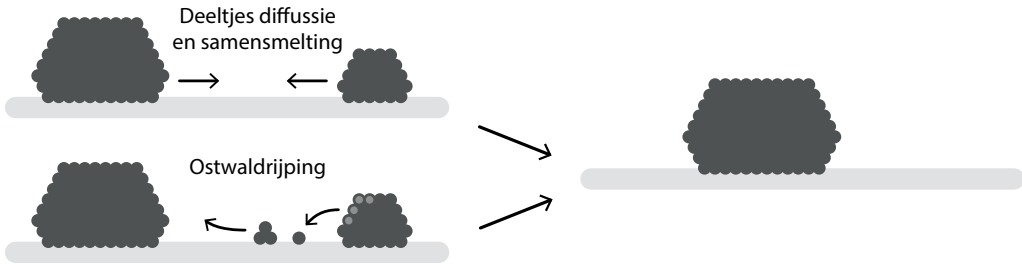
Om de invloed van specifieke parameters op de prestatie van de katalysator te onderzoeken, maken we gebruik van modelkatalysatoren. Dit zijn nog steeds volledig werkende katalysatoren, maar waarbij we specifieke eigenschappen van die katalysator uitkiezen en die precies zo maken als gewenst. In dit proefschrift gebruiken we model dragermaterialen met geordende poriestructuren. Dit vereenvoudigt het systeem en maakt het gebruik van

geavanceerde karakteriseringstechnieken krachtiger. In **Hoofdstuk 2** staat de bereiding van geordend macroporeus α -alumina beschreven. Het speciale van dit materiaal is het relatief hoge specifieke oppervlak ($30 \text{ m}^2 \text{ g}^{-1}$) en de geordende poriestructuur met poriën van ongeveer 200 nm in diameter, in combinatie met de α -fase van het alumina. α -Alumina wordt normaliter namelijk pas gevormd bij een hittebehandeling van een aluminiumzout of een ander soort alumina boven de $1100 \text{ }^\circ\text{C}$. Bij gebruik van een aluminiumzout worden eerst andere alumina fases gevormd voordat uiteindelijk de α -fase bereikt wordt. Door deze verschillende faseovergangen en de hoge temperatuur die nodig is, stort de poriestructuur in. In de door ons beschreven bereiding, schematisch te zien in Figuur 3, hebben we de poriestructuur extra stabiliteit kunnen geven tijdens de cruciale stappen van de bereiding.



Figuur 3 Schematische weergave van bereiding macroporeus α -alumina via de vorming van een stabiliserend koolstof sjabloon.

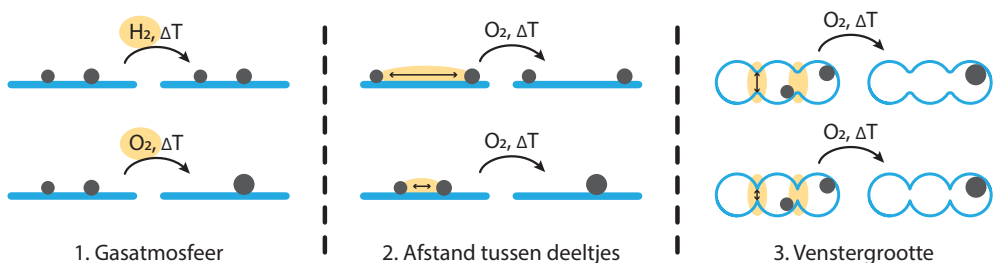
In **Hoofdstuk 3** hebben we onderzocht welke aspecten belangrijk zijn voor de groei van zilverdeeltjes. Ondanks de stabiliserende werking van het dragermateriaal op de zilverdeeltjes, kan gedurende de reactie toch deeltjesgroei plaatsvinden. Voor de katalysatoren die gebruikt worden in de epoxidatie van ethyleen (zie Figuur 2) is het verlies van zilveroppervlak door het groeien van de deeltjes zelfs een van de meest belangrijke factoren voor het verliezen van activiteit. Uit eerdere studies weten we dat er twee belangrijke mechanismes voor deeltjesgroei zijn, waarbij in de een de verplaatsing van gehele zilverdeeltjes centraal staat (diffusie en samensmelting), en in de ander de verplaatsing van clusters bestaande uit enkele of een paar zilveratomen (Ostwaldrijping). Beide mechanismes zijn uitgebeeld in Figuur 4. Bij de verplaatsing van gehele deeltjes over het drageroppervlak, kunnen twee deeltjes dicht bij elkaar komen, en vervolgens samensmelten tot één groter deeltje. Hierbij helpt het vermijden van ontmoetingen tussen deeltjes dus om de groei van de deeltjes tegen te houden. Deeltjesgroei via Ostwaldrijping ontstaat doordat kleinere deeltjes energetisch minder stabiel zijn dan grotere deeltjes. Losse zilveratomen of clusters van enkele zilveratomen kunnen zich van de kleine zilverdeeltjes losmaken, zich verplaatsen en met andere veelal grotere zilverdeeltjes samensmelten. Netto vindt een verplaatsing van zilver van kleinere naar grotere deeltjes plaats, waardoor grote deeltjes steeds groter worden ten koste van de kleine deeltjes. Omdat Ostwaldrijping gedreven wordt door de verschillen in deeltjesgroottes, gaat het verkleinen van die verschillen de deeltjesgroei via Ostwaldrijping tegen.



Figuur 4 Schematische weergave van deeltjesgroei via twee verschillende mechanismes.

Om inzicht te krijgen in welk mechanisme overheerst voor de groei van zilverdeeltjes op α -alumina, hebben we de zilverdeeltjes onderworpen aan verschillende hittebehandelingen. Een schematische weergave van de verschillende elementen die we onderzocht hebben is te zien in Figuur 5. De atmosfeer tijdens de hittebehandelingen was van groot belang (Figuur 5, links). Bij het verwarmen van de deeltjes tot 400 °C in waterstof (een reducerend gas) vond vrijwel geen deeltjesgroei plaats, maar in zuurstof (een oxiderend gas) wel. Onder oxiderende condities kunnen metaaloxideclusters worden gevormd, dus dit wijst op Ostwaldrijping.

Ook bleek de afstand tussen de zilverdeeltjes van grote invloed te zijn (Figuur 5, midden). Hoe dichter de deeltjes op elkaar waren geplaatst, hoe meer deeltjesgroei plaatsvond. Dit kan bij zowel bij diffusie en samensmelting als bij Ostwaldrijping een rol spelen, omdat bij beide verplaatsingen plaatsvinden (van of tussen de zilverdeeltjes), maar de afstand tussen de deeltjes heeft meestal een grotere invloed bij diffusie en samensmelting. Daarom hebben we nog beter gekeken naar de verplaatsingen van de gehele deeltjes (Figuur 5, rechts). Hiervoor hebben we gekeken naar het verschil in deeltjesgroei tussen zilverdeeltjes die wel of niet “opgesloten” waren in de poriën van het geordende macroporeuze α -alumina uit Hoofdstuk 2. Omdat het wel of niet limiteren van verplaatsingen van gehele zilverdeeltjes geen verschil gaf in de groei van de deeltjes, denken we dat de groei van zilverdeeltjes voornamelijk via Ostwaldrijping verloopt, waarbij vooral de verplaatsing van zilveroxideclusters een belangrijke rol speelt. Hierdoor weten we dat door de verschillen tussen de grootte van de zilverdeeltjes te verkleinen, en de afstand tussen de deeltjes te vergroten, we meer stabiele katalysatoren krijgen.

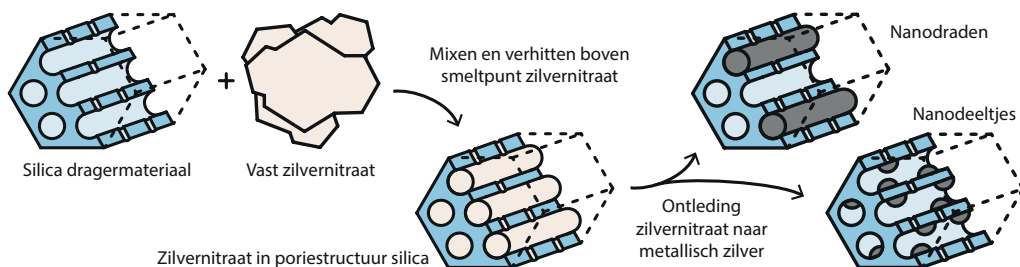


Figuur 5 Schematische weergave van de onderzochte elementen voor de stabiliteit van zilverdeeltjes.

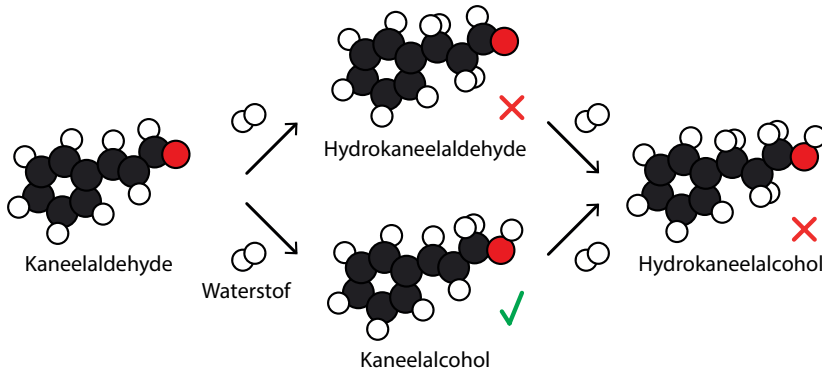
In **Hoofdstuk 4** bespreken we een alternatieve bereidingswijze voor zilverkatalysatoren. De meeste katalysatoren worden bereid door een metaalzout zo gelijk mogelijk over een dragermateriaal te verspreiden, waarna het metaalzout wordt ontleed door een hittebehandeling. Voor de verspreiding van het metaalzout zijn veel verschillende technieken. Vaak wordt het metaalzout opgelost in een vloeistof, meestal water, waarna de poriën van het dragermateriaal worden gevuld met deze oplossing. Hierna wordt het materiaal gedroogd, waarbij het metaalzout achterblijft in de poriën. Wij hebben een andere manier onderzocht om het metaalzout over het dragermateriaal te verspreiden, namelijk door middel van smeltinfiltratie. Bij deze methode verwarmen we een fysisch mengsel van poreus dragermateriaal met een metaalzout, in dit geval zilvernitraat, waardoor het zilvernitraat vloeibaar wordt, en het vanzelf de poriën van het dragermateriaal binnendringt. Dit komt door de capillaire krachten van de poriestructuur, vergelijkbaar met water in een spons, of geurvloeistof bij geurstokjes. Het voordeel van smeltinfiltratie is dat we op deze manier een grote hoeveelheid zilver kunnen afzetten. Daarnaast gebruiken we geen oplosmiddel, waardoor we minder afval produceren dat moet worden schoongemaakt. Het nadeel van deze methode is dat het moeilijk is om het metaalzout gelijkmatig over het dragermateriaal te verspreiden als je niet alle poriën vult, omdat het als vloeistof bij elkaar blijft.

Ook voor dit onderzoek hebben we een dragermateriaal gebruikt met een geordende poriestructuur, zodat we de verkregen materialen beter konden bestuderen. In dit geval gebruikten we een mesoporeus silica, met cilindrische poriën van 7 nm in diameter die van de ene kant van het deeltje naar de andere kant lopen. In Figuur 6 is de bereiding van de materialen via smelt infiltratie uitgebeeld. Het insmelten van het zilvernitraat ging heel gemakkelijk. Na het verwarmen van het mengsel van zilvernitraat en silica tot 250 °C (het smeltpunt van zilvernitraat is 212 °C) zat vrijwel al het metaalzout in de poriën van het silicamateriaal. Daarna hebben we het zilvernitraat ontleed door het mengsel te verwarmen in waterstof. Tijdens deze ontleding vond er veel transport van het zilver plaats. Hierdoor was het relatief eenvoudig om zilverdraden te vormen die sommige poriën volledig vulden. Ook is het, met wat meer moeite, gelukt om zilverdeeltjes van ongeveer 2–3 nm te maken, maar hierbij bleef niet al het zilver in de poriestructuur achter.

Zowel de katalysatoren met de nanodraden als de nanodeeltjes hebben we gebruikt voor de selectieve hydrogenatie van kaneelaldehyde naar kaneelalcohol, een reactie die (je kan



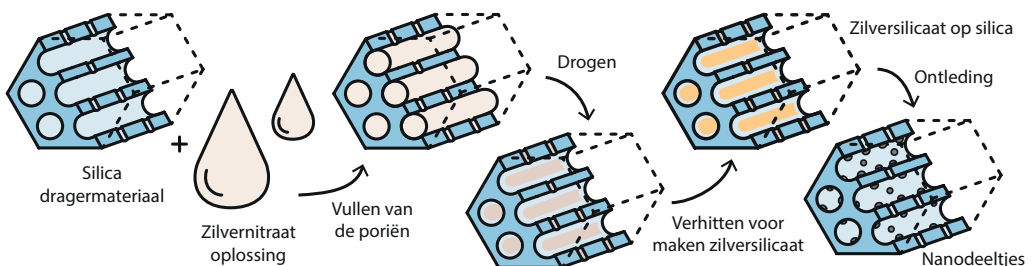
Figuur 6 Schematische weergave van bereiding van zilver nanodraden en nanodeeltjes via smelt infiltratie.



Figuur 7 Schematische weergave van de verschillende reactiepaden voor de hydrogenatie van kaneelaldehyde. Het groene vinkje markeert het gewenste product, de rode kruisjes markeren de ongewenste producten.

het al een beetje uit de naam opmaken) belangrijk is voor de farmaceutische, smaak- en parfumindustrie. Daarnaast is dit een modelreactie voor selectieve hydrogenatiereacties. De verschillende reactiepaden zijn te zien in Figuur 7. Als de waterstofatomen op de juiste plek worden ingevoegd, ontstaat kaneelalcohol. Maar als de hydrogenatie op een andere plek plaatsvindt, ontstaat hydrokaneelaldehyde. Ook kan de hydrogenatie twee keer plaatsvinden, waarbij hydrokaneelalcohol gevormd wordt. De activiteit van beide katalysatoren was niet heel hoog vergeleken met de beschreven activiteit van andere metalen uit de literatuur, maar goed voor wat je van zilverkatalysatoren kunt verwachten. Daarnaast was de selectiviteit, vooral van de zilvernanostraden, wel hoog. De zilverdraden hadden een hogere activiteit per oppervlakte zilver, dan de zilverdeeltjes. Dit laat zien dat smeltinfiltratie een interessante bereidingswijze is voor zilverkatalysatoren, en dat voor bepaalde hydrogenatiereacties de zilverdeeltjes niet te klein moeten zijn.

In **Hoofdstuk 5** zijn we nog beter gaan kijken naar de ontleding van het metaalzout tijdens de bereiding van de zilverkatalysatoren. Zoals hiervoor beschreven, kan het zilver verplaatsen tijdens de ontleding van het zilvernitraat in waterstof. Om dit tegen te gaan hebben we in dit hoofdstuk gebruik gemaakt van een tussenstructuur, zilversilicaat. In Figuur 8 staat uitgebeeld hoe we het zilversilicaat hebben gemaakt. Eerst hebben we zilvernitraat over het silica verdeeld door de poriën te vullen met een oplossing van zilvernitraat, en dit vervolgens te drogen. Omdat we hier met een lagere zilverlading werkten ten opzichte van Hoofdstuk 4,



Figuur 8 Schematische weergave van bereiding zilverkatalysatoren door gebruik te maken van zilversilicaat.

is nu slechts het oppervlak van het silica bedekt met zilvernitraat, en zijn de poriën niet volledig gevuld. Het zilversilicaat werd gevormd na reactie van gesmolten zilvernitraat met silica in zuurstof op hogere temperatuur (400 °C), waardoor de zilveratomen aan het dragermateriaal vastgehecht werden. In een volgende stap werd het zilversilicaat ontleed door het materiaal te verwarmen tot 150 °C in waterstof of koolmonoxide, waarbij zeer kleine zilverdeeltjes van ongeveer 1–2 nm werden gevormd. In tegenstelling tot de verkregen materialen uit Hoofdstuk 4, bleef al het zilver nu in de poriestructuur zitten.

Deze katalysator werd getest voor de oxidatie van koolstofmonoxide (zie Figuur 1), waarbij de zilverdeeltjes een goede activiteit, en vooral ook een hele goede stabiliteit lieten zien. Het gebruik van zilversilicaat bleek daarom een aantrekkelijke methode voor de bereiding van heel kleine zilverdeeltjes op silicadragermaterialen, vooral bij hoge zilverbeladingen. Met deze hoge zilverbeladingen kan het verschil in activiteit tussen zilver en andere, vaak duurdere metalen gedeeltelijk worden opgevangen, waardoor zilverkatalysatoren, met hun hoge selectiviteit en stabiliteit, nog interessanter worden voor verschillende selectieve oxidatie- of hydrogenatiereacties.

Acknowledgements

In my introduction, I listed some subjects that are essential in the field of catalysis and the research described in this thesis. Here, I would like to list some people who were essential to me for the realization of this thesis.

Allereerst wil ik **Krijn de Jong** en **Petra de Jongh** bedanken voor jullie fijne begeleiding. Ik ben blij dat jullie mijn promotoren waren en ik heb ontzettend veel van jullie geleerd. Krijn, bedankt voor je vertrouwen en de vrijheid om zelf een richting te kiezen. Maar ook bedankt voor je betrokkenheid en beschikbaarheid om het vervolg te bespreken als ik hierover twijfelde, of als ik naar mijn idee vast zat. Na onze besprekingen zag ik de waarde van mijn behaalde resultaten positiever in en had ik weer goede ideeën over wat ik verder nog kon proberen. Petra, je kritische houding en oog voor detail, je enthousiasme bij positieve uitkomsten en de gezelligheid tijdens/na een overleg heb ik altijd zeer gewaardeerd. Je bent heel betrokken geweest bij mijn onderzoek, waardoor velen dan ook dachten dat niet Krijn, maar jij mijn eerste promotor was. Dankjewel voor deze betrokkenheid, ook op persoonlijk gebied.

Daarnaast hebben **Jeroen van den Reijen** en **Claudia Keijzer** beide een grote bijdrage geleverd aan de inhoud van dit proefschrift, en ik ben blij dat jullie mijn paranimfen willen zijn. Jeroen, tijdens mijn masterproject kwam ik onder jouw begeleiding voor het eerst in aanraking met de bereiding van zilverkatalysatoren, en voor mijn eigen promotieonderzoek heb ik het werk op gebied van zilver van je overgenomen. Bedankt dat je mij op een prettige manier alle fijne kneepjes van het vak hebt geleerd en bedankt voor de mooie samenwerkingen die we hebben gehad. Claudia, bedankt dat je jouw masterproject onder mijn begeleiding wilde doen, waarbij je dankzij jouw goede en harde werk hele mooie resultaten hebt behaald. Ik ben ontzettend blij dat ik het stokje aan jou heb kunnen overdragen en dat het werk op gebied van zilver nu door jou wordt voortgezet met jouw eigen promotieonderzoek.

Ook heb ik met veel plezier de bachelorprojecten van **Phoebe van Ameyden**, **Sofie Ferwerda** en **Mike van de Poll**, mogen begeleiden, bedankt voor jullie inzet en enthousiasme. Naast dat ik jullie hopelijk het een en ander heb kunnen leren, heb ik ook heel veel geleerd van jullie, en van de door jullie behaalde resultaten.

I would also like to thank **Jovana Zečević** and **Baira Donoeva** for their contributions to my work. Jovana, even though my project and your career took other paths, I want to thank you for your support during your time spent as my co-promotor. Baira, your knowledge of selective hydrogenation catalysis contributed largely to the success of my paper about melt infiltration, thank you for your help on this subject. **Peter Ngene**, thank you for the many pleasant conversations that we had and for the useful discussions during team meetings.

Daarnaast ben ik de secretariële en technische staf van MCC en ICC erg dankbaar voor de vele ondersteuning rondom de organisatie van de groep en het onderhouden van alle apparatuur en opstellingen in het laboratorium. Bedankt **Dymph Serrée**, **Ilonka Buhrs** en **Sylvia Visser**

Acknowledgments

dat er altijd wel iemand klaarstond om te helpen bij administratieve zaken. **Hans Meeldijk**, bedankt dat ik altijd op jouw hulp kon rekenen als ik weer eens iets verkeerd had gedaan rond een elektronenmicroscop (zelfs op je vrije avond/dag) en voor je gezelligheid tijdens het tijdens het afhandelen van de problemen. **Ad van der Eerden**, bedankt voor je harde werk om de veiligheid op het lab te blijven verbeteren en specifiek voor je aandacht rondom het verbeteren van de veiligheid van de epoxidatie opstelling. **Dennie Wezendonk**, bedankt voor al je inspanningen rondom het verzorgen van de vele verschillende karakterisaties op mijn materialen. **Jan Willem de Rijk**, bedankt voor je inzet, met name bij de opstellingen voor ethyleen epoxidatie en koolstofmonoxide oxidatie. **Pascal Wijten**, bedankt voor je hulp met de multi-autoclaaf opstelling en met de verschillende GC's. Verder wil ik **Oscar Kerkenaar**, **Ramon Oord**, **Chris Schneijdenberg**, **Jochem Wijten**, **Fouad Soulimani**, **Joris Janssens**, **Marjan Versluijs-Helder**, **Herrick Schaink**, **Ad Mens**, **Mies van Steenbergen** (UIPS) en **Eric Hellebrand** (Geolab) bedanken voor de hulp bij verschillende opstellingen/technieken en bij het oplossen van allerlei kleine en toch iets minder kleine problemen op het lab.

Naast de directe samenwerkingen heb ik veel gehad aan de (wetenschappelijke) discussies met de vele collega's van MCC en ICC, onder andere bij werkbesprekingen en in het lab, maar ook tijdens pauzes of bij een van de vele sociale activiteiten. **Johan de Boed**, we hebben samen heel wat uren doorgebracht rondom, of denkend over, de epoxidatie opstelling. Uiteindelijk hebben we er beide hele mooie en goede resultaten mee behaald. Dankjewel voor je onuitputbare energie om toch nog maar nog een extra keer iets anders te proberen, opnieuw een kalibratie uit te voeren of nieuwe dingen uit te zoeken. **Nynke Krans**, bedankt voor de gezellige tijd, met onze conferentie in Thailand toch wel als hoogtepunt, en de fijne gesprekken met adviezen die we konden uitwisselen, binnen en buiten het David de Wied. **Lars van der Wal**, we begonnen op dezelfde dag en hebben ons werk ook ongeveer gelijktijdig afgerond. Het was fijn dat we samen de PhD wereld konden verkennen, en af en toe even lekker tegen elkaar konden klagen over de frustraties die we beiden tegenkwamen. **Stijn Hinterding**, ook al zat je vrijwel altijd in een ander gebouw, dankjewel voor de leuke tijden wanneer we elkaar wel tegenkwamen. Een van jouw kwaliteiten is om stress bij anderen weg te halen en zaken te relativieren, waar ik regelmatig dankbaar gebruik van heb gemaakt. **Anne-Eva Nieuwelink**, bedankt voor de fijne theepauzes als ik daar echt even aan toe was en het altijd kunnen geven van andere invalshoeken. Dankjewel **Laura de Kort** en **Nienke Visser** voor de gezelligheid bij de keren dat meer zin had in (lekkere) koffie en een korte wandeling. **Jessi van der Hoeven**, **Rolf Beerthuis** and **Nazila Masoud**, you were great neighbors in the office and thank you for the many insightful and lovely discussions and chats. **Erik Maris**, bedankt voor de vele leuke wandelingen tijdens het thuiswerken van de laatste jaren. **Lisette Pompe**, je bereidwilligheid om iedereen te willen helpen waardeerde ik niet alleen tijdens onze PhD tijd, maar ook nu opnieuw als jouw collega bij het RIVM.

Furthermore, I would also like to thank **Carolien Vis**, **Christa van Oversteeg**, **Francesco Mattarozzi**, **Giorgio Totarella**, **Jelle Boereboom**, **Jochem Wijten**, **Jogchum Oenema**, **Jongkook Hwang**, **JX**, **Katarína Stančíaková**, **Kristiaan Helfferich**, **Laura Barberis**, **Lee Durndell**, **Lennart Weber**, **Luc Smulders**, **Maaïke van Ittersum**, **Marisol Tapia Rosales**, **Marjolein Velthoen**, **Mark Meijerink**, **Matt Peerlings**, **Nikos Nikolopoulos**, **Oscar Brandt Corstius**,

Peter Bramwell, Ramon Oord, Remco Dalebout, Robert Geitner, Sander Lambregts, Savannah Turner, Silvia Zanoni, Suzan Schoemaker, Suzanne Verkleij, Xinwei Ye, and all other colleagues from MCC and ICC for all the fun times.

Ook heb ik altijd op de steun van mijn lieve vrienden kunnen rekenen. Daarnaast hielpen de vele borrels, verjaardagen, spelletjesmiddagen, etentjes, escape rooms, weekendjes weg, bierfestivals, vakanties en alle andere leuke dingen met onder andere **Team Oei**, het **27ste**, de **ZBF groep** en verschillende **D&D groepen** mij eraan te herinneren dat er ook nog andere dingen waren in het leven naast mijn proefschrift. **Gerda Kamsma**, ik ben nog steeds ontzettend dankbaar voor onze vriendschap die begonnen is op de eerste dag dat we aan de opleiding scheikunde begonnen. Dankjewel voor alle fijne en gezellige momenten die we samen op de universiteit, maar vooral ook daarbuiten hebben meegemaakt. **Juliette Poulisse**, we hebben laatst onze 12.5 jaar vriendschap kunnen vieren en ondanks dat je waarschijnlijk weinig van de inhoud van dit boekje snapt, kon ik toch altijd mijn frustraties bij je uiten en mijn successen met je vieren. **Fleur de Vries**, onze vriendschap gaat nog langer terug. Al op de middelbare school leerde je mij te zijn wie ik ben, door zelf te zijn wie jij bent en te laten zien dat daar helemaal niets mis mee is. Ik ben blij dat we elkaar nog steeds niet uit het oog verloren zijn. **Merel van de Plassche**, onze vriendschap is (vrij) letterlijk uitgegroeid tot familie, en ik ben dankbaar dat onze vriendschap alleen maar sterker is geworden sinds ik je broer heb leren kennen. Dankjewel dat je altijd voor mij klaarstaat.

Kees en **Agnes**, lieve pap en mam, dankjewel voor alles wat jullie mij gegeven hebben. Voor jullie onvoorwaardelijke steun en jullie inspanningen om steeds toch te proberen (een beetje) te begrijpen waar ik nou mee bezig was. En voor de nuchtere blik, eigenwijsheid (of koppigheid) en doorzettingsvermogen die ik van jullie mee heb mogen krijgen. **Karin, Linda**, en **Marijn**, bedankt voor de fantastische vakanties samen waarbij ik er echt even uit kon. Karin, bedankt voor je rol als grote zus waarbij je er altijd voor mij bent, ook wanneer dit voor jou minder voordelig is (zoals het parkeren van jouw auto bij mij thuis, zodat ik er tenminste makkelijk gebruik van kan maken nu je hem niet bij jouw eigen voordeur kwijt kan). Linda, bedankt voor je nieuwsgierigheid naar mijn onderzoek en je inspanningen om mijn problemen goed genoeg te proberen te begrijpen, zodat je hierover mee kon denken. Bedankt voor je creatieve en vindingrijke ideeën, die nog vaker dan verwacht ook hebben bijgedragen de oplossing. Marijn, ook jij bent steeds meer als zus gaan aanvoelen, dankjewel dat je deze rol steeds meer op je neemt en dat ik altijd bij je terecht kan. Lieve familie, bedankt voor jullie interesse in mijn onderzoek en voor jullie trots als ik weer een stapje verder kwam.

Karel, dankjewel voor je begrip als ik ervoor koos om te lang door te werken, ook als dit betekende dat ik daarna bij jou niet veel meer waard was. Dankjewel voor je steun en je energie om mij op te vrolijken als het tegen zat en voor je aanmoedigen om, voor ik verder ging, eerst even rust te pakken. Dankjewel voor je overtuiging dat ik echt wel een manier zou vinden om toch mijn doelen te behalen, en dankjewel voor je blijheid als dit dan ook zo bleek te zijn. Ik hou van je, tweeeindigduizend veel.

List of publications and presentations

Publications

- P.H. Keijzer & J.E. van den Reijen, P.E. de Jongh, 'Pore structure stabilization during the preparation of single phase ordered macroporous α -alumina', *Materialia*, **4**, 423–430, 2018 (Chapter 2)
- P.H. Keijzer & J.E. van den Reijen, C.J. Keijzer, K.P. de Jong, P.E. de Jongh, 'Influence of atmosphere, interparticle distance and support on the stability of silver on α -alumina for ethylene epoxidation', *Journal of Catalysis*, **405**, 534–544, 2022 (Chapter 3)
- P.H. Keijzer, B. Donoeva, K.P. de Jong, P.E. de Jongh, 'Supported silver catalysts prepared via melt infiltration: Synthesis, characterization and performance in selective hydrogenation', *Catalysis Today*, **375**, 393–400, 2021 (Chapter 4)
- P.H. Keijzer, P.E. de Jongh, K.P. de Jong, 'Utilization of silver silicate for the formation of highly dispersed silver on silica catalysts', *ChemCatChem*, accepted (Chapter 5)

Oral presentations

- 6th International School-Conference for Young Scientists “Catalysis: from Science to Industry”, Tomsk, Russia, 2020, 'Ordered macroporous α -alumina as catalyst support for enhanced thermal stability of silver nanoparticles' (online conference)
- NWO CHAINS, Velthoven, Netherlands, 2019, 'Preparation of ordered macroporous α -alumina catalyst supports'
- European Materials Research Society (E-MRS) - Spring Meeting, Warsaw, Poland, 2019, 'Supported silver catalysts prepared via melt infiltration: Synthesis, characterization and catalytic performance'
- The 8th Asia-Pacific Congress on Catalysis, Bangkok, Thailand, 2019, 'Supported silver catalysts prepared via melt infiltration: Synthesis, characterization and catalytic performance'
- Netherlands' Catalysis and Chemistry Conference (N3C), Noordwijkerhout, Netherlands, 2019, 'Supported silver catalysts prepared via melt infiltration: Synthesis, characterization and catalytic performance'
- 4th International Conference on Advanced Complex Inorganic Nanomaterials (ACIN), Namur, Belgium, 2018, 'Synthesis of supported silver catalysts using melt infiltration'

List of publications and presentations

- *Canadian Symposium on Catalysis (CSC), Vancouver, Canada, 2020, 'Ordered macroporous α -alumina as catalyst support for enhanced silver nanoparticle stability' – oral accepted, conference canceled due to Covid-19*
- *Canadian Symposium on Catalysis (CSC), Vancouver, Canada, 2020, 'Supported silver catalysts prepared via melt infiltration: Synthesis, characterization and catalytic performance' – oral accepted, conference canceled due to Covid-19*
- *17th International Congress on Catalysis (ICC), San Diego, United States of America, 2020, 'Supported silver catalysts prepared via melt infiltration: Synthesis, characterization and catalytic performance' – oral accepted, conference canceled due to Covid-19*

Poster presentations

- Netherlands' Catalysis and Chemistry Conference (N3C), Noordwijkerhout, Netherlands, 2020, 'Ordered macroporous α -alumina as catalyst support for enhanced silver nanoparticle stability'
- 14th European Congress on Catalysis (Europacat), Aachen, Germany, 2019, 'Supported silver catalysts prepared via melt infiltration: Synthesis, characterization and catalytic performance' (Presented by Baira Donoeva)
- 26th North American Catalysis Society Meeting (NAM), Chicago, United States of America, 2019, 'Supported silver catalysts prepared via melt infiltration: Synthesis, characterization and catalytic performance' (Presented by Baira Donoeva)
- 3rd European Summer School on Catalyst Preparation: Fundamental Concepts and Industrial Requirements (CatPrep), Vogüé, France, 2019, 'Supported silver catalysts prepared via melt infiltration: Synthesis, characterization and catalytic performance'
- 4th International Conference on Advanced Complex Inorganic Nanomaterials (ACIN), Namur, Belgium, 2018, 'Pore structure stabilization during the preparation of ordered macroporous α -alumina'
- 12th International Symposium on the "Scientific Bases for the Preparation of Heterogeneous Catalysts" (PREPA12), Louvain-la-Neuve, Belgium, 2018, 'Fundamental study on the synthesis of supported silver catalysts using melt infiltration'
- Netherlands' Catalysis and Chemistry Conference (N3C), Noordwijkerhout, Netherlands, 2018, 'Fundamental study on the synthesis of supported silver catalysts using melt infiltration'
- NWO CHAINS, Velthoven, Netherlands, 2017, 'Fundamental study on the synthesis of supported silver catalysts using melt infiltration'

- EMAT Workshop on Transmission Electron Microscopy, Antwerp, Belgium, 2017, 'Fundamental study on the synthesis of supported silver catalysts using melt infiltration'
- Netherlands' Catalysis and Chemistry Conference (N3C), Noordwijkerhout, Netherlands, 2017, 'Ordered macroporous α -alumina as support material for the silver catalyzed epoxidation of ethylene'
- *17th International Congress on Catalysis (ICC), San Diego, United States of America, 2020, 'Ordered macroporous α -alumina as catalyst support for enhanced silver nanoparticle stability' – poster accepted, conference canceled due to Covid-19*

About the author

Petra Keijzer was born on February 20, 1992, in the Noordoostpolder (Flevoland, the Netherlands). After finishing pre-university education (VWO) at the Zuyderzee College in Emmeloord, she moved to Utrecht in 2010, where she studied chemistry at Utrecht University. During her bachelor study, Petra spent one year as full-time board member of the chemistry students' association 'U.S.S. Proton', where she focused on educational affairs within the chemistry department, and participated in several representation councils. After obtaining her BSc diploma in 2014, Petra continued her studies at Utrecht University by enrolling in the master program 'Nanomaterials: Chemistry and Physics'. She performed her master thesis research in the group 'Inorganic Chemistry and Catalysis', under the supervision of (now dr.) J.E. van den Reijen and prof. dr. P.E. de Jongh. During this research project, Petra designed a preparation route for macroporous α -alumina, which is the basis for the second chapter of this thesis. Afterward, she did an internship at the Johnson Matthey Technology Centre, in Sonning Common, United Kingdom, where she worked on alternative catalyst preparation methods in the automotive catalyst research group. After Petra obtained her MSc diploma in 2016, she started her PhD project under the supervision of prof. dr. ir. K.P. de Jong and prof. dr. P.E. de Jongh in the research group Inorganic Chemistry and Catalysis (now Materials Chemistry and Catalysis). The main results of this project are described in this thesis and have been published in peer-reviewed academic journals and presented at (inter)national conferences. Besides her scientific research, Petra taught various practical lab courses and theoretical tutorial classes to chemistry bachelor and master students, and supervised several research projects of BSc and MSc students. Per August 2021, Petra continued her career as a scientific researcher at the RIVM, the Dutch National Institute for Public Health and the Environment.



